

1-1-2010

# Mechanical Properties Of Butt Welded AZ31B Magnesium Alloys

MD. S.M. Chowdhury  
*Ryerson University*

Follow this and additional works at: <http://digitalcommons.ryerson.ca/dissertations>

 Part of the [Mechanical Engineering Commons](#)

---

## Recommended Citation

Chowdhury, MD. S.M., "Mechanical Properties Of Butt Welded AZ31B Magnesium Alloys" (2010). *Theses and dissertations*. Paper 1290.

This Thesis is brought to you for free and open access by Digital Commons @ Ryerson. It has been accepted for inclusion in Theses and dissertations by an authorized administrator of Digital Commons @ Ryerson. For more information, please contact [bcameron@ryerson.ca](mailto:bcameron@ryerson.ca).

# **MECHANICAL PROPERTIES OF BUTT WELDED AZ31B MAGNESIUM ALLOYS**

**By**

**MD. SAKI MURSALIN CHOWDHURY**

**Bachelor of Science in Mechanical Engineering**

**Bangladesh University of Engineering and Technology (BUET), 2006**

**A thesis presented to Ryerson University**

**in partial fulfillment of the requirements for the degree of**

**Master of Applied Science in the program of Mechanical Engineering**

**Toronto, Ontario, Canada, 2010**

**© Md. Saki Mursalin Chowdhury 2010**

## **AUTHOR'S DECLARATION**

I hereby declare that I am the sole author of this thesis.

I authorize Ryerson University to lend this thesis to other institution or other individuals for the purpose of scholarly research.

Md. Saki Mursalin Chowdhury: \_\_\_\_\_

I further authorize Ryerson University to reproduce this thesis by photocopying or by other means, in total or in part, at the request of other institutions or individuals for the purpose of scholarly research.

Md. Saki Mursalin Chowdhury: \_\_\_\_\_



# **MECHANICAL PROPERTIES OF BUTT WELDED AZ31B MAGNESIUM ALLOYS**

Md. Saki Mursalin Chowdhury

MASc., Mechanical Engineering

Ryerson University, Toronto, 2010

## **ABSTRACT**

Mechanical properties of friction stir welded (FSWed), double sided arc welded (DSAWed), fiber laser welded (FLWed) and diode laser welded (DLWed) on AZ31B Mg alloy were studied. After welding, grains at the centre became recrystallized. Brittle phase  $\beta$ -Mg<sub>17</sub>Al<sub>12</sub> particles observed at the centre of the joint during fusion welding process. The yield strength (YS), ultimate tensile strength (UTS) and fatigue strength were lower in the FSWed samples than in the DSAWed samples. Welding defect at the bottom of the FSWed joint was observed when right hand thread (RHT) weld tool was considered. In FLWed joint, YS, UTS and fatigue strength, with a joint efficiency of ~91%, was achieved while the YS, UTS and fatigue strength of the DLWed joints were notably lower. The DSAWed joints and DLWed joints exhibited a higher strain hardening capacity in comparison with the FSWed joints and FLWed joints, respectively.

## **ACKNOWLEDGEMENTS**

I would like to thank my supervisors Dr. Daolun Chen and Dr. S. D. Bhole for their guidance, support and encouragement during my studies at Ryerson University. I would also like to thank Dr. X. Cao, Aerospace Manufacturing Technology Centre, Institute for Aerospace Research, National Research Council Canada, Montreal, Dr. Y. Zhou and Dr. D. Weckman, University of Waterloo, Waterloo, Ontario, Canada for their helpful discussions.

I would also like to thank the Natural Sciences and Engineering Research Council of Canada (NSERC) and AUTO21 for providing financial support. This investigation involves part of the Canada-China-USA Collaborative Research Project on the Magnesium Front End Research and Development (MFERD), and material supports from National Research Council Canada and University of Waterloo are also acknowledged.

I would like to extend my thanks to all my friends and colleagues at Ryerson University for helping me and keeping my spirits up. Special thanks to A. Machin, J. Amankrah, Q. Li and R. Churaman for their strong support in providing easy access to the facilities.

Words cannot express my deepest gratitude towards my parents.

**To**

**My Parents**

**Mrs. Rowshan Ara Begum, Md. Nurul Amin Chowdhury**

# TABLE OF CONTENTS

AUTHOR’S DECLARATION.....	ii
BORROWER’S PAGE.....	iii
ABSTRACT.....	iv
ACKNOWLEDGEMENTS.....	v
TABLE OF CONTENTS.....	vii
LIST OF TABLES.....	x
LIST OF FIGURES.....	xii
NOMENCLATURE.....	xx
<b>CHAPTER 1: INTRODUCTION .....</b>	<b>1</b>
<b>CHAPTER 2: LITERATURE REVIEW .....</b>	<b>3</b>
2.1    Magnesium and Its Alloys.....	3
2.2    Physical Metallurgy and Properties.....	3
2.3    Types of Magnesium Alloys.....	6
2.4    Double Sided Arc Welding.....	7
2.5    Friction Stir Welding.....	10
2.6    Fiber Laser Welding.....	12
2.7    Diode Laser Welding.....	13
2.8    Previous Studies.....	14
2.9    Research Objective.....	18
<b>CHAPTER 3: EXPERIMENTAL PROCEDURE.....</b>	<b>20</b>

3.1	Materials and Composition.....	20
3.2	Sample preparation and testing.....	21
3.2.1	Metallography.....	22
3.2.2	Quantitative Image Analysis.....	22
3.2.3	Micro-hardness Tests.....	23
3.2.4	Tensile Tests.....	23
3.2.5	Fatigue Tests.....	24

## **CHAPTER 4: MECHANICAL PROPERTIES OF FRICTION STIR AND**

	<b>DOUBLE SIDED ARC WELDED AZ31B Mg JOINTS .....</b>	<b>25</b>
4.1	Microstructurel of the Base Metal.....	25
4.2	Microstructure of the Friction Stir Welded Joint.....	25
4.2.1	Effect of Welding Parameters.....	27
4.2.2	Effect of Threads on Material Flow.....	29
4.3	Microstructure of The Double Sided Arc Welded Joint.....	32
4.4	EDS Analysis.....	34
4.5	Micro-hardness.....	39
4.6	Tensile Strength and Ductility.....	40
4.6.1	Effect of Weld Parameter.....	42
4.6.2	Effect of Thread.....	50
4.6.3	Change of Failure Location of the FSWed Joint.....	51
4.7	Strain Hardening Behavior.....	52
4.7.1	Effect of Welding Parameter and Thread.....	61
4.7.2	Strain Rate Sensitivity.....	63

4.8	Tensile Fractography.....	64
4.9	Fatigue Properties.....	66
4.9.1	Effect of Welding Paramter.....	68
4.9.2	Effect of Thread.....	71
4.10	Fatigue Fractography.....	73
<b>CHAPTER 5: MECHANICAL PROPERTIES OF LASER WELDED AZ31B</b>		
<b>Mg JOINTS.....</b>		
5.1	Microstructurel of the Fiber and Diode Laser Welded Joints.....	76
5.2	Microhardness.....	85
5.3	Tensile Strength and Ductility.....	86
5.4	Strain Hardening Behavior.....	88
5.5	Tensile Fractography.....	92
5.6	Fatigue Properties.....	93
5.7	Fatigue Fractography.....	96
<b>CHAPTER 6: CONCLUSIONS AND FUTURE WORK.....</b>		
6.1	Summary and Conclusions.....	99
6.2	Scope of Future Work.....	102
<b>REFERENCES.....</b>		
		104

## LIST OF TABLES

Table 2-1	Physical properties of metals [12].....	4
Table 3-1	Chemical composition of AZ31 Mg alloy.....	20
Table 3-2	Welding parameter of all welded joints.....	21
Table 4-1	Failure locations of the FSWed specimens during tensile testing.....	52
Table 4-2	Hardening capacity of the base alloy, FSWed and DSAWed samples tested at different strain rates.....	53
Table 4-3	Ultimate tensile strength, fatigue limit and fatigue ratio of the BM, DSAWed and FSWed joints.....	67
Table 4-4	Fatigue strength coefficient $\sigma_f'$ and fatigue strength exponent $b$ of the base metal, DSAWed and FSWed joints.....	68
Table 4-5	Ultimate tensile strength, fatigue limit and fatigue ratio of the BM and FSWed joints at different welding speeds and rotational rates.....	70
Table 4-6	Ultimate tensile strength, fatigue limit and fatigue ratio of the BM and FSWed joints by using different threads of weld tool at different welding speeds and rotational rates.....	72
Table 5-1	Hardening capacity of the base alloy, FLWed and DLWed samples tested at different strain rates.....	89

Table 5-2 Ultimate tensile strength, fatigue limit and fatigue ratio of the BM,  
FLWed and DLWed joints .....94

Table 5-3 Fatigue strength coefficient  $\sigma_f'$  and fatigue strength exponent  $b$  of the  
base metal, FLWed and DLWed joints.....95

## LIST OF FIGURES

Figure 2.1	Basal, Prismatic and Pyramidal slip systems in pure magnesium [13].....	5
Figure 2.2	Schematic diagrams of welding systems. (a) Regular welding system and (b) double sided arc welding system [16].....	8
Figure 2.3	A schematic of friction-stir welding process [18] .....	10
Figure 3.1	Geometry and dimensions of the sub-sized tensile/fatigue test specimen according to ASTM E8M [64].....	24
Figure 4.1	Typical microstructures of the base metal (BM) of the AZ31 Mg alloy.....	25
Figure 4.2	Typical macroscopic and microscopic structures of a friction stir welded AZ31 alloy. (a) Top weld bead surface, (b) cross-section of the welded joint, (c) heat affected zone(HAZ), (d) thermomechanically-affected zone (TMAZ), and (e) stir zone (SZ).....	26
Figure 4.3	Effect of welding speed and rotational rate on the grain structure in the stirred zone at (a) 5 mm/s-1000 rpm, (b) 10 mm/s-1000 rpm, (c) 20 mm/s-1000 rpm, (d) 10 mm/s-2000 rpm, (e) 20 mm/s-2000 rpm, and (f) 30 mm/s-2000 rpm.....	28
Figure 4.4	(a) Optical microscopic image and (b) SEM image of fracture surface of a FSWed joint made with a right hand thread (RHT) pin	

	tool in the clockwise rotation at a welding speed of 10 mm/s and 2000 rpm.....	29
Figure 4.5	Schematic illustration of the plasticized material flow during FSW using (a) right hand thread (RHT) and (b) left hand thread (LHT) pin tools in the clockwise rotation.....	30
Figure 4.6	Typical macroscopic and microscopic structures of a double sided arc welded AZ31 alloy. (a) Top weld bead surface, (b) cross- section of the welded joint, (c) heat-affected zone (HAZ), and (d) fusion zone (FZ) .....	33
Figure 4.7	EDS line scan showing the compositional variation across the particles in base metal (BM) .....	35
Figure 4.8	EDS line scan showing the compositional variation across the particles in heat-affected zone (HAZ) .....	36
Figure 4.9(a)	EDS line scan showing the compositional variation across the particles in the fusion zone (FZ) of DSAWed joint .....	37
Figure 4.9(b)	EDS line scan showing the compositional variation across the particles in fusion zone (FZ) of DSAWed joint at higher magnification.....	38
Figure 4.10	Microhardness profile across a) DSAWed sample, and b) FSWed sample.....	39

Figure 4.11	Typical engineering stress versus engineering strain curves of the AZ31B base alloy, FSWed and DSAWed samples tested at a strain rate of $1 \times 10^{-5} \text{ s}^{-1}$ .....	40
Figure 4.12	Effect of strain rate on (a) yield strength (YS), (b) ultimate tensile strength (UTS), and (c) ductility of the base metal, FSWed and DSAWed samples .....	41
Figure 4.13	(a) Typical engineering stress-strain curves of the AZ31B base alloy and FSWed samples tested at a strain rate of $1 \times 10^{-4} \text{ s}^{-1}$ , (b) a magnified view of the region boxed in (a) .....	43
Figure 4.14	Effect of strain rate on (a) yield strength (YS), (b) ultimate tensile strength (UTS), and (c) ductility of the AZ31B FSWed samples at different welding speeds and rotational rates .....	44
Figure 4.15	Yield strength versus grain size in the AZ31B alloy after FSW at different welding speeds and rotational rates .....	47
Figure 4.16	A comparison of the YS and UTS of the AZ31B FSWed joints, as a function of the weld pitch [the ratio of welding speed ( $v$ ) to rotational rate ( $\omega$ )], with those reported in the literature.....	48
Figure 4.17	Effect of pin tool thread orientation on (a) YS and UTS, and (b) ductility of the AZ31B-H24 FSWed joints at a welding speed of 10 mm/s and rotational rate of 2000 rpm.....	50

Figure 4.18	Schematic illustration of a true stress versus true strain curve.....	55
Figure 4.19	Effect of strain rate in the base metal, FSWed and DSAWed samples on (a) $n$ -value, (b) $n_1$ -value and (c) $n^*$ -value.....	56
Figure 4.20	Strain hardening rate ( $\theta$ ) versus net flow stress ( $\sigma - \sigma_y$ ) of the base metal tested at different strain rates.....	57
Figure 4.21	Strain hardening rate ( $\theta$ ) versus net flow stress ( $\sigma - \sigma_y$ ) of the base metal, FSWed and DSAWed samples tested at a strain rate of $1 \times 10^{-2} \text{ s}^{-1}$ .....	59
Figure 4.22	Effect of weld parameter on (a) $n$ -value and (b) $n^*$ -value in the AZ31B FSWed samples at different welding speeds and rotational rates.....	61
Figure 4.23	Effect of pin tool thread orientation on (a) $n$ -value and (b) $n^*$ -value in the AZ31B FSWed samples at a welding speed of 10 mm/s and rotational rate of 2000 rpm.....	62
Figure 4.24	A typical plot used to evaluate the strain-rate sensitivity, $m_L$ , at a true strain value of 2.5% via the Lindholm's approach for the base metal, DSAWed and FSWed samples.....	63
Figure 4.25	Typical SEM images showing the fracture surfaces of samples tested at a strain rate $1 \times 10^{-3} \text{ s}^{-1}$ . (a) base metal, (b) FSWed sample, and (c) DSAWed sample.....	65

Figure 4.26	S-N curves of the AZ31B base metal, DSAWed and FSWed joints tested at R=0.1, 50 Hz and room temperature.....	66
Figure 4.27	S-N curves of the AZ31B base metal and FSWed joints at different welding speeds and rotational rates tested at R=0.1, 50 Hz and room temperature.....	69
Figure 4.28	S-N curves of the AZ31B base metal and FSWed joints at 10 mm/s welding speed and 2000 rpm rotational rate using LHT and RHT weld tool tested at R=0.1, 50 Hz and room temperature.....	71
Figure 4.29	SEM images showing the fracture surfaces of the FSWed samples, after fatigue testing at a stress amplitude of 60 MPa, made with (a) RHT pin tool; (b) LHT pin tool in the clockwise rotation.....	73
Figure 4.30	Typical SEM images of the fatigue fracture surface of a FSWed sample made with the LHT pin tested at a stress amplitude of 60 MPa. (a) fatigue crack initiation area at a low magnification; (b) fatigue crack initiation area at an intermediate magnification; (c) backscattered electron image of (b); (d) fatigue crack propagation area at a high magnification; (e) EDS spectrum of the particle near the surface on the image (c) indicated by an arrow.....	74
Figure 5.1	Schematic illustration of (a) keyhole and (b) conduction modes during laser welding.....	77
Figure 5.2	Weld bead of (a) fiber laser and (b) diode laser welded joints.....	77

Figure 5.3	Typical macroscopic and microscopic structures of a fiber laser welded (FLWed) joint at a welding speed of 100 mm/s. (a) cross section of the welded joint, (b) base metal (BM) (etchant 1), (c) heat-affected zone (HAZ) at 400X (etchant 1), (d) columnar dendrites in the boundary of fusion zone (FZ) at 1000X (etchant 1), (e) columnar dendrites at 400X (etchant 2), (f) FZ at 400X (etchant 1) and (g) FZ at 200X (etchant 2) and (h) schematic diagrams of the bubble formation in the FZ.....	79
Figure 5.4	Typical macroscopic and microscopic structures of a diode laser welded (DLWed) joint at a welding speed of 8.33 mm/s. (a) cross section of the welded joint, (b) heat-affected zone (HAZ) at 400X (etchant 1), (c) columnar dendrites at 200X (etchant 1), (d) columnar dendrites at 400X (etchant 2), (e) fusion zone (FZ) at 200X (etchant 1), (f) FZ at the same magnification (etchant 2) and (g) heterogeneous nuclei in the FZ (etchant 2).....	80
Figure 5.5	Effect of temperature gradient $G$ and growth rate $R$ on the formation of various solidification microstructures [116].....	81
Figure 5.6	EDS line scan showing the typical compositional variation across a particle in the FZ of FLWed joint.....	83
Figure 5.7	EDS line scan showing the typical compositional variation across two particles in the FZ of DLWed joint .....	84

Figure 5.8	Typical microhardness profile of (a) fiber laser welded joint at a welding speed of 100 mm/s and (b) diode laser welded joint at a welding speed of 8.33 mm/s.....	85
Figure 5.9	Typical engineering stress-strain curves of the AZ31B Mg alloy, fiber laser and diode laser welded samples tested at a strain rate of $1 \times 10^{-4} \text{ s}^{-1}$ .....	86
Figure 5.10	Effect of strain rate on (a) yield strength (YS) (b) ultimate tensile strength (UTS) and (c) ductility of the FLWed and DLWed samples.....	88
Figure 5.11	Effect of strain rate on (a) n-value, and (b) n*-value of the FLWed and DLWed samples.....	90
Figure 5.12	Strain hardening rate ( $\theta$ ) versus net flow stress ( $\sigma - \sigma_y$ ) of the FLWed and DLWed samples tested a strain rate of $1 \times 10^{-3} \text{ s}^{-1}$ .....	91
Figure 5.13	Typical SEM images showing the fracture surfaces after tensile testing at a strain rate of $1 \times 10^{-5} \text{ s}^{-1}$ , (a) overall view of the entire fracture surface and (b) and (c) magnified view at higher magnifications of a FLWed sample, (d) overall view of the entire fracture surface, and (e) magnified view at a higher magnification of a DLWed sample.....	92
Figure 5.14	S-N curves of the AZ31B base metal, FLWed and DLWed joints tested at R=0.1, 50 Hz and room temperature.....	94

Figure 5.15 Typical SEM images of fatigue fracture surface of FLWed joints.  
(a) overall view of the entire fracture surface at a lower stress amplitude of 40 MPa, (b) multiple crack initiation at a higher stress amplitude of 80 MPa, (c) crack initiation from a welding defect, and (d) crack propagation zone.....96

Figure 5.16 Typical SEM images of fatigue fracture surface of a DLWed joint tested at a stress amplitude of 40 MPa. (a) overall view of the entire fracture surface at a low magnification (b) welding defect at a higher magnification, (c) crack initiation site at a higher magnification, and (e) crack propagation zone at a higher magnification.....97

# NOMENCLATURE

<u>Acronym</u>	<u>Definition</u>
Al	Aluminum
<i>ASTM</i>	American society for testing and materials
C	Carbon
CNC	Computer numerical control
BM	Base metal
EDS	Energy dispersive X-ray spectrometry
FSW	Friction stir welding
FSWed	Friction stir welded
DSAW	Double sided arc welding
DSAWed	Double sided arc welded
FLW	Fiber laser welding
FLWed	Fiber laser welded
DLW	Diode laser Welding
DLWed	Diode laser welded

FZ	Fusion zone
SZ	Stir zone
GHG	Green house gas
GTAW	Gas tungsten arc welding
PAW	Plasma arc welding
HAZ	Heat affected zone
TMAZ	Thermo-mechanically affected zone
HCP	Hexagonal close pack
FCC	Face centered cubic
BCC	Body centered cubic
ISO	International standards organization
LASER	Light amplification by stimulated emission of radiation
Mg	Magnesium
Zn	Zinc
Mn	Manganese
Zr	Zirconium
Si	Silicon

Th	Thorium
Nd	Neodymium
YAG	Yttrium-Aluminum-Garnet
RPM	Revolution per minute
S-N	Stress vs. Number of cycle to failure
SEM	Scanning electron microscopy
UTS	Ultimate tensile strength
YS	Yield strength
XRD	X-ray diffraction analysis
TTT	Through the thickness

**Symbol**

**Definition**

$K$	Strength coefficient according to Hollomon equation
$K_l$	Strength coefficient according to Ludwik equation
$K^*$	Strength coefficient according to modified equation
$n$	Strain hardening exponent according to Hollomon equation
$n_l$	Strain hardening exponent as per Ludwik equation
$n^*$	Strain hardening exponent as per modified equation

P	Laser power, KW
$P_{max}$	Maximum applied load by fatigue tester on test samples, KN
$P_{mean}$	Average load applied by fatigue tester on test samples, KN
R	Stress ratio
$T_0$	Ambient temperature, K
$T_{max}$	Maximum temperature, K
$\sigma$	True stress, MPa
$\sigma_{min}$	Minimum stress, MPa
$\sigma_{max}$	Maximum stress, MPa
$\sigma_a$	Stress amplitude, MPa
$\sigma_m$	Mean stress, MPa
$\sigma_y$	Yield strength, MPa
$\sigma_\varepsilon$	Effective stress, MPa
$\varepsilon_\varepsilon$	Effective strain
$\varepsilon$	True Strain
$\varepsilon_y$	Yield strain
$\mu$	Co-efficient of friction

$F$	Compressive force, KN
$r_0$	Radius of the shoulder of the friction stir weld tool, mm
$r_i$	Radius of the pin of the friction stir weld tool, mm
$h$	Height of the pin of friction stir weld tool, mm
$\omega$	Angular velocity of the friction stir weld tool, rpm
$v_o$	Welding speed of the friction stir weld tool, mm/s
$s$	Scale factor
$H_c$	Hardening capacity

# CHAPTER 1

## INTRODUCTION

Rising concern about global warming that is directly affected by vehicle emissions can be reduced to an extent if the total weight of each car can be decreased. A report published by USAMP (United States Automotive Materials Partnership) expressed the vision of increasing the use of magnesium alloys by 340 lbs per car by the year of 2020 (only about 10~12 lbs of magnesium alloys were used in a typical car in 2006), which will lead to a substantial reduction of the car weight (about 15%). In a January 2007 article, IIHS (Insurance Institute of Highway Safety) stated "a way to improve fuel economy and maintain vehicle crashworthiness is to use lighter materials that reduce vehicle weight but not size." IIHS also noted "some weight reduction, especially among very heavy vehicles, could improve total safety by lowering the risk to other people on the road."

To achieve that goal, it is essential to consider lightweight alloys with good formability as a substitute of some structural parts considered. Magnesium alloys have attracted special attention of researchers and engineers especially working in the transportation industry because they are the lightest structural metallic materials with high specific strength and stiffness, good heat conductivity, high electromagnetic interference shielding and damping capabilities, good machinability and castability [1-4]. To increase the application of Mg alloys in the automotive and aircraft industries, welding and joining would inevitably be involved. In this regard, mechanical properties such as strength (tensile and fatigue), ductility, strain-hardening behavior, strain-rate sensitivity, etc., of

all welded joints used in structural applications must be evaluated to ensure the integrity and safety of the joint and structure. However, till now, comparisons of different welded joints in Mg alloys in terms of mechanical properties on Mg alloy are very limited. For the FSW of Mg alloys the weld pitch of  $v/\omega$  (welding speed/rotational rate) has been limited to between 0.0144 and 0.402 mm/rev [5-8], and it is not known what will happen if the welding pitch is increased beyond this range. Some limited work on the fiber laser welding (FLW) of Mg alloys has also recently been reported [9-10]. Thus, the aim of the present study was to compare different welded joints of AZ31B Mg alloy in terms of microstructural evaluation, micro-hardness, tensile properties, strain hardening and fatigue properties.

A literature survey is presented in Chapter 2 on Mg alloys and their properties. Basic principles of different welded joints along with published results of microstructural evaluation, tensile and fatigue properties of the welded joints are also discussed. Chapter 3 gives the experimental procedures involved in this study. Chapters 4 and 5 present the test results obtained in this work. Microstructural characterization, micro-hardness, tensile and fatigue properties of extruded AZ31B and welded joints are presented and analyzed in those two Chapters. Chapter 6 presents summary, conclusions and future scope of the relevant work.

# **CHAPTER 2**

## **LITERATURE REVIEW**

### **2.1 Magnesium and Its Alloys**

Magnesium was discovered and isolated in 1808, but it took about 100 years before a real demand for magnesium developed. The uses of magnesium as a structural material were, however, very few. The bulk was used as an alloying element in aluminum alloys. Since 1993, there has been renewed interest in using magnesium based alloys in automobile, aerospace and household and sport applications. The driving force is the weight saving. Magnesium is substantially less dense than aluminum. It is also relatively expensive to produce, not as easily worked as aluminum, relatively few developed alloys exist, no secondary recycling procedure has been developed and there are questions as to corrosion resistance, safety and reliability; all factors which prevent its wide acceptance. Unless the automobile industry embraces its use, magnesium might not become economically viable in other fields [11].

### **2.2 Physical Metallurgy and Properties**

Magnesium and magnesium alloys have been employed in a wide variety of structural applications because of their favorable combination of tensile strength (160 to 365 MPa), elastic modulus (45 GPa) and low density (1.74 gm/cm<sup>3</sup>). Magnesium alloys have high strength-to-weight ratios and relatively good electrical conductivity and thermal

conductivity. They have also high damping capacity, that is, the ability to absorb elastic vibrations.

Magnesium is a silvery white metal. It is the sixth most abundant metal on earth. Table 2-1 shows the physical properties of magnesium and other structural materials. Its density is less than one quarter that of iron and two-thirds that of aluminum. The melting point and specific heat of magnesium are almost the same as those of aluminum. The Young's modulus and shear modulus of magnesium are about two-thirds of those of aluminum. Another aspect is good damping behavior. Pure magnesium shows even higher damping properties than cast iron, although these properties are highly dependent on the prior heat treatment [12].

Table 2-1 Physical properties of metals [12].

	Mg	Al	Ti	Fe	Cu
Lattice Structure	HCP	FCC	HCP	BCC	FCC
Density (gm/cm <sup>3</sup> )	1.74	2.70	4.51	7.87	8.98
Melting Point (°C)	650	660	1668	1535	1083
Specific Heat (cal/m.°C)	0.24	0.22	0.13	0.11	0.09
Young's Modulus (GPa)	45	76	114	190	136
Shear Modulus (GPa)	17	26	45	80	44
Thermal Conductivity (W/m.K)	167	238	16	73	394

Figure 2.1 shows the lattice structure and slip systems of magnesium. Magnesium with a structure has poor formability at room temperature because of its HCP structure. The

directions for easy crystallographic slip in HCP single crystals are closed packed directions. At low temperatures, the three dominant sets of planes which contain this slip direction are (0001) $\langle$ 11-20 $\rangle$  basal plane. The activation of pyramidal and prismatic slip systems in polycrystalline aggregates occurs primarily due to the high temperature and large stresses generated in grain-boundary regions because of the misorientation between neighboring grains. Thus, magnesium has high ductility at elevated temperatures, because of the activation of three prismatic slip systems of  $\{10\bar{1}0\}\langle$ 11-20 $\rangle$  and the six pyramidal slip systems of  $\{10\bar{1}1\}\langle$ 11-20 $\rangle$  [15]. Therefore, commercially available magnesium is deformed normally at elevated temperature. For example, plastic processes for magnesium, such as rolling, forging and extrusion, are usually performed at elevated temperatures.

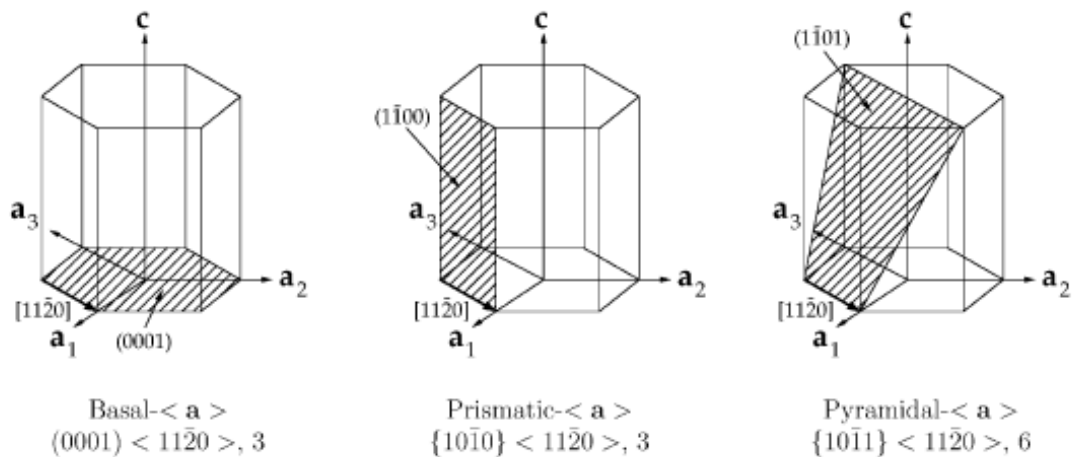


Figure 2.1: Basal, Prismatic and Pyramidal slip systems in pure magnesium [13].

## 2.3 Types of Magnesium Alloys

For the materials where only alloying can lead to sufficient strength for construction purposes, for practical design, two categories of magnesium alloys are usually used:

- This type of Mg alloys contains 2-10% of Al, with minor content of Zn and Mn. The production cost for this type of alloys is relatively low and the mechanical properties of alloys deteriorate rapidly at higher temperature.
- This type contains wide variety of chemical elements, such as, Zn, Th, Ag, Si, with low content of Zr, which means close-grained structure and higher mechanical strength. These alloys have better properties at higher temperatures but their production cost is very high because of the expensive elements and the special production technology.

Aluminum is the most commonly used alloying element and forms the basis of the die casting alloys. Maximum solubility of Al in magnesium is 12.7 wt % and alloys in excess of 6 wt % can be heat treated. Aluminum improves strength, the optimum combination of strength and ductility being observed at about 6%. The alloys are readily castable [11]. Zinc is used as an alloying element to increase the strength of the alloys by solid solution and precipitation. However, it reduces the ductility of the Mg alloys [14]. Manganese is usually not employed alone but with other elements, e.g., Al. In this case, compounds such as  $MnAl$ ,  $MnAl_6$  or  $MnAl_4$  are formed. Mn reduces the solubility of iron and produces relatively safe compounds. It increases the yield strength and improves salt water corrosion resistance of Mg-Al and Mg-Al-Zn alloys. Binary alloys are used in forgings or extruded bars. The maximum amount of manganese is 1.5-2 wt %. [11].

According to a different classification, magnesium alloys are divided into casting alloys, wrought alloys, composites and powder materials. Most magnesium alloys show very good machinability and processability [15]. Cast, moulded and forged parts are inert gas weld-able and machinable. Along with the excellent properties, there are some disadvantages to the application of these alloys. The cold working ability of the magnesium alloys is very poor and the corrosion resistance is very low. Again, when cast, magnesium has a high mold shrinkage, about 4% when solidifying and about 5% during cooling. This high degree of shrinkage leads to microporosity and low toughness that cannot be ignored [12].

The negative properties mentioned above kept engineers away from accepting magnesium alloys as a competitive replacement for aluminium and steel. Therefore, attempts have been made to improve the characteristic profile of Mg alloys by employing different alloying elements.

Till now, the main fabrication route of magnesium alloy parts remains die-casting because of its high productivity and dimensional accuracy. It is well known that wrought magnesium alloys have superior mechanical properties than cast alloys. Often these superior properties are attained through hot working such as rolling, forging and extrusion during which the grains are greatly refined.

## **2.4 Double Sided Arc Welding**

Double-sided arc welding (DSAW) developed at the University of Kentucky employed a different technique to improve the arc concentration. Figure 2.2(a) is a regular arc welding system. As can be seen, the regular arc welding system uses an electrical

connection (ground cable) between the workpiece and power supply to allow the welding current to complete the loop. The electric arc is established between the workpiece and the torch. In the DSAW system shown in Figure 2.2(b), the workpiece is disconnected from the power supply and a second torch is placed on the opposite side of the workpiece to complete the current loop. As a result, electric arcs are simultaneously established between the workpiece and each of two torches. Although DSAW can be implemented using different torch combination, this study will focus on the case where a plasma arc welding (PAW) torch and a gas tungsten arc welding (GTAW) torch are used as the primary and secondary torch, respectively [16].

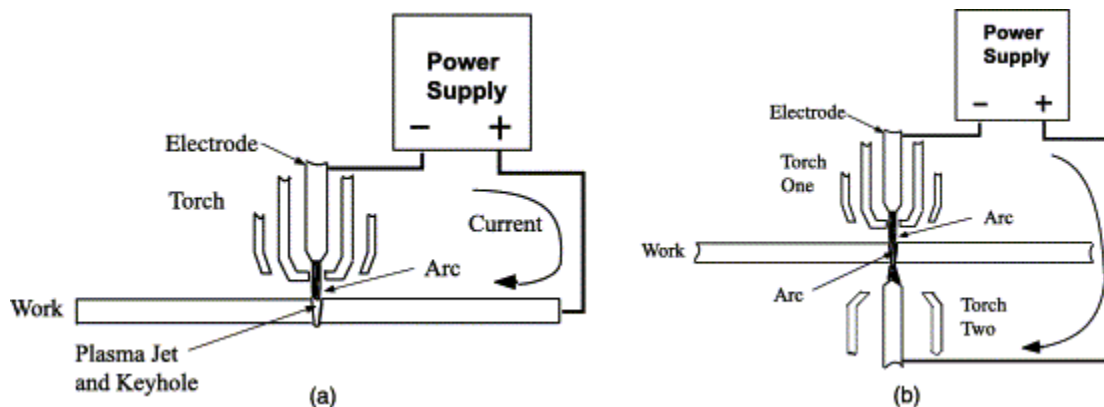


Figure 2.2: Schematic diagrams of welding systems. (a) Regular welding system and (b) double sided arc welding system [16].

Studies have shown that DSAW has certain unique characteristics. First, in DSAW process, the current has to flow through the thickness of the workpiece. This direction of current is referred to as through-the-thickness (TTT) direction. However, in regular arc welding, the TTT direction does not exist because the majority of the welding current flows from the arc into the surface of the workpiece. Second, the unique TTT direction of

the current results in a presence of the current in the keyhole. Because of the presence of the arc in the keyhole, an arc column is established along the keyhole. DSAW thus has a unique energy compensation and radial heating mechanism which helps produce deep narrow penetration. However, in regular keyhole PAW, the plasma jet, as an electrically neutral mix of ions and electrons, only consumes its initial energy, gained before entering the keyhole, when it travels along the keyhole TTT. Of course, the most pronounced characteristic of DSAW process is its symmetric hour glass-shaped weld, due to the symmetric double-sided and radial heating. This unique characteristic, together with the deep narrow penetration capability, makes DSAW a promising competing process for joining large metal structures.

At the University of Kentucky, technologies have been developed to double-sided arc weld aluminum alloys, stainless steels, and mild steels. Plates up to 12.7 mm (1/2 in.) thick can be welded in a single pass without bevels. In particular, an adaptive control technology has been developed which can guarantee the desired full penetration despite variations in root opening and mismatch and thus makes DSAW an attractive practical production process. A shipyard's preliminary study concluded that DSAW process has potential use in making butt welds in ship structure manufacturing. However, despite the success in experimental verification and control system, limited studies have been done to analyze and to understand the physical processes occurring during DSAW. Such studies will play a fundamental role in verifying the unique characteristics of DSAW as well as in designing the welding parameters to meet the requirements in different applications [16].

## 2.5 Friction stir welding

Friction-stir welding (FSW) is a solid-state joining process (meaning the metal is not melted during the process) and is used for applications where the original metal characteristics must remain unchanged as far as possible. This process is primarily used on aluminum, and most often on large pieces which cannot be easily heat treated post weld to recover temper characteristics. It was invented and experimentally proven by Wayne Thomas and a team of his colleagues at The Welding Institute UK in December 1991 [17].

Figure 2.3 presents a schematic of the friction-stir welding process. In this process, a cylindrical-shouldered tool, with a profiled threaded/unthreaded probe (nib or pin) is rotated at a constant speed and fed at a constant traverse rate into the joint line between two pieces of sheet or plate material, which are butted together.

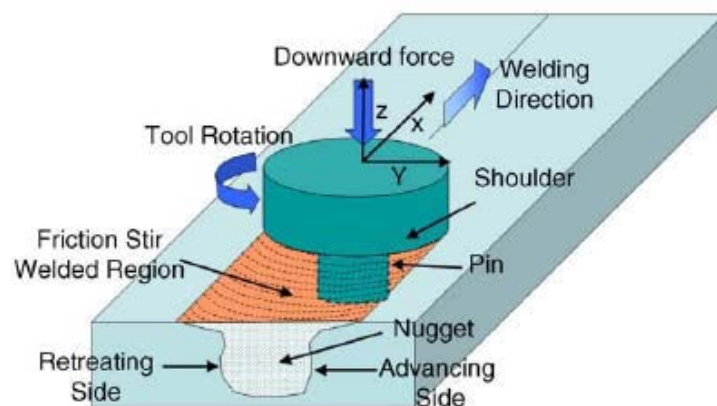


Figure 2.3: A schematic of friction-stir welding process [18].

The parts have to be clamped rigidly onto a backing bar in a manner that prevents the abutting joint faces from being forced apart. The length of the nib is slightly less than the weld depth required and the tool shoulder should be in intimate contact with the work surface. The nib is then moved against the work, or vice versa. Frictional heat is generated between the wear-resistant welding tool shoulder and nib, and the material of the work pieces. This heat, along with the heat generated by the mechanical mixing process and the adiabatic heat within the material, cause the stirred materials to soften without reaching the melting point (hence cited a solid-state process), allowing the traversing of the tool along the weld line in a plasticised tubular shaft of metal. As the pin is moved in the direction of welding, the leading face of the pin, assisted by a special pin profile, forces plasticised material to the back of the pin while applying a substantial forging force to consolidate the weld metal. The welding of the material is facilitated by severe plastic deformation in the solid state, involving dynamic recrystallization of the base material [18].

For any welding process it is, in general, desirable to increase the travel speed and minimise the heat input as this will increase productivity and possibly reduce the impact of welding on the mechanical properties of the weld. At the same time it is necessary to ensure that the temperature around the tool is sufficiently high to permit adequate material flow and prevent flaws or tool fracture.

The total energy generated per unit length of the weld is the sum of the energy generated due to friction between the tool and the workpiece surface and the plastic deformation within the workpiece. Thus, the total energy generated during FSW can be expressed as follows [18],

$$E_{total} = 2\mu F \left( \frac{1}{3} r_o + \frac{r_i^2}{r_o^2} h \right) \frac{\omega}{v_o} + s \sigma_\epsilon \epsilon_\epsilon (2r_i h) \quad (2)$$

where  $\mu$  is the coefficient of friction,  $F$  is the compressive force,  $r_o$  is the radius of the shoulder,  $r_i$  is the radius of the pin,  $h$  is the height of the pin,  $\omega$  is the tool angular velocity in rpm (rev/min),  $v_o$  is the welding speed,  $s$  is a scale factor,  $\sigma_\epsilon$  is the effective stress and  $\epsilon_\epsilon$  is the effective strain. In chapter 4 the effect of heat input along with transverse speed  $\omega$  and welding speed  $v_o$  are discussed in details.

## 2.6 Fiber Laser Welding

Fiber laser welding is best employed for keyhole welding. The laser is focused so as to achieve a very high power density (typically at least 1 MW/cm<sup>2</sup>) at the work piece. At the center of the focused beam (where the laser power density is usually highest) the metal actually vaporizes, opening up a blind hole (the keyhole) into the molten metal pool. Vapor pressure holds back the surrounding molten metal and keeps this hole open during the process. This metal vapor also re-radiates laser energy into the molten metal along the side of the keyhole, thus transferring energy through the entire depth of the keyhole and resulting in a weld with a deep aspect ratio. The small size of keyhole region results in a relatively small fusion zone and heat affected zone. Furthermore, the highly localized application of heat means that the work piece both heats up and cools down rapidly which can minimize grain growth in high strength, low alloy steels. Even though no filler material is typically used for keyhole welding, the high temperatures of keyhole welding can vaporize volatile materials, producing a different composition in the fusion zone than

in the base metal. Also with hardenable steels, the rapid cooling generates fully martensitic fusion zones and hardened heat affected zones [19].

## **2.7 Diode Laser Welding**

Diode lasers are best employed for conduction mode welding of thin metals for applications in which cost is a prominent factor (both purchase price and operating costs) and in which practical considerations such as floor space and part access are important. Indeed, their small size and low weight mean that these laser systems can be mounted directly on robot arms and moved relatively quickly. Alternatively, the ability to deliver the output through long lengths of optical fiber allows a high level of flexibility in terms of where the laser system is located. It also enables beam delivery into tight or hard to access spaces. Typical uses would therefore be under-hood welding of components in automobile manufacturing and welding of heat-sensitive medical devices such as pacemakers. Conduction mode welding with diode lasers is well suited for stainless steel, particularly in applications where the corrosion resistance of the weld is critical. Typical examples are in medical devices, reactors and aerospace components. Again, this is because the lower process temperature does not cause removal of more volatile alloying elements from the fusion zone. Additionally, stainless steels are generally increasingly reflective at longer wavelengths so the shorter wavelength of the diode laser results in incrementally better light absorption and thus higher efficiency than with older laser types. The higher absorption of shorter wavelength light is even more pronounced in aluminum which has a very significant dip in its reflectivity in the near infrared. Aluminum alloys containing volatile alloying materials such as magnesium, which are

difficult to keyhole weld can thus be successfully conduction welded with diode lasers. Since, the density of diode laser is low and the welds are produced in the conduction mode the welding speeds are limited, to achieve the full penetration [20].

## 2.8 Previous Studies

A lot of studies on the fusion welding of Mg alloys have been reported [21-34]. For example, Weisheit *et al.* [30] carried out CO<sub>2</sub> laser welding of different Mg alloys and showed that most Mg alloys could be easily welded without serious defects, except AZ series and AM series with extremely high porosity. Zhao and Debroy [31] investigated the formation of porosity in AM60 Mg alloy during laser welding and concluded that hydrogen in the parent material was the main origin of porosity in the welds and thus suggested remelting as a remedy measure. Sun *et al.* [32] evaluated TIG, CO<sub>2</sub> and pulsed Nd:YAG laser welded joints of AZ31 sheet and reported that TIG welding could be used to achieve welds without defects but with coarser grain sizes that could reduce the mechanical properties. Sun *et al.* [34] employed Nd:YAG laser on AZ31B Mg wrought alloy and observed that weld penetration increased by adding oxide fluxes (TiO<sub>2</sub>, SiO<sub>2</sub>, Cr<sub>2</sub>O<sub>3</sub>). While the as-welded FZ with oxide fluxes had a deeper weld penetration, the tensile strengths of the welded joints with activating fluxes were lower due to the presence of larger grain sizes in the FZ. This was attributed to the fact that the absorptivity of laser energy increased, i.e., more energy was absorbed by the flux coat which was transmitted to the specimen in the early period of laser interaction. Quan *et al.* [35] studied the effects of heat input on microstructure and tensile properties of laser welded AZ31 Mg alloy. Liu and Dong [36] reported the effect of microstructural changes

on the tensile properties in non-autogenous gas tungsten arc welded AZ31B magnesium alloy. Zhu *et al.* [37] presented the effect of welding parameters on the welding defects and change of microstructure in CO<sub>2</sub> and diode laser welded AZ31B magnesium alloy. A lot of studies on the FSW of magnesium alloys have been reported, including microstructural evaluation [15, 38, 39-42] and tensile properties [5-7, 15, 40, 43-46] in relation to the welding parameters. Abbasi *et al.* [8] studied the influence of  $\omega/v$  (ratio of rotational rate to welding speed) on the mechanical properties of the FSWed samples, while Seidel and Reynolds [46] reported that  $v/\omega$  ratio, rather than  $\omega/v$  ratio, is an important parameter for the FSWed joints and referred to this ratio as the weld pitch of the FSWed joint since the specific weld energy (Joule/meter) is associated with the weld pitch, i.e., the energy generated per unit length of weld decreases with increasing weld pitch. For the FSW of Mg alloys the weld pitch of  $v/\omega$  has been basically limited to relatively small values ranging between 0.00024 and 0.0067 mm/(s.rpm)<sup>1</sup> (i.e., 0.0144 and 0.402 mm/rev) within which the yield strength (YS) and ultimate tensile strength (UTS) were observed to increase only slightly with increasing weld pitch [5-8]. Still, it is unclear how the YS and UTS further change if the weld pitch is beyond this range.

On the other hand, to improve the mechanical properties and ensure the integrity of the FSWed joints it is essential to ascertain the flow behavior of materials during FSW. Li *et al.* [47] described the material flow as a chaotic-dynamic mix in FSWed dissimilar Al alloys. Colligan [48] studied material flow pattern of the FSWed Al alloy via a stop action technique using a FSW pin tool with left hand thread (LHT) in the clockwise rotation and obtained superior welded joints and stated that the material flow was

---

<sup>1</sup> 1 mm/(s.rpm) = 60 mm/rev.

dependent on the exact tool geometry and welding parameters used. Reynolds [49] and Seidel and Reynolds [46] reported flow visualization during FSW process on AA2195-T8 alloy by a marker insert technique (MIT), which allowed the determination of the position of material pre- and post-welding in the thermo-mechanically affected zone (TMAZ) through a serial sectioning technique. Then three-dimensional plots of the deformed markers could be obtained and they provided a good qualitative characterization of the material flow in friction stir welds. But Zhang *et al.* [50] pointed out that the insertion of the marker material in the weld line could alter the nature of material flow in the weld due to different material flow characteristics of the base and marker materials and the introduction of additional interfaces. They also reported that the formation of pores in the FSWed magnesium alloys was due to insufficient pressure underneath the shoulder. But there was little information available on the role of tool geometry on the defect formation. The important contribution to material flow visualization was done by Fratini *et al.* [51] who incorporated the material flow and analysis with microstructural evaluation. Guerra *et al.* [52] and Schnider and Nunes [53] extensively studied and characterized the flow pattern of FSWed joints. They emphasized the importance of the threaded pin tool profile and pointed out that the material flow was driven by the threads on the pin tool and was reversed if the direction of the threads or the direction of the tool rotation was reversed. Colegrove and Shercliff [54] proposed a three-dimensional material flow model around the threaded tool and observed that the unthreaded tool had a lower traversing force than the threaded pin. Ulysse [55] modeled the effects of tool speeds, both rotational and linear, on forces and plate temperatures during FSW of thick aluminum plates based on a three-dimensional viscoplastic model.

Nandan *et al.* presented the results of a three dimensional material flow and heat transfer model during FSW of 6061 Aluminum alloy [56] and 304 austenitic stainless steel [57]. Schmidt *et al.* [58] investigated the 2D and 3D flow patterns in the highly deformed zone at the tool/matrix interface in FSW using marker material along with the measurements of the deposition distance, tool travel distance, stream line path distance, average velocity of a material point flowing along a stream line. Zhang *et al.* [59] studied 3D material flow in FSW under different processing parameters using a finite element technique based on the nonlinear continuum mechanics, and observed a quasi-linear relation between the change of the axial load on the shoulder and the variation of the equivalent plastic strain. They also observed that the equivalent plastic strain was larger near the top surface than near the bottom surface which could be attributed to the larger plastic flow near the top surface created by the mechanical action of the rotating shoulder. Hamilton *et al.* [60] proposed a model in which the surface material from the retreating side was extruded into the plasticized material zone within the weld thickness. However, the efficacy of the model was limited to specific conditions and assumptions involving steady-state material flow. Gerlich *et al.* [61] studied the material flow and intermixing during friction stir spot welding of both lap and butt dissimilar Al alloy sheets, and observed that in both similar and dissimilar friction stir welds a helical vertical rotational flow was created within the intermixed region and formed beside the periphery of the rotating pin. Kumar and Kailas [62] recently studied the defect formation and the mechanism of friction stir weld formation. Zhao *et al.* [63] examined the influence of the pin tool profile on the mechanical properties in the FSWed Al alloy and reported that the LHT pin tool in the clockwise rotation produced an extra downward force and increased heat generation that

would be beneficial for accelerating the flow of plasticized material and ensuring good mechanical bonding. Guerra *et al.* [52] further noted specifically that nib or pin is usually threaded and turned in such a direction that the material is pushed down by the threads (for example, a right hand thread pin tool turning counterclockwise or left hand thread pin tool turning clockwise). Changing either the rotational direction or the thread orientation of the pin tool could cause inferior welded joints that were proven by Cao and Jahazi [15] who observed the appearance of notable defects at the root of the FSWed Mg joints using a right hand thread pin tool in the clockwise rotation.

## **2.9 Research Objective**

Based on the literature, it is clear that a suitable welding method for Mg alloy is yet to be found. The fatigue properties are important in design consideration as the automotive and aerospace components are inevitably subjected to dynamic or cyclic stresses in service, however, no studies of fatigue behavior of fiber laser welded (FLWed), diode laser welded (DLWed) and double sided arc welded (DSAWed) Mg joints were found in the open literature. Thus, the aim of the present investigation was to:

- Evaluate and compare the microstructure, tensile properties, strain hardening, strain rate sensitivity and fatigue properties of double sided arc welded and friction stir welded AZ31B Mg alloy sheet.
- Evaluate and compare the microstructure, tensile properties, strain hardening, strain rate sensitivity and fatigue properties of diode laser welded and fiber laser welded AZ31B Mg alloy sheet.

- Observe the change of mechanical properties of the friction stir welded joints by using right hand thread and left hand thread weld tool and different welding parameters and also to evaluate the effect of the weld pitch on the tensile properties.

# CHAPTER 3

## EXPERIMENTAL PROCEDURE

### 3.1 Materials and Composition

Extruded wrought AZ31B Mg alloy was selected in this study. The material was developed and provided by General Motors Research and Development Center through Waterloo University, Waterloo, Canada. The chemical composition of the alloy is listed in Table 3-1.

Table 3-1 Chemical composition of AZ31Mg alloy (weight %).

<b>Al</b> <b>(wt%)</b>	<b>Zn</b> <b>(wt%)</b>	<b>Mn</b> <b>(wt%)</b>	<b>Fe</b> <b>(wt%)</b>	<b>Ni</b> <b>(wt%)</b>	<b>Cu</b> <b>(wt%)</b>	<b>Mg</b> <b>(wt%)</b>
2.5-3.5	0.7-1.3	0.2-1.0	0.0035	0.0007	0.0008	Balance

Four different welded joints namely, friction stir welding (FSW), double sided arc welding (DSAW), fiber laser welding (FLW) and diode laser welding (DLW) were employed to make autogenous welds between the work-pieces in the butt joint configuration. The FSW was received from CANMET research laboratory, Montreal, Canada. The rest of the three welded joints are received from Waterloo University, Waterloo, Canada. All welded joints were made with the welding direction perpendicular to the rolling direction of the sheet. Prior to welding, surface oxides were removed with a

steel brush and then the surface was cleaned using ethanol as well. The welding parameters for those welding methods are listed in Table 3-2

Table 3-2 Welding parameter of all welded joints

<b>Welding Method</b>	<b>Welding speed (mm/s)</b>	<b>Rotational rate (clockwise) rpm</b>	<b>Thread of the weld tool</b>	<b>Welding power (KW)</b>
FSW	30	2000	Left-hand	-
	20	do		
	10	do		
	20	1000		
	10	do		
	5	do		
	10	2000	Right-hand	
DSAW	25	-	-	1.4
FLW	100	-	-	2
DLW	8.3	-	-	3

### 3.2 Sample Preparation and Testing

The experimental tests were conducted and metallographic sample are prepared in the Mechanical Engineering Department laboratories at Ryerson University.

### **3.2.1 Metallography**

All metallographic samples for microstructural characterization were taken from the cross section perpendicular to the extrusion direction and were cold mounted using Lecoset 7007 resin (mixing ratio: 2 parts of resin added to 1 part of catalyst). Hot mounting was avoided to prevent any possible microstructure change due to the effect of temperature during sample preparation.

The mounted samples were manually ground with SiC papers up to a grit of #1200 with water as the lubricant and then polished with 6 $\mu$ m and 1 $\mu$ m diamond paste followed by finer Master-Prep solution. The polishing lubricant for the diamond paste was a mixture of rust inhibiting solution and distilled water (10% solution by volume). Due to the reactive nature of magnesium in the presence of water, ethanol was used as a cleaning agent during the polishing stages.

Two etchants were used individually. Etchant 1 (a solution of 10 ml acetic acid, 4.2 g picric acid, 10 ml distilled water, and 70 ml ethanol (95%)) was used to reveal the microscopic structure (grain boundaries) of the alloys and etchant 2 (same composition but no distilled water) was used to reveal the dendrites in the fusion zone (FZ) of the welded joints.

### **3.2.2 Quantitative Image Analysis**

Microscopic images were taken using a light microscope and image analyses were subsequently performed using Clemex software to obtain the grain size. The Clemex image analysis system was comprised of Clemex CMT software adaptable to ASTM

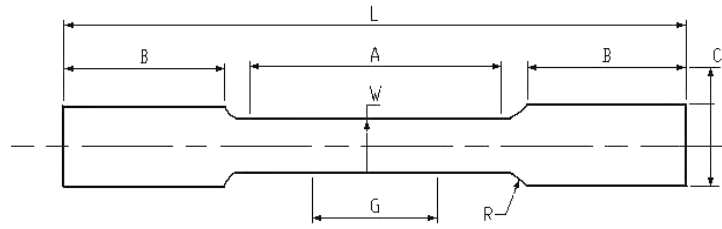
standards, a Nikon optical microscope (10× eye piece, five different object lenses with magnifications of 5×, 10×, 20×, 40×, and 100×), a high-resolution digital camera, and a high performance computer to carry out the detailed analysis.

### **3.2.3 Micro-hardness Tests**

A computerized Buehler microhardness testing machine was used for the micro-indentation hardness tests where a load of 100 g and duration of 15 s were used. The test results were recorded in the computer using a Hyper Terminal. Vickers microhardness tests were performed on the unetched samples. All the indentations were adequately spaced to avoid any potential effect of strain fields caused by adjacent indentations.

### **3.2.4 Tensile Tests**

The samples for tensile tests were prepared according to the ASTM E8M [64] standard for sub-sized sheet type material (i.e., 25 mm gauge length and 6 mm gauge width). The specimen dimensions are shown in Figure 3.1. All samples for the tensile tests were taken parallel to the extrusion direction. The tests were carried out using a computerized United testing machine at four different strain rates:  $1 \times 10^{-2} \text{ s}^{-1}$ ,  $1 \times 10^{-3} \text{ s}^{-1}$ ,  $1 \times 10^{-4} \text{ s}^{-1}$  and  $1 \times 10^{-5} \text{ s}^{-1}$ . All the tests are conducted at room temperature. After tensile tests, fracture surfaces were examined using a high performance JSM-6380LV scanning electron microscope (SEM) with an embedded energy dispersive X-ray spectroscopy (EDS) system which allows for seamless observations and has a high resolution of 3.0 nm.



<b>Dimensions in mm</b>	
G – Gauge length	25
W – Width	6
R – Radius	6.35
L – Overall length	140
A – Length of the reduced section	32
B – Length of the Grip Section	50
C – Width of the grip section	9.52

Figure 3.1: Geometry and dimensions of the sub-sized tensile/fatigue test specimen according to ASTM E8M [64].

### 3.2.5 Fatigue Tests

Fatigue tests were performed using a fully computerized servo-hydraulic INSTRON 8801 fatigue testing system. The samples for fatigue test were similar to the tensile testing samples. The tests were carried out in a stress control mode at different stress amplitudes. A stress ratio of  $R$  ( $\sigma_{\min}/\sigma_{\max}$ ) equal to 0.1, sinusoidal waveform, and frequency of 50 Hz were selected in all the tests. At each stress level at least two samples were tested.

# CHAPTER 4

## MECHANICAL PROPERTIES OF FRICTION STIR AND DOUBLE SIDED ARC WELDED AZ31B Mg JOINTS

### 4.1 Microstructure of the Base Metal

The microstructure of the AZ31B Mg base metal (BM) is shown in Figure 4.1, where elongated and pancake-shaped grains with varying sizes were observed. The heterogeneity in the grain structure of the BM was due to both deformation of the 2 mm thick sheet by rolling and incomplete dynamic recrystallization (partial annealing) [15].

The average grain size of the BM was about  $3.6 \pm 2.2 \mu\text{m}$ .

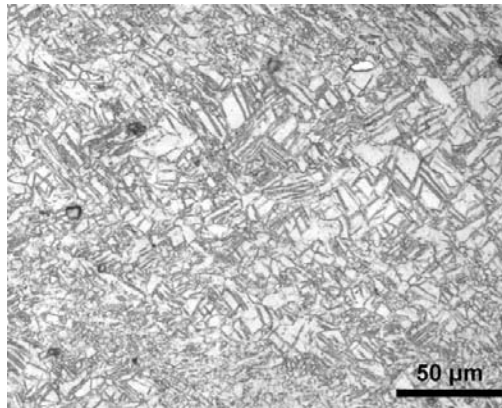


Figure 4.1: Typical microstructures of the base metal (BM) of the AZ31 Mg alloy.

### 4.2 Microstructure of the Friction Stir Welded Joint

The typical macroscopic and microscopic structures of FSWed Mg alloys are shown in Figure 4.2. Figure 4.2(a) shows the top weld bead after FSW and Figure 4.2(b) presents a

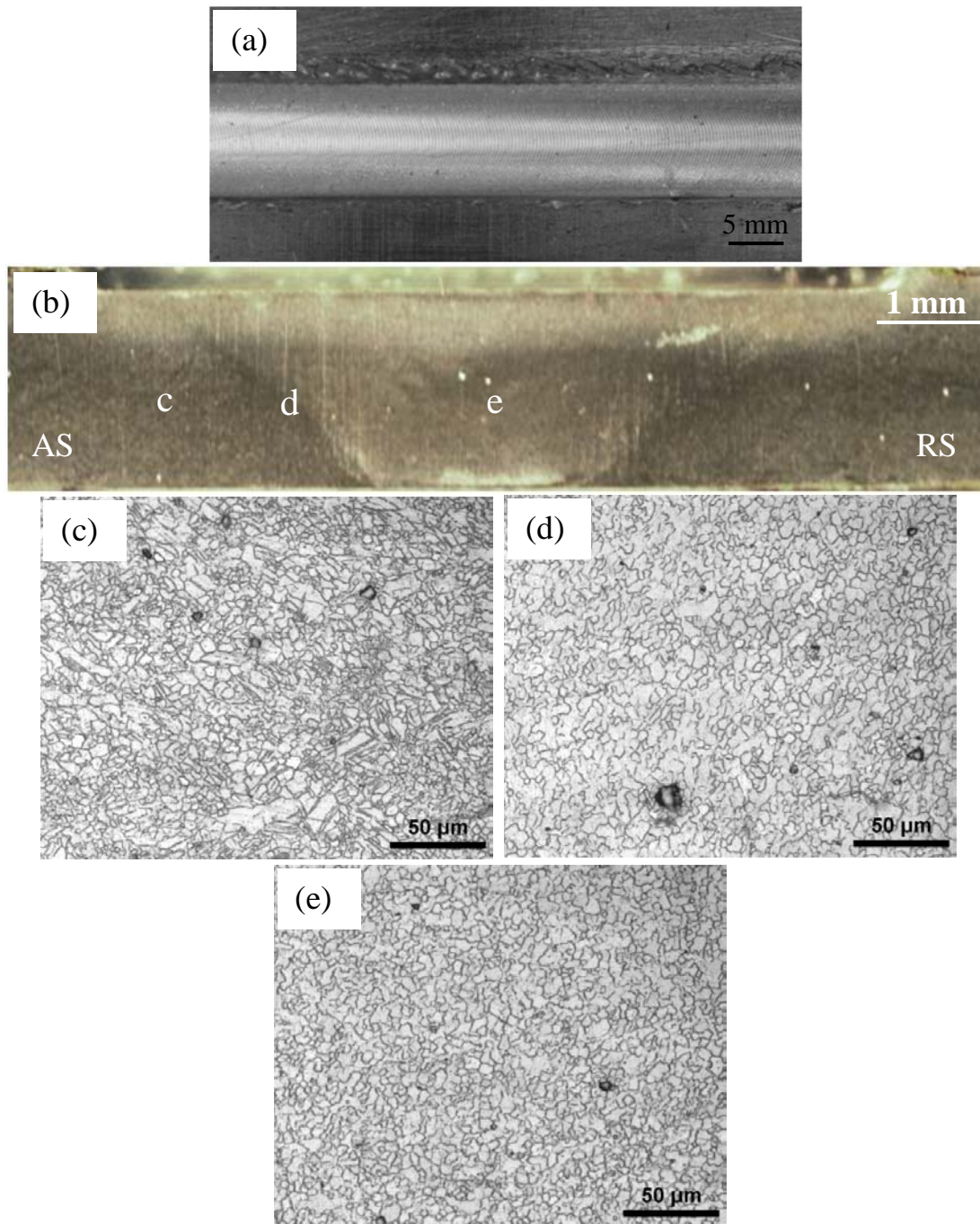


Figure 4.2: Typical macroscopic and microscopic structures of a friction stir welded (FSWed) AZ31 alloy. (a) Top weld bead surface, (b) cross-section of the welded joint, (c) heat-affected zone (HAZ), (d) thermomechanically-affected zone (TMAZ), and (e) stir zone (SZ).

typical cross-section of the FSWed sample including HAZ, thermo-mechanically affected zone (TMAZ) and stir zone (SZ). As seen in Figure 4.2(c), both equiaxed and elongated grains were present in the HAZ. However, in comparison to the BM (Figure 4.1), far more equiaxed grains appeared in the HAZ, indicating that partial recrystallization had also taken place during FSW. The recrystallization temperature of the alloy was approximately 250°C. Thus, the temperature in part of the HAZ may have been above this value. This is confirmed by some large grains observed in the HAZ due to grain growth after recrystallization [15]. The grain structure in the TMAZ (Figure 4.2(d)) in the present study is equiaxed and recrystallized, which was similar to the recent results reported by Cao and Jahazi [15] and Afrin *et al.* [5,42], while it was different from earlier observations [65] where the TMAZ was still characterized by deformed and elongated grains. The grains in the SZ were equiaxed (Figure 4.2(e)) and became noticeably bigger in the center of the stir zone (~8 µm). These changes were caused by dynamic recrystallization during FSW [66]. A larger grain size in the SZ was also reported by Cao and Jahazi [15], Afrin *et al.* [5,42], Pareek *et al.* [6], and Lim *et al.* [7].

#### **4.2.1 Effect of Welding Parameters**

The effect of the welding speed and rotational rate on the microstructure in the SZ is shown in Figure 4.3. The SZ microstructure consisted of recrystallized equiaxed grains, irrespective of the welding speed and rotational rate. However, the grain size was observed to decrease with increasing welding speed (Figure 4.3(a) → (b) → (c) and (d) → (e) → (f)), but increased- with increasing rotational rate (Figure 4.3(b) → (d) and (c) → (e)). As expected, the heat input and peak temperature decreased with either increasing

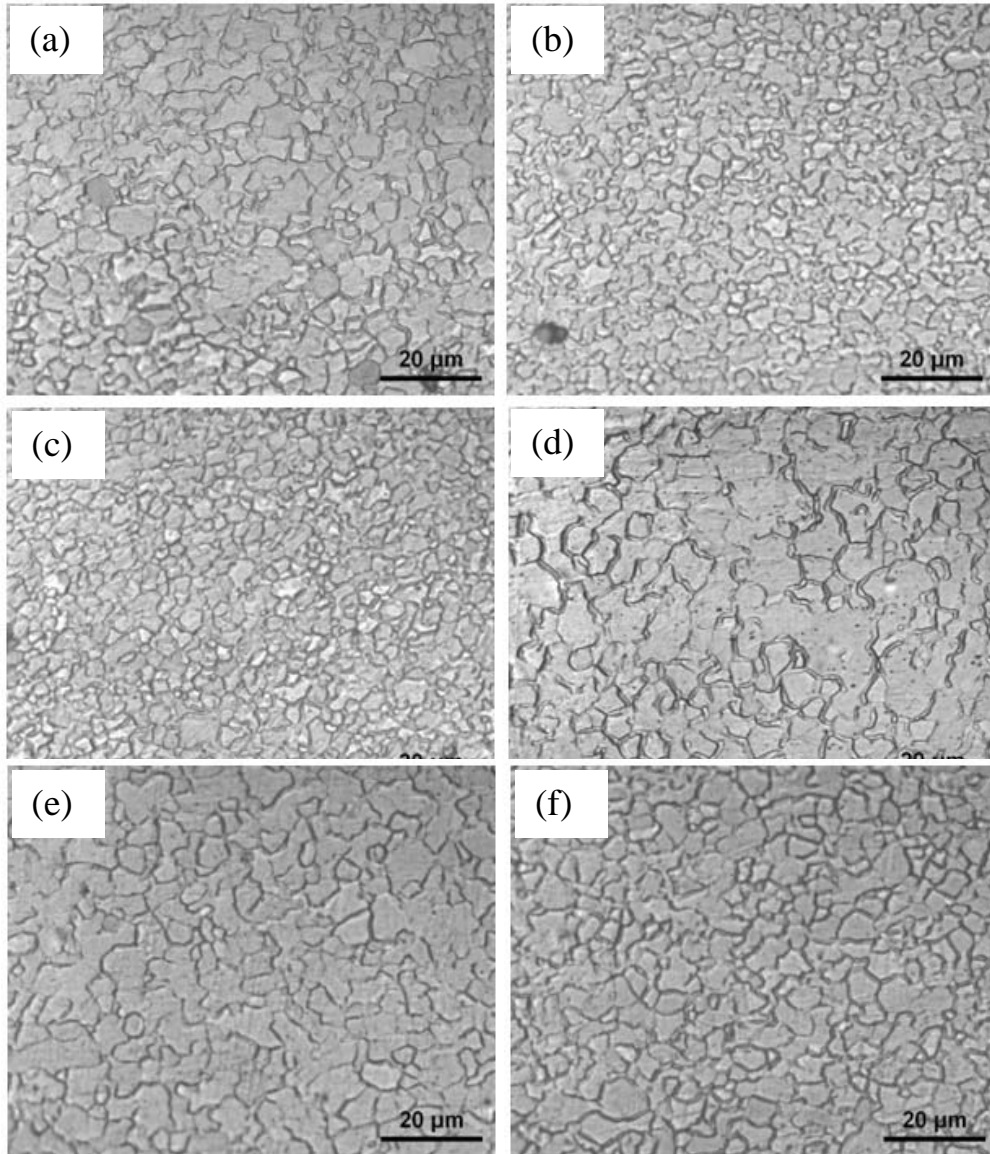


Figure 4.3: Effect of welding speed and rotational rate on the grain structure in the stirred zone at (a) 5 mm/s-1000 rpm, (b) 10 mm/s-1000 rpm, (c) 20 mm/s-1000 rpm, (d) 10 mm/s-2000 rpm, (e) 20 mm/s-2000 rpm, and (f) 30 mm/s-2000 rpm.

welding speed or decreasing rotational rate [15]. As a consequence, less time was available at higher welding speed and lower rotational rate for grain growth, giving rise to a smaller grain size.

### 4.2.2 Effect of Threads on Material Flow

While the left hand thread (LHT) pin tool turning clockwise gave good FSWed joints without visible defects, some cavity or lack-of-bonding defects occurred near the bottom surface of the FSWed joint when the right hand thread (RHT) pin tool was used and rotated in the same clockwise direction, as shown in Figure 4.4.

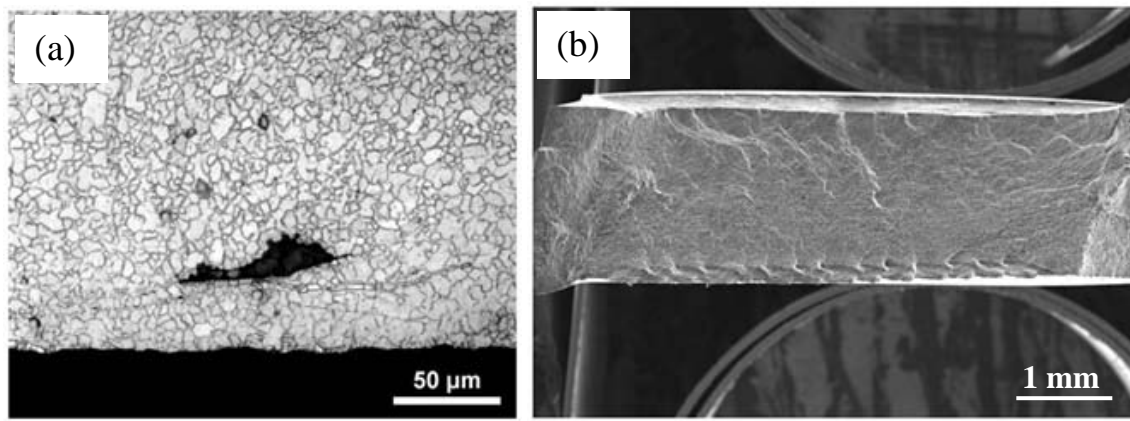


Figure 4.4: (a) Optical microscopic image and (b) SEM image of fracture surface of a FSWed joint made with a right hand thread (RHT) pin tool in the clockwise rotation at a welding speed of 10 mm/s and 2000 rpm.

This indicated a strong effect of pin thread orientation where the direction of material flow would be different when the pin tool with different thread orientations was used during FSW. Nunes *et al.* [67] also observed a similar effect and emphasized the importance of the rotational flow of material around the nib during FSW. They synthesized a model of material flow around the nib out of (1) a pure translation flow field, (2) a rigid disc rotation flow field (enclosing the nib), and (3) a radially symmetrical vortex ring flow field (inward at the shoulder, down at the nib threads, outward on the lower part of the nib and upward in the outer region around the nib to

complete the circulation). After further study Schnider and Nunes [53] predicted that, the direction of the material flow could be changed due to the change of threads of rotating tool while the direction of the tool rotation remained the same. To better understand this, a schematic illustration is shown in Figure 4.5, which illustrates how the flow directions of the material change by changing the pin thread while keeping the clockwise rotation.

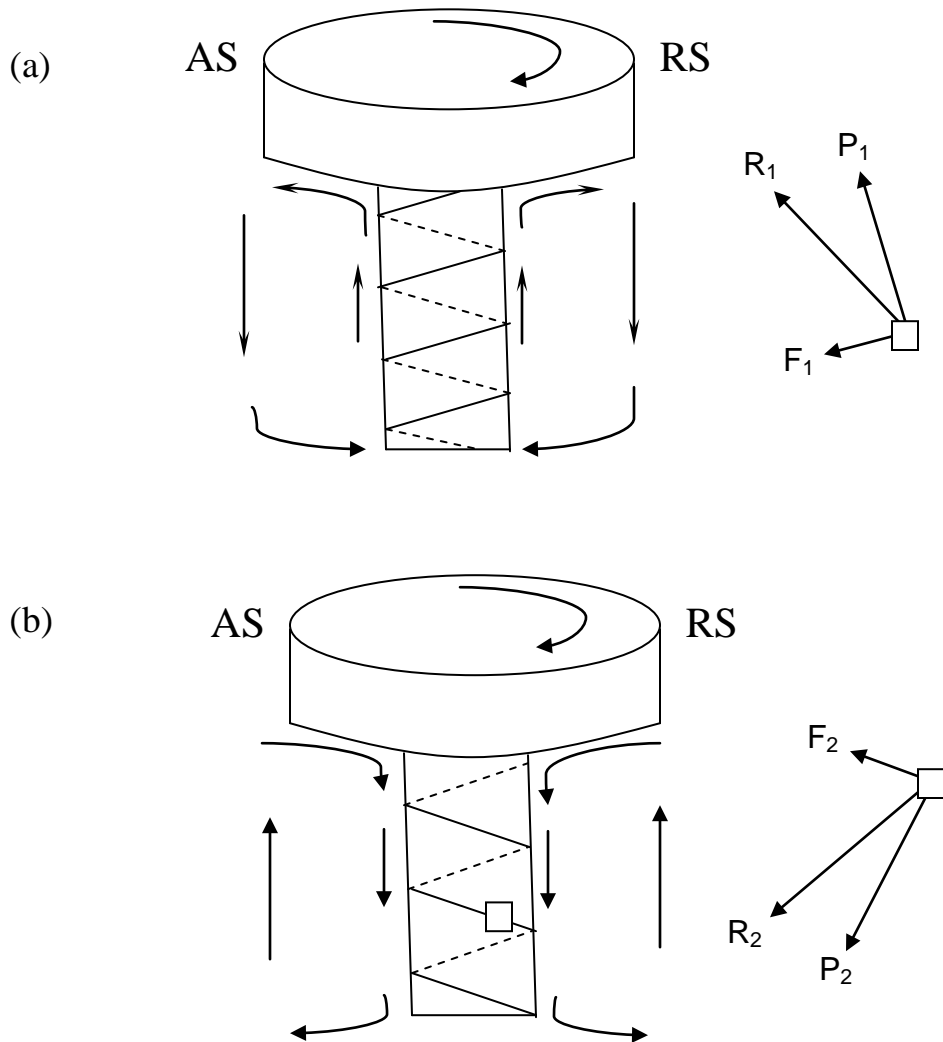


Figure 4.5: Schematic illustration of the plasticized material flow during FSW using (a) right hand thread (RHT) and (b) left hand thread (LHT) pin tools in the clockwise rotation.

In this figure, the rotating tool is moving into the page with the advancing side (AS) on the left and the retreating side (RS) on the right and the front side of the page indicated trailing side of the weld tool. From Figure 4.5(a) it is seen that the material flow around the RHT pin moved upward near the threaded pin. During FSW the plasticized material around the pin experienced two kinds of force. One was pressure  $P_1$  acting in the direction normal to the thread surface due to the rotation of the pin tool, and the other was traction force  $F_1$  which was parallel to the thread surface as a consequence of the friction between the thread surface and the plasticized material [68]. The orientation relationship of the forces exerted on the plasticized material in close contact with the thread surface of the RHT pin tool is schematically shown in Figure 4.5(a). The combined action of those two forces ( $P_1$  and  $F_1$ ) led to the plasticized material flowing upward from the bottom of the RS in a direction of  $R_1$  and deposited at the trailing side of the pin tool (or the front side of the page). It should be pointed out that the material flow was not a vertical upward flow, which was an inclined upward flow from the RS to AS at the trailing side as a result of the clockwise rotation. More plasticized material occurred as the weld tool rotated and thus the material moved continuously from the bottom of the screw thread to the shoulder of the rotating tool. Since FSW is a constant volume process [68] and the shoulder, the pin, the back plate and the undeformed BM restrict the flow path, the transported material underneath the shoulder is pushed into a downward direction to fill the cavity at the bottom of the joint that has already been created due to the inclined upward movement of the material in the vicinity of the thread. It should be noted that in the case of RHT pin tool rotating clockwise, there is no direct contact between the thread surface and the downward flowing plasticized material (Figure 4.5(a)).

On the other hand, for the LHT pin tool rotating clockwise, the plasticized material around the thread experiences pressure  $P_2$  and traction force  $F_2$ , as schematically illustrated in Figure 4.5(b), where  $P_2$  is perpendicular to the thread surface and  $F_2$  is parallel to the thread surface. Due to the change in the geometrical orientation of the thread the direction of  $P_2$  acts downward that is opposite in comparison with the RHT pin tool. The plasticized material in the neighborhood of the thread moves downward and simultaneously from the RS to the AS owing to the clockwise rotation in a direction of  $R_2$  and thus deposits at the trailing side of the weld tool. Again, due to the constant volume process, the material transported to the bottom area is forced to follow an upward motion to fill out the potential cavity underneath the rotating shoulder. In the case of LHT pin tool the plasticized material moving downward has a direct contact with the threaded pin surface that enhances proper joining at the bottom of the welded joint.

### **4.3 Microstructure of the Double Sided Arc Welded Joint**

The typical macroscopic and microscopic structures of DSAWed Mg alloys are shown in Figure 4.6. Figure 4.6(a) and (b) shows the top weld bead surface and a cross-section of the DSAWed joint, respectively. It is seen that the top weld bead quality appeared excellent with complete cleaning of the oxide. The bottom weld bead surface was similar to the top. As shown in Figure 4.6(b), there was a slight sagging of the weld pool due to the effects of gravity on the molten pool during welding. Figure 4.6(c) shows an equiaxed microstructure of the HAZ in the DSAWed sample that was completely recrystallized. The grain size in the HAZ of DSAWed sample (Figure 4.6(c)) was larger than that in the HAZ of the FSWed sample (Figure 4.2(c)). This was attributed to the higher temperature

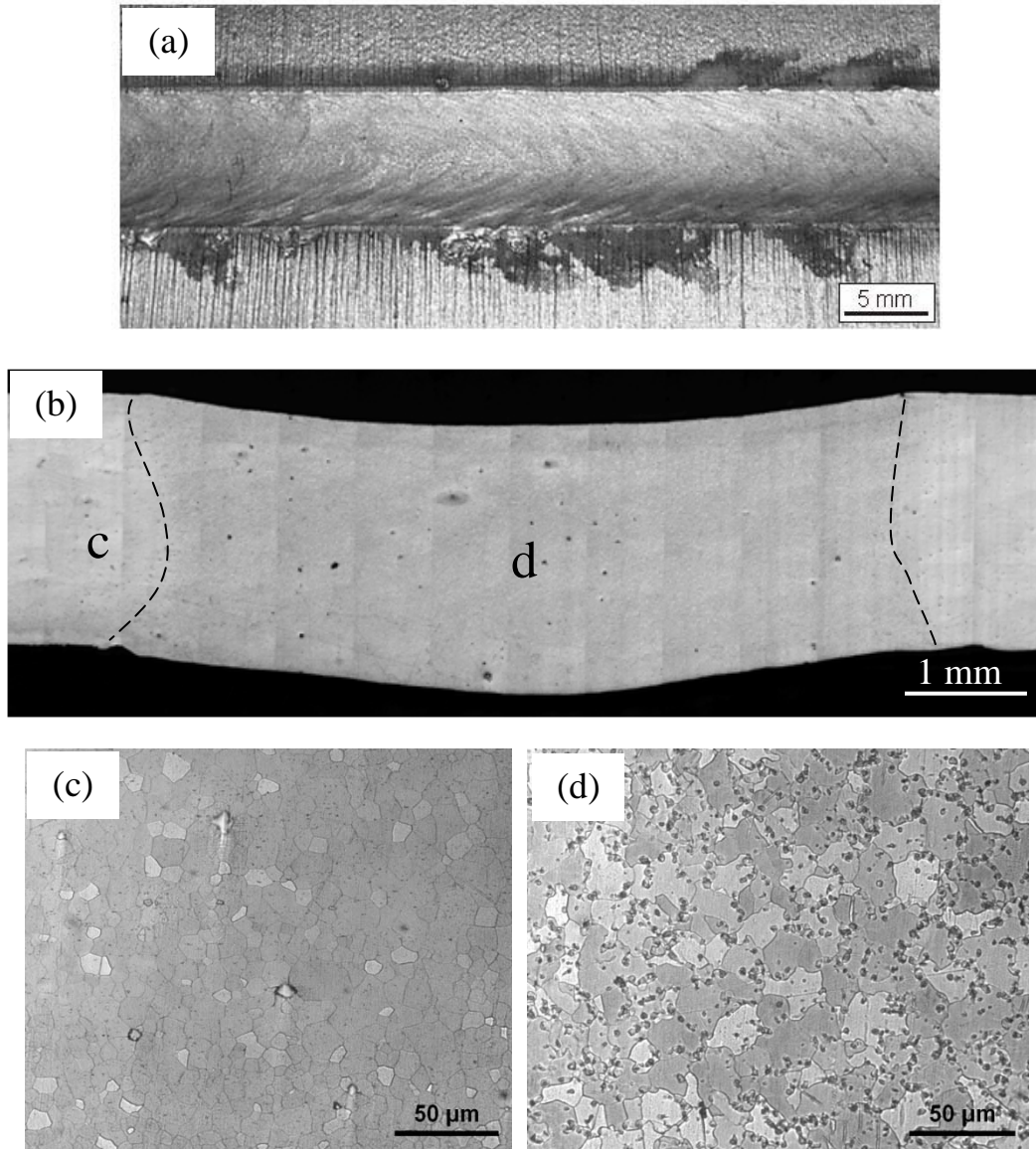


Figure 4.6: Typical macroscopic and microscopic structures of a double sided arc welded (DSAWed) AZ31 alloy. (a) Top weld bead surface, (b) cross-section of the welded joint, (c) heat-affected zone (HAZ), and (d) fusion zone (FZ).

experienced in the HAZ of the DSAWed sample. The fusion boundary had a slight hour glass shape (Figure 4.6(b)) and the grain size in the FZ, Figure 4.6(d), became larger with  $\beta$  ( $Mg_{17}Al_{12}$ ) phase particles arising from a divorced eutectic that formed in the interdendritic and intergranular regions of the solidification microstructure in the FZ.

#### 4.4 EDS Analysis

EDS analysis indicated that some Mn-Al containing particles/inclusions were present in the BM, as shown in Figure 4.7. Similar results were observed by Lin and Chen [69]. Figure 4.8 shows a typical particle in the HAZ. Line scan with EDS analysis signified that this particle was similar to the Mn-Al containing particle observed in the base metal (Figure 4.1), in spite of the remainder of the material experiencing a transition of microstructure in the HAZ (Figure 4.2(c) and 4.6(c)). Figure 4.9(a) revealed clearly a divorced eutectic structure in the FZ of the DSAWed sample, with both  $\beta$  phase particle on the left-hand side and the unmelted Mn-Al containing particle on the right-hand side along the grain boundary, although both particles had the same white color on the image. The eutectic-like structure consisting of alternating eutectic  $\alpha$ -Mg and eutectic  $\beta$ -Mg<sub>17</sub>Al<sub>12</sub> along the grain boundary could be seen in Figure 4.9(b). The presence of the eutectic-like structure was due to the fast non-equilibrium cooling of the weld pool after welding, since no normal eutectic structure in the form of alternating layers of  $\alpha$  and  $\beta$  would be possible in the AZ31 Mg alloy containing only 3 wt% Al. As seen in Figure 4.6(d) and Figure 4.9(a,b) there were also many  $\beta$ -Mg<sub>17</sub>Al<sub>12</sub> particles within the grains. Liu *et al.* [70] studied laser/arc hybrid welding behavior on Mg alloy and reported that many “spot” precipitates formed within the Mg grain were likely to be the  $\beta$ -Mg<sub>17</sub>Al<sub>12</sub> phase. Liu *et al.* [71] also observed Mg-Al intermetallic brittle phase in the FZ of TIG welded Mg/Al dissimilar joints. Ben-Hamu *et al.* [72] studied GTA welded AZ31B Mg alloy and reported that the FZ microstructure consisted of a cored  $\alpha$ -Mg matrix and a divorced eutectic in the interdendritic regions which were originally Mg<sub>17</sub>Al<sub>12</sub> that

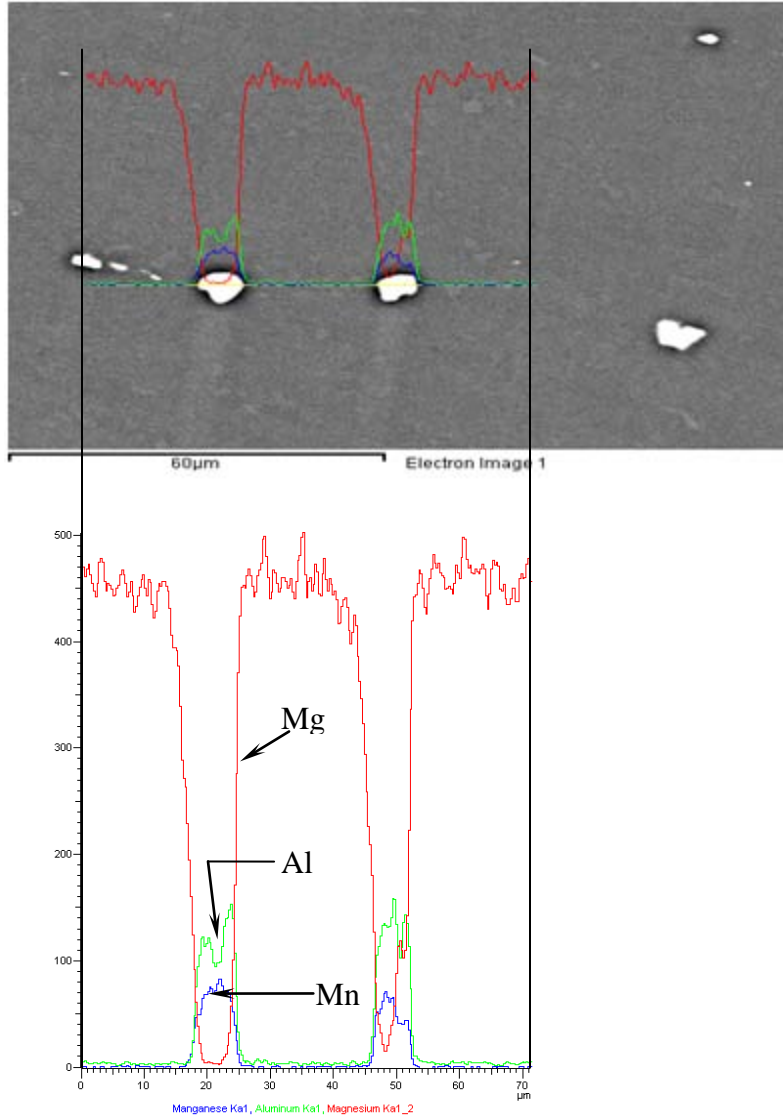


Figure 4.7: EDS line scan showing the compositional variation across the particles in base metal (BM).

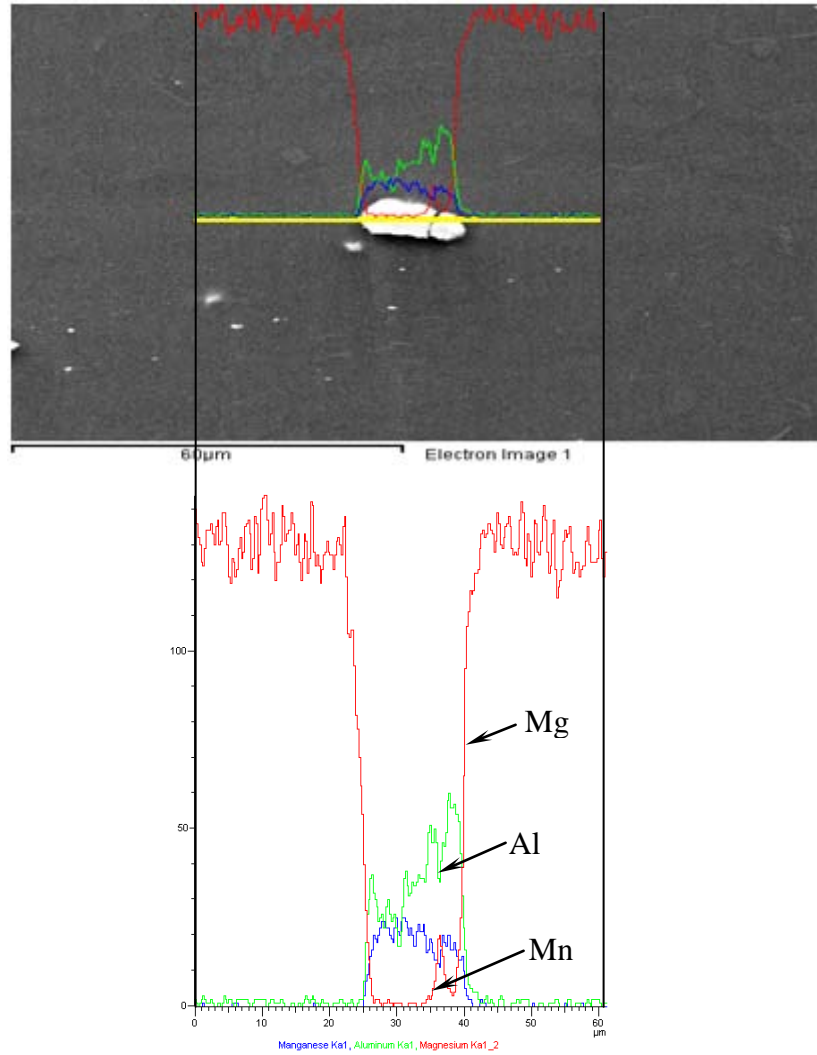


Figure 4.8: EDS line scan showing the compositional variation across the particle in heat-affected zone (HAZ).

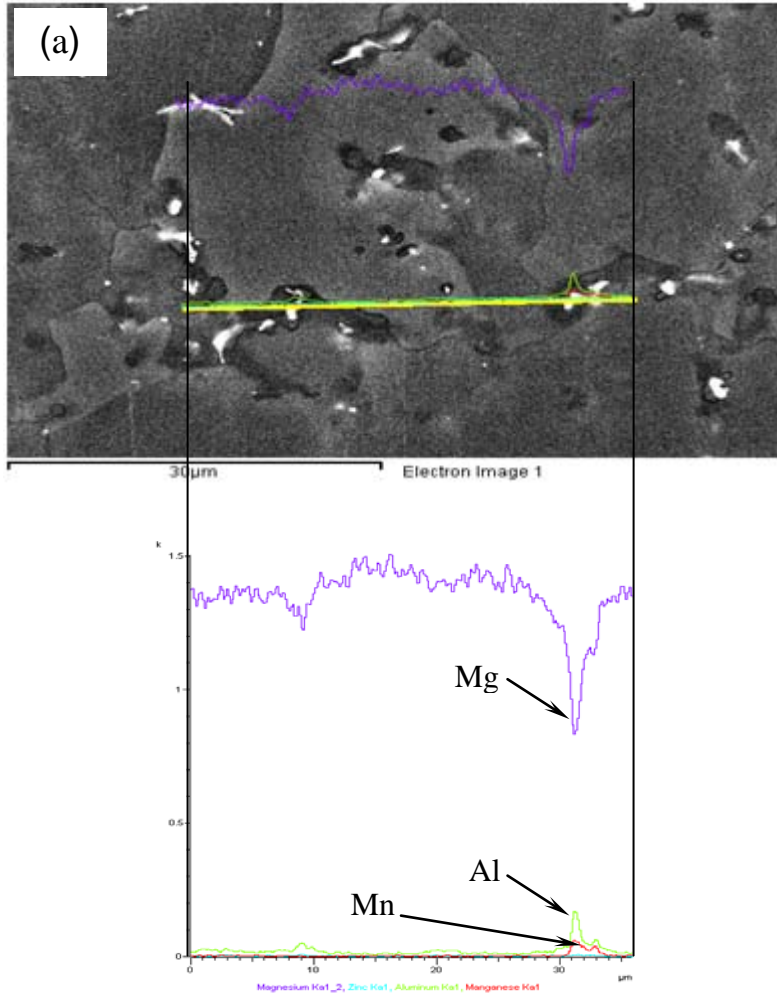


Figure 4.9(a): EDS line scan showing the compositional variation across the particles in fusion zone (FZ) of DSAWed joint.

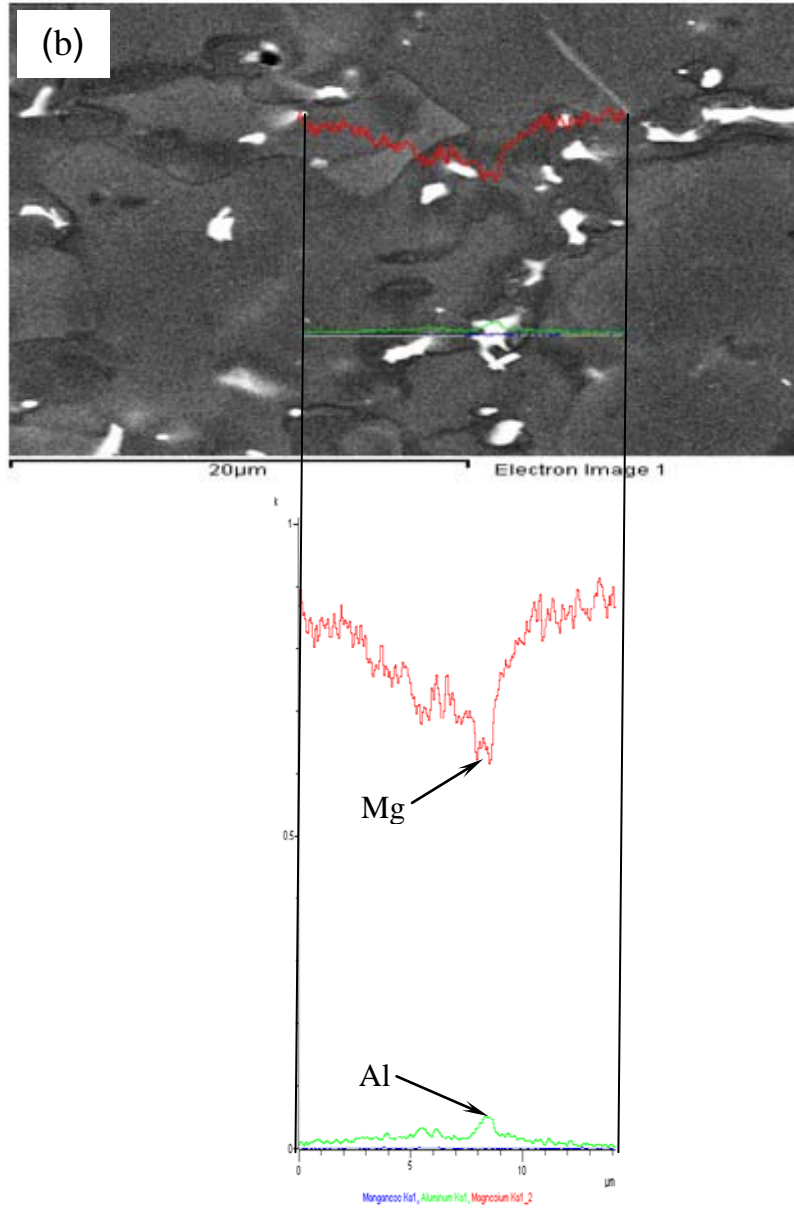


Figure 4.9(b): EDS line scan showing the compositional variation across the particles in fusion zone (FZ) of DSAWed joint at higher magnification.

subsequently transformed to  $\tau$  phase ( $Mg_{32}(Al,Zn)_{49}$ ) intermetallics. Electron beam welding and gas tungsten arc welding had been employed to weld AZ91 and AZ31B Mg

alloys, respectively, by Su *et al.* [73] and Padmanaban *et al.* [74], and they observed fine equiaxed grains with intergranular  $\beta$ -Mg<sub>17</sub>Al<sub>12</sub> precipitates as well.

## 4.5 Micro-hardness

Typical hardness profiles across the DSAWed and FSWed AZ31B Mg alloy are shown in Figure 4.10. It is seen that in both of the welded joints the hardness value decreased gradually from about HV 72-73 in the half-hardened H24 temper BM to approximately HV 50 at the center of the FZ of the welded joints.

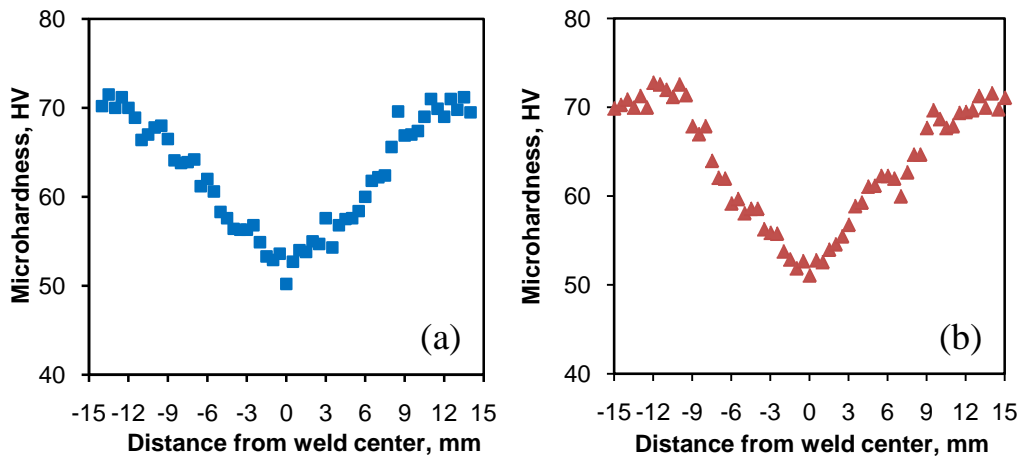


Figure 4.10: Microhardness profile across a) DSAWed sample, and b) FSWed sample.

In DSAWed joints, this is due to the formation of non-equilibrium cast structures in the FZ (Figure 4.6(d)), in conjunction with a larger grain size in the FZ in comparison with that in the HAZ (Figure 4.6(c)) and in the BM (Figure 4.1). Furthermore, the grain shape had a significant change from the deformed and elongated (or pancake-shaped) grains in the half-hardened H24 condition (Figure 4.1) to the fully annealed or recrystallized equiaxed grains in the HAZ (Figure 4.6(c)). All of these factors led to the hardness

change shown in Figure 4.10. Similar results were observed for the FSWed joints, where the lowest hardness occurred at the center of stir zone as well.

#### 4.6 Tensile Strength and Ductility

Figure 4.11 shows typical engineering stress versus engineering strain curves of the BM, FSWed and DSAWed AZ31 Mg alloy sheets tested at a strain rate of  $1 \times 10^{-5} \text{ s}^{-1}$ .

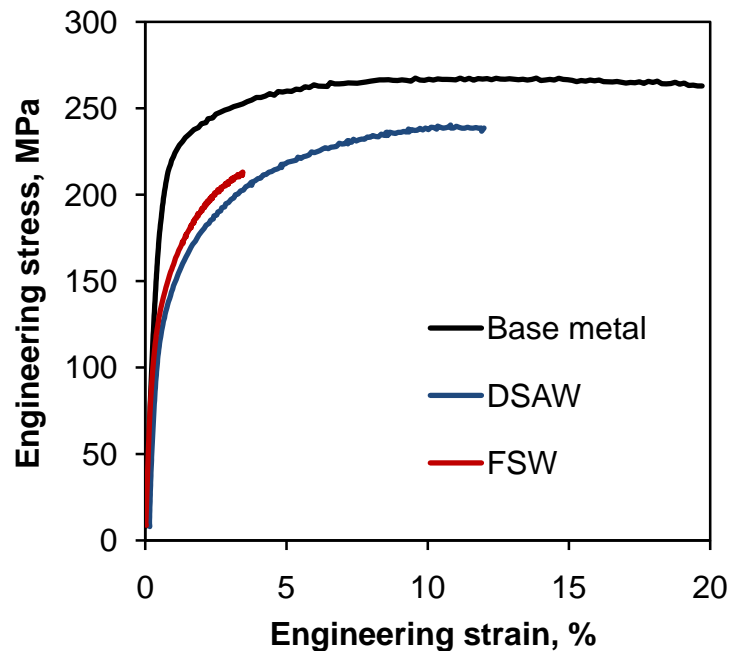


Figure 4.11: Typical engineering stress versus engineering strain curves of the AZ31B base alloy, FSWed and DSAWed samples tested at a strain rate of  $1 \times 10^{-5} \text{ s}^{-1}$ .

In this case, FSW was welded by RHTed weld tool. It is seen that after welding, both the strength and elongation were reduced. While the FSWed sample had higher yield strength (YS), the DSAWed sample had a higher ultimate tensile strength (UTS) and elongation. A joint efficiency of about 83% was achieved for the DSAWed joints, but it was only

about 72% for the FSWed joint. Figure 4.12 presents the effect of strain rate on the tensile properties.

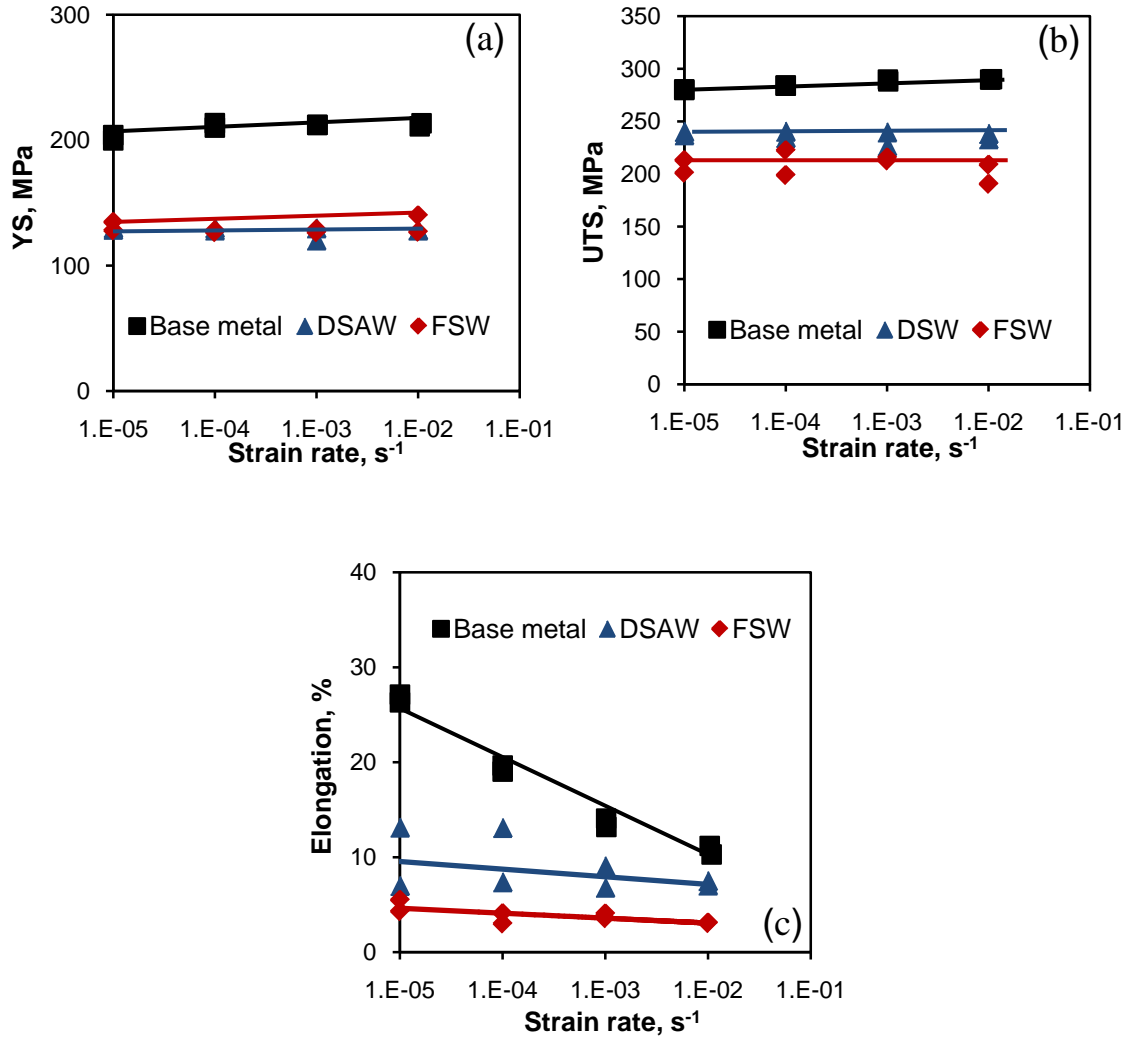


Figure 4.12: Effect of strain rate on (a) yield strength (YS), (b) ultimate tensile strength (UTS), and (c) ductility of the BM, FSWed and DSAWed samples.

It was clear that the YS and UTS increased and ductility (%El) decreased with increasing strain rate for the BM, but the effect of strain rate on the YS, UTS and %El became smaller after both types of welding. Similar effect of strain rate on the YS and UTS was

also reported in Mg-9Li-1Y [75], AM30 [76], cryo-rolled Cu [77] and AZ31B alloys [45,78,79]. Both the UTS and %El of the DSAWed joints lay in-between those of the BM and the FSWed joints. The reason behind this was the presence of a significant welding defect observed near the bottom surface of FSWed samples using a RHTed pin tool, as shown in Figure 4.4. Similar defects were also observed by Cao and Jahazi [15] who noted that the upward movement of the material in the SZ may cause the formation of subsurface porosity or even root notches near the bottom surface of the work-piece when the right-hand pin was used. It is clear that such defects at the bottom surface in the FSWed joints would lead to a strong notch effect or stress concentration and have a significant influence on the mechanical properties, causing premature failure as shown in Figure 4.11. As a consequence, both the UTS and ductility of the FSWed samples were reduced significantly (Figure 4.12(b) and (c)), in spite of the slightly higher YS (Figure 4.12(a)), in comparison with those of DSAWed joints.

#### **4.6.1 Effect of Weld Parameter**

Figure 4.13(a) shows typical engineering stress versus engineering strain curves of the BM and FSWed AZ31B Mg alloy joints at different welding speeds and rotational rates tested at a strain rate of  $1 \times 10^{-4} \text{ s}^{-1}$  at room temperature. In this case all FSWed joints were welded by LHTed weld tool. The middle portion in the region of YS is magnified in Figure 4.13(b) to better distinguish the stress-strain curves of FSWed joints. It is seen that after welding both the strength and elongation reduced. The ultimate tensile strength (UTS) of the BM in the rolling direction was obtained to be 286 MPa, which was about 6.3% higher than the minimum UTS of 269 MPa specified in ASTM B90-07 for the

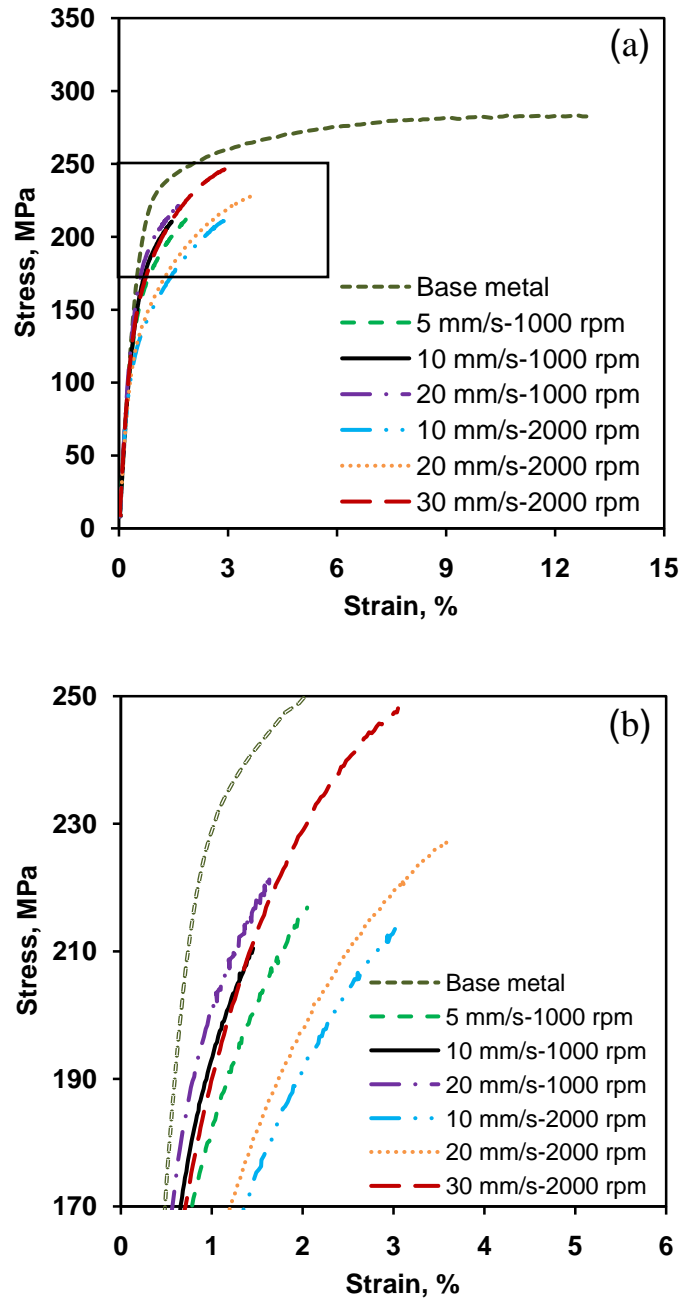


Figure 4.13: (a) Typical engineering stress-strain curves of the AZ31B-H24 base alloy and FSWed samples tested at a strain rate of  $1 \times 10^{-4} \text{ s}^{-1}$ , (b) a magnified view of the region boxed in (a).

present thin sheet in H24 condition. Joint efficiency of the FSWed joints varied approximately from 74% to 83%. The elongations were relatively low compared to the BM, ranging from approximately 2.3 to 4.4%. Figure 4.14 presents the effect of strain rate on the tensile properties of the BM and FSWed joints at varying welding speeds and rotational rates. Firstly, as expected, both the strength and ductility decreased after FSW. A slight increase of YS and UTS with increasing strain rate in the BM was observed

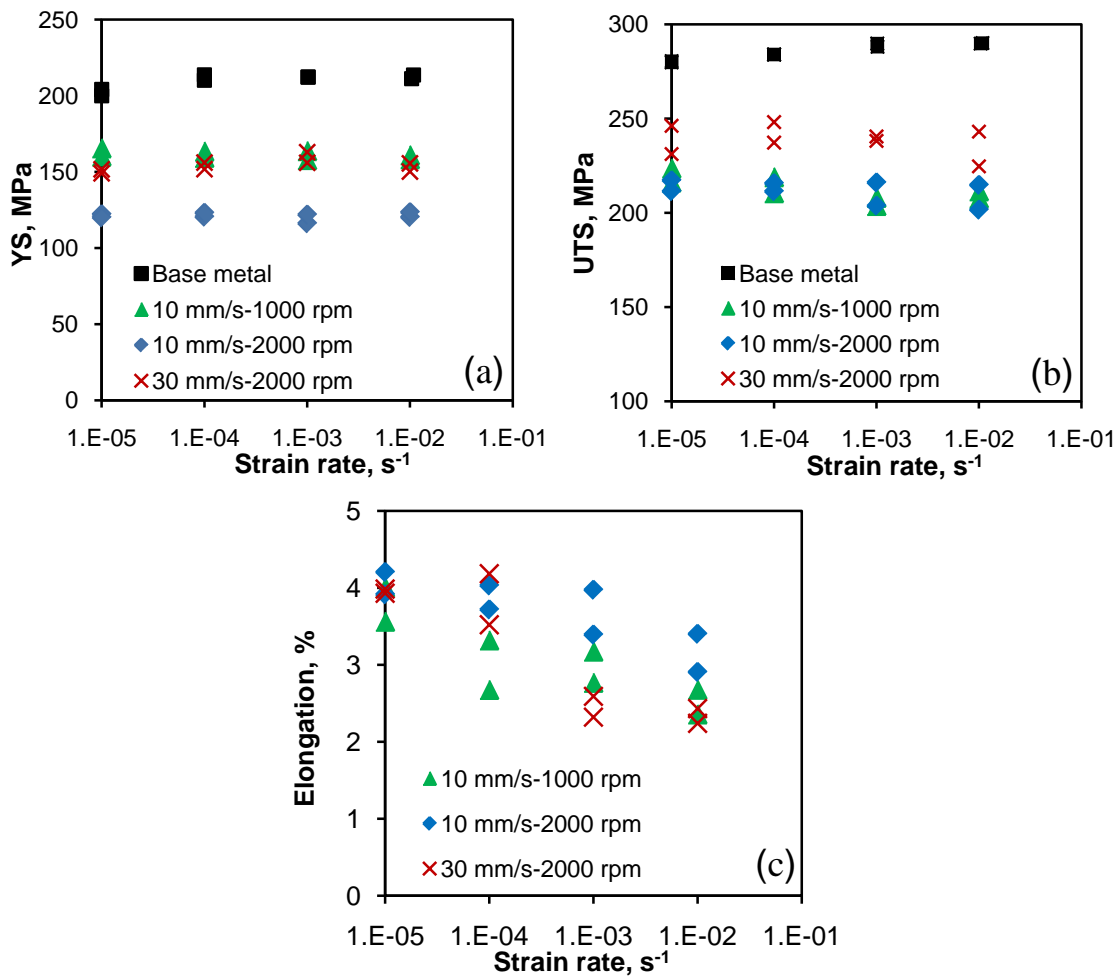


Figure 4.14: Effect of strain rate on (a) yield strength (YS), (b) ultimate tensile strength (UTS), and (c) ductility of the FSWed samples at different welding speeds and rotational rates.

while ductility decreased drastically (Figures 4.12(c) and 4.14(c)). However, for the FSWed samples the strain rate dependence became much weaker. The strain rate sensitivity of the BM will be discussed later.

Secondly, the effect of the welding speed and rotational rate on the YS and UTS of the FSWed joints could be seen in Figure 4.14. A significant increase in the YS was observed at the higher welding speed of 30 mm/s than at 10 mm/s at a constant rotational rate of 2000 rpm (Figure 4.14(a)). Similarly, the YS increased with decreasing rotational rate from 2000 rpm to 1000 rpm at a constant welding speed of 10 mm/s. The reason behind this could be explained by the heat energy generated during FSW. The total energy generated by the rotating pin tool to the workpiece ( $E_{total}$ ), consisted of the energy due to the plastic deformation of the material ( $E_{plastic}$ ) and the energy created by friction between the tool and workpieces ( $E_{friction}$ ) [80],

$$E_{total} = E_{friction} + E_{plastic}. \quad (4.1)$$

Then the total energy generated during FSW can be expressed as follows [18],

$$E_{total} = 2\mu F \left( \frac{1}{3} r_o + \frac{r_i^2}{r_o^2} h \right) \frac{\omega}{v_o} + s \sigma_\varepsilon \varepsilon_\varepsilon (2r_i h) \quad (4.2)$$

where  $\mu$  is the coefficient of friction,  $F$  is the compressive force,  $r_o$  is the radius of the shoulder,  $r_i$  is the radius of the pin,  $h$  is the height of the pin,  $\omega$  is the tool angular velocity in rpm (rev/min),  $v_o$  is the welding speed,  $s$  is a scale factor,  $\sigma_\varepsilon$  is the effective stress and  $\varepsilon_\varepsilon$  is the effective strain. Based on Equation 4.2 the heat input is inversely related to the welding speed and directly proportional to the tool rotational rate while keeping other parameters constant. That is, during FSW low heat was generated at a high welding speed and/or low rotational rate, leading to a smaller grain size of the FSWed

joints (Figure 4.2). It is well known that the YS at room temperature depends on the grain size according to the following Hall-Petch relationship,

$$\sigma_{0.2} = \sigma_o + kd^{-1/2}, \quad (4.3)$$

where  $\sigma_{0.2}$  is the YS of the material,  $d$  is the grain size,  $\sigma_o$  is the “friction stress” representing the overall resistance of the crystal lattice to dislocation movement (or the YS related to a material with infinitely large grain size which is similar to that of single crystal), and  $k$  is a constant called “locking parameter” representing the relative hardening contribution of grain boundaries as obstacles to slip across the grain boundaries [81,82]. Figure 4.15 shows the obtained YS as a function of the grain size of the FSWed joints made with different welding parameters. It is seen that the YS followed the Hall-Petch relationship nicely. This suggested that the grain boundaries were the main obstacle to the slip of dislocations and the material with a smaller grain size had a higher strength as it would impose more restrictions to the dislocation movement. As shown in Figure 4.14(b) the UTS increased with increasing welding speed as well, which was observed by several researchers [5-7,15]. But the UTS decreased beyond a certain welding speed due to the formation of the welding defects such as kissing bond. Due to the microscopic roughness or asperities or the oxides with some absorbed air, effective metallic bonding might not be well established in the solid state during FSW, leading to the formation of kissing bond defects at high welding speeds (i.e., with low heat input) [15].

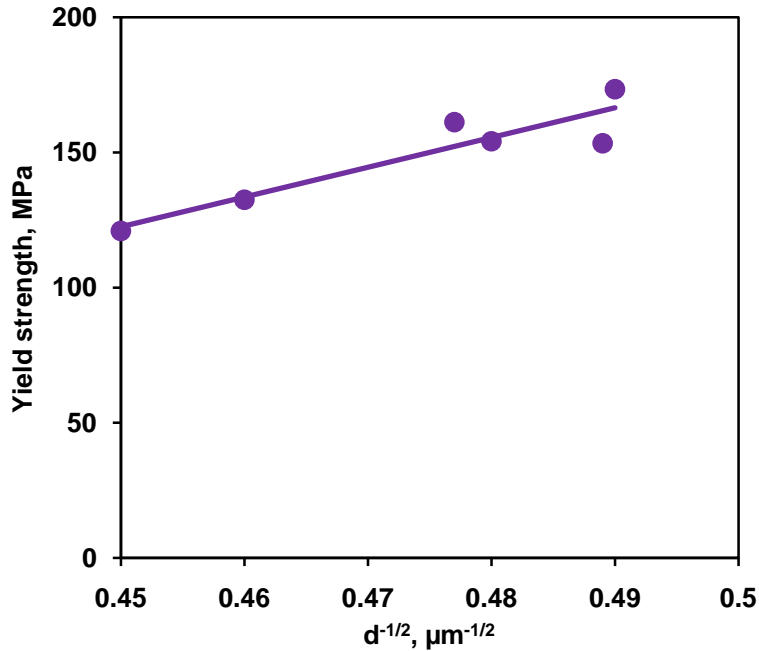


Figure 4.15: Yield strength versus grain size in the AZ31B alloy after FSW at different welding speeds and rotational rates.

It should be noted that, the kissing bond was extremely difficult to detect with any non-destructive testing method due to its sub-millimeter size [83]. The overall reduction in the ductility after FSW (Figure 4.11 or Figure 4.14(c)) would be due to the presence of a certain amount of kissing bond defects and/or lack-of-bonding defects occurring near the bottom surface for the FSWed joints made with a RHT pin tool turning clockwise. The percent elongation increased either with increasing rotational rate or with decreasing welding speed, as shown in Figure 4.14(c), which was also in good agreement with the results reported in [84].

The change of the strength with the welding speed and rotational rate has also been observed by several other researchers [5-8,85]. The combined role of both the welding

speed and rotational rate could be better represented by the weld pitch ( $v/\omega$ ) [46]. The strength of the FSWed joints as a function of the weld pitch is plotted in Figure 4.16.

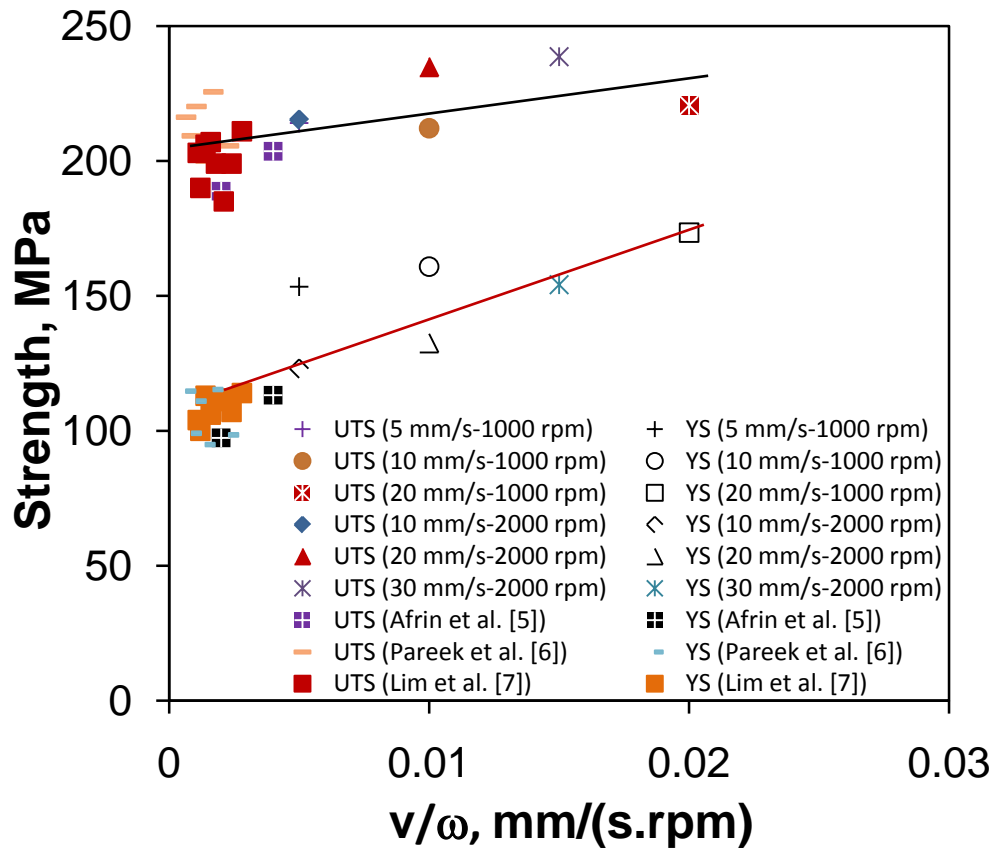


Figure 4.16: A comparison of the YS and UTS of the AZ31B FSWed joints, as a function of the weld pitch [the ratio of welding speed ( $v$ ) to rotational rate ( $\omega$ )], with those reported in the literature.

It is of interest to observe that with increasing weld pitch over a wide range both YS and UTS increased significantly in a linear form within the experimental scatter, especially for the YS. For the sake of comparison, the data reported in the literature [5-7] are also plotted in Figure 4.16. The strength of the FSWed magnesium joints made with smaller weld pitches lay basically in the left low end with a YS of about 110 MPa and a UTS of

about 200 MPa in the weld pitch range of 0.00065-0.004 mm/(s.rpm) [5-7], while in the present study a YS of as high as about 170 MPa has been achieved at a high weld pitch of 0.02 mm/(s.rpm) or 1.2 mm/rev in spite of only a modest increase in the UTS to about 230 MPa. Such a change could be understood from Equation 4.2. With increasing value of  $v/\omega$ , the total heat generation during FSW decreased, leading to the formation of smaller grain sizes, as shown in Figure 4.2. As a result, the strength of the FSWed joints increased with increasing  $v/\omega$  according to the Hall-Petch relationship (Figure 4.15 and Equation 4.3). The observed linear variation of the YS and UTS with the weld pitch  $v/\omega$  could be expressed as:

$$YS = \alpha_1 + \beta_1 \frac{v}{\omega}, \quad (4.4)$$

$$UTS = \alpha_2 + \beta_2 \frac{v}{\omega}, \quad (4.5)$$

where  $\alpha_1$ ,  $\beta_1$ ,  $\alpha_2$  and  $\beta_2$  are constants. In the present FSWed AZ31B-H24 Mg alloy, these parameters were determined to be  $\alpha_1 = 126$  MPa,  $\beta_1 = 2194$  (s.rpm.MPa)/mm,  $\alpha_2 = 214$  MPa,  $\beta_2 = 817$  (s.rpm.MPa)/mm. Clearly, the slope of  $\beta_1$  was much higher than  $\beta_2$ , indicating a stronger effect of the weld pitch on the YS than on the UTS. It should be noted that while the above linear relationships were seen to be valid in a fairly wide range of weld pitch values (Figure 4.16) in comparison with those reported in the literature, an upper limit or threshold value of  $v/\omega$  could be expected above which a large amount of kissing bond defects or other lack-of-bonding defects could occur, since the proper mechanical/metallurgical bonding might not be established due to the inadequate plasticization of the material caused by the insufficient heat energy input at too high weld

itches. Such an upper limit would also be anticipated to depend on the temperature-dependent flow characteristics of materials. Thus different materials would have different upper limit values of  $v/\omega$ . Further studies are needed to find the upper limits of the weld pitch for different materials.

#### 4.6.2 Effect of Thread

The effect of thread orientation (LHT and RHT) of the FSW pin tool on the tensile properties is shown in Figure 4.17 at a welding speed of 10 mm/s and rotational rate of 2000 rpm in the clockwise rotation.

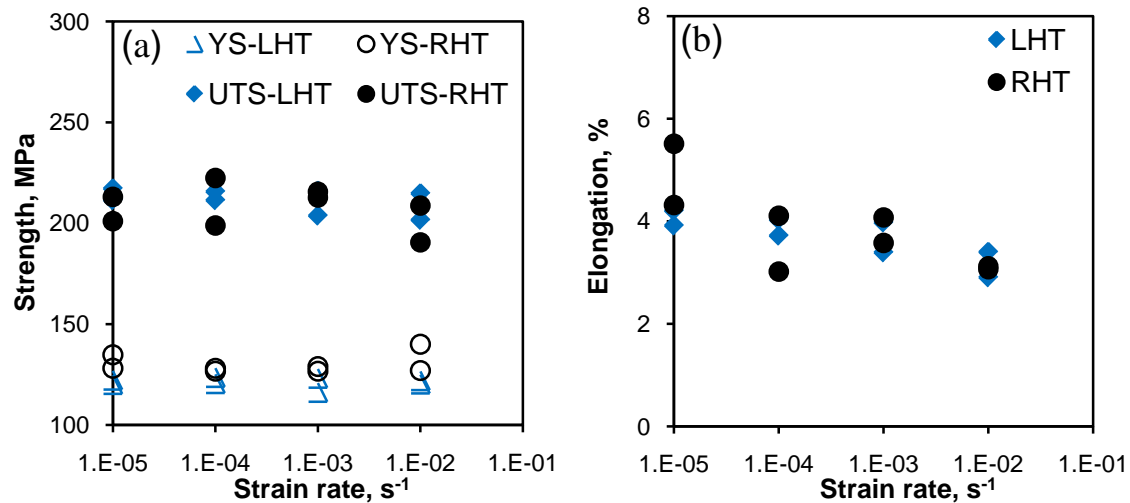


Figure 4.17: Effect of pin tool thread orientation on (a) YS and UTS, and (b) ductility of the AZ31B FSWed joints at a welding speed of 10 mm/s and rotational rate of 2000 rpm.

It is seen from Figure 4.17 that in spite of the presence of cavity or lack-of-bonding defects near the bottom surface (Figure 4.4), the UTS became slightly lower and the YS was slightly higher, while the ductility was equivalent for the FSWed joints made with

RHT pin tool, in comparison with the FSWed joints made with LHT pin tool. However, the tensile test data obtained for the FSWed joints made with RHT pin tool were more scattered (Figure 4.17) due to the presence of defects near the bottom surface (Figure 4.4).

### **4.6.3 Change of Failure Location of the FSWed Joint**

In this section, mainly the failure location of the FSWed joints is discussed. In the arc welded joints, failure occurred at the centre of the joints during tensile testing due to the presence of large grains along with brittle precipitates but in FSWed joints the failure of the FSWed sample was in the form of  $45^\circ$  shear fracture, which could be due to the significant change of texture with a high intensity of (0002) diffraction around the TMAZ during FSW, leading to a prone slip along the (0002) with an orientation of  $\sim 45^\circ$  at a low critical resolved shear stress [86]. The failure of all the FSWed joints was observe to occur in-between the SZ and TMAZ either on the AS or RS side, depending on the welding parameters and the thread of weld tool as well. It appeared that at a low welding speed of 10 mm/s all FSWed joints made with the LHT pin tool turning clockwise failed on the AS side, while a higher welding speed of 30 mm/s and RHT pin tool rotating clockwise promoted failure at the RS side, as summarized in Table 4-1. Seidel and Reynolds [46] also observed that at a high weld pitch the amount of plastic deformation of the material at the joint was reduced at the RS and stated that the vertical mixture of material at the RS was inversely proportional to the weld pitch. This inadequate plastic deformation enhanced the formation of oxide layer at the RS during FSW, as also reported by Afrin *et al.* [5] and Shinoda [87]. This oxide-rich region then significantly affected the tensile behavior of Mg alloy and thus failure occurred at the RS at high weld pitches during tensile tests.

Table 4-1 Failure locations of the FSWed specimens during tensile testing.

Welding parameter	Weld pitch mm/(s.rpm)	Thread of weld tool	Failure location	
			(AS)	(RS)
30 mm/s and 2000 rpm	0.015	LHT	0	8
10 mm/s and 2000 rpm	0.005	LHT	8	0
10 mm/s and 1000 rpm	0.010	LHT	8	0
10 mm/s and 2000 rpm	0.005	RHT	2	6

On the other hand, Park *et al.* [41] reported that for the FSWed AZ31 joints texture or preferred orientation was considered as a major factor for the failure during tensile tests and the joints failed along the plane with a higher Schmid factor. During the FSW the change of material flow direction by changing the thread orientation (from LHT to RHT) of the weld tool, as shown in Figure 4.5, was likely to contribute to the change of texture, leading to the failure of samples at the RS as well, even though the weld pitch was low. More studies are needed on this aspect.

#### 4.7 Strain Hardening Behavior

The hardening capacity of a material may be considered as a ratio of the ultimate tensile strength  $\sigma_{UTS}$ , to the yield strength  $\sigma_y$  [45,88]. Afrin *et al.* [45] re-defined a normalized parameter of hardening capacity,  $H_c$ , as follows,

$$H_c = \frac{\sigma_{UTS} - \sigma_y}{\sigma_y} = \frac{\sigma_{UTS}}{\sigma_y} - 1 \quad (4.6)$$

The obtained hardening capacity of the BM and the welded samples is listed in Table 4-2.

Table 4-2 Hardening capacity of the base alloy, FSWed and DSAWed samples tested at different strain rates.

Specimen	Average strain rate ( $s^{-1}$ )	Hardening capacity ( $H_c$ )
Base metal	$1 \times 10^{-2}$	0.37
	$1 \times 10^{-3}$	0.36
	$1 \times 10^{-4}$	0.36
	$1 \times 10^{-5}$	0.41
Friction stir welded sample	$1 \times 10^{-2}$	0.49
	$1 \times 10^{-3}$	0.67
	$1 \times 10^{-4}$	0.66
	$1 \times 10^{-5}$	0.57
Double sided arc welded sample	$1 \times 10^{-2}$	0.84
	$1 \times 10^{-3}$	0.86
	$1 \times 10^{-4}$	0.84
	$1 \times 10^{-5}$	0.84

For the convenience of readers only one FSWed sample at a welding speed of 10 mm/s and 2000 rpm rotational rate using right hand thread weld tool was taken into consideration to compare the hardening capacity with DSAWed sample. It is seen that the hardening capacity was enhanced after FSW, similar to the results reported by Afrin et al [45]. The hardening capacity in the DSAWed samples was even higher than that in the FSWed samples. There was little effect of the strain rate on the hardening capacity. The hardening capacity of a material is related to its YS, which is further associated with the grain size according to the Hall-Petch relationship [82,89,90]. An increase in the grain size would decrease the YS and increase the hardening capacity. A decrease in the grain size reduced the difference of the flow resistance between the grain boundary and interior, which in turn reduces the hardening capacity [88]. Since the grain size of the DSAWed samples was larger than that of FSWed sample, as shown in Figure 4.2(e) and 4.6(d), respectively, the higher value of hardening capacity in the DSAWed samples would be

anticipated. To understand strain hardening behavior it is better to examine the strain hardening exponents of different materials. The strain hardening exponent is a measure of the ability of a metal to strain harden; the larger its magnitude, the greater the strain hardening for a given amount of plastic strain [89]. Several researchers have proposed different equations to evaluate the strain hardening exponent. Hollomon [91] gave the following expression,

$$\sigma = K\varepsilon^n, \quad (4.7)$$

where  $n$  is the strain (or work) hardening exponent,  $K$  is the strength coefficient,  $\sigma$  is the true stress and  $\varepsilon$  is the true strain [90-93]. To better quantify the strain hardening response, Chen and Lu [94] fitted their tensile curves using the Ludwik equation [93-95],

$$\sigma = \sigma_y + K_1\varepsilon^{n_1}, \quad (4.8)$$

where  $n_1$  is the strain hardening exponent and  $K_1$  is the strength coefficient which represents the increment in strength due to strain hardening at  $\varepsilon = 1$ . Afrin *et al.* [45] proposed the following equation using net flow stress and net plastic strain of materials after yielding,

$$\sigma = \sigma_y + K^*(\varepsilon - \varepsilon_y)^{n^*}, \quad (4.9)$$

where  $n^*$ ,  $\sigma$ ,  $\varepsilon$ ,  $\sigma_y$  and  $\varepsilon_y$  are the strain hardening exponent, true stress, true strain, yield strength and yield strain of a material, respectively.  $K^*$  is the strength coefficient which reflects the increment in strength due to strain hardening corresponding to  $(\varepsilon - \varepsilon_y) = 1$ . The above three equations could be better illustrated in Figure 4.18. Equation 4.7 has the origin positioned at O (including the elastic deformation stage where the Hooke's law holds true), although only the data in the uniform deformation stage between the YS and

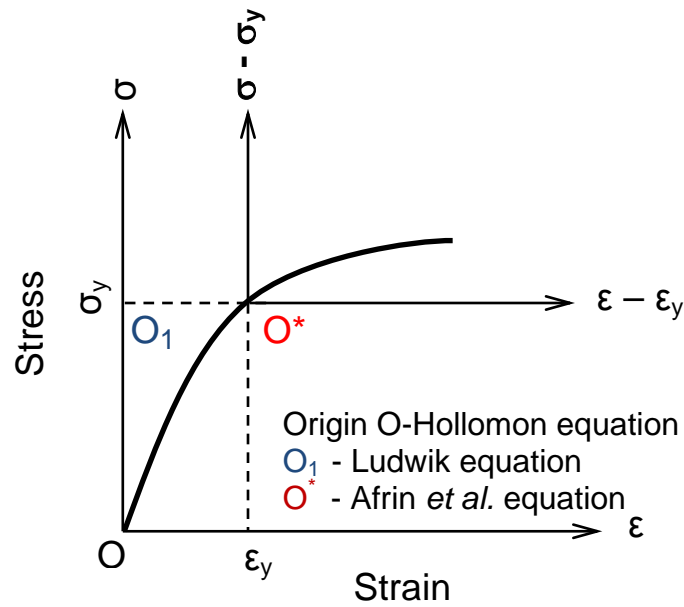


Figure 4.18: Schematic illustration of a true stress versus true strain curve.

UTS are used. Equation 4.8 corresponds to a shift of the origin from  $O$  to  $O_1$  in Figure 4.18 where the yield stress is excluded, while Equation 4.9 proposed recently by Afrin *et al.* [45] represents a further shift of the origin from  $O_1$  to  $O^*$ . It implies that both the yield stress and yield strain are precluded.

Figure 4.19 presents the evaluated strain hardening exponents ( $n, n_1, n^*$ ) as a function of strain rate for the base metal, FSWed and DSAWed samples. Almost no effect of strain rate on the strain hardening exponents was seen in the base metal. But for the DSAWed and FSWed samples, the strain hardening exponents increased with increasing strain rate. The strain hardening exponents evaluated according to all the above three equations were obviously higher after welding, and the DSAW resulted in somewhat higher strain hardening exponents than the FSW, as shown in Figure 4.19.

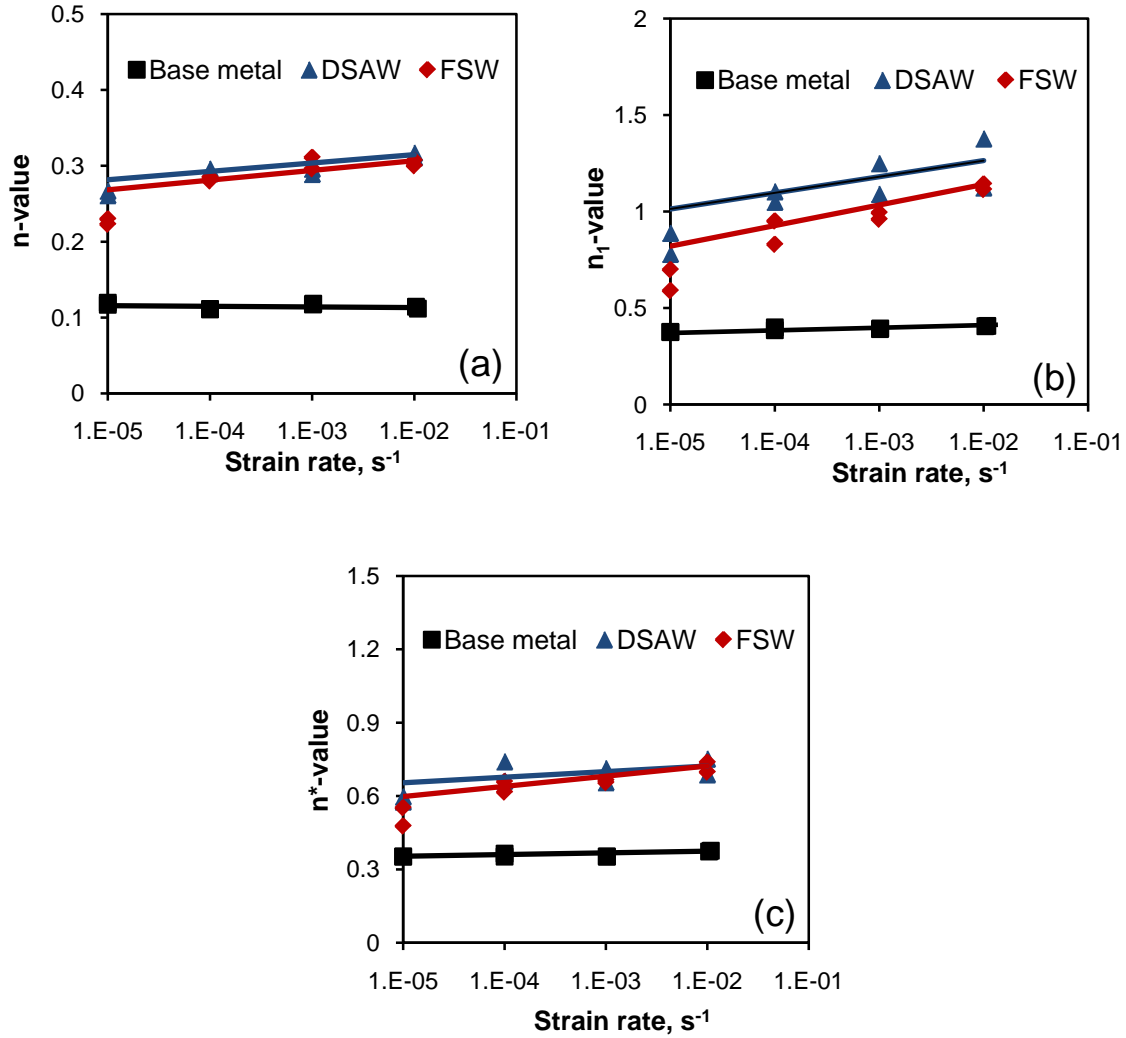


Figure 4.19: Effect of strain rate in the BM, FSWed and DSAWed samples on (a) n-value, (b) n<sub>1</sub>-value and (c) n\* -value.

It is also seen that the n values were the smallest and n<sub>1</sub> values were the highest with n\* lying in-between the two. One of the most important contributions to the strain hardening is related to the formation and multiplication of dislocations. In the plastic deformation stage, the net flow stress due to dislocation density could be expressed as [96,97],

$$\sigma - \sigma_y \propto \sqrt{\rho}, \quad (4.10)$$

where  $\rho$  is the dislocation density. The net flow stress necessary to continue deformation of a material is proportional to the square root of the dislocation density. The dislocation density in a metal increases with deformation or cold work due to dislocation multiplication or the formation of new dislocations which decreases the spacing among dislocations and their interactions become repulsive. The net result would be that the motion of a dislocation is impeded by other dislocations. As the dislocation density increases, the resistance to dislocation motion by other dislocations becomes more pronounced. Thus, a higher stress is necessary to deform a metal [89]. Figure 4.20 shows a typical Kocks-Mecking plot of strain hardening rate ( $\theta = d\sigma/d\varepsilon$ ) vs. net flow stress ( $\sigma - \sigma_y$ ) at different strain rates from  $1 \times 10^{-2} \text{ s}^{-1}$  to  $1 \times 10^{-4} \text{ s}^{-1}$  for the BM.

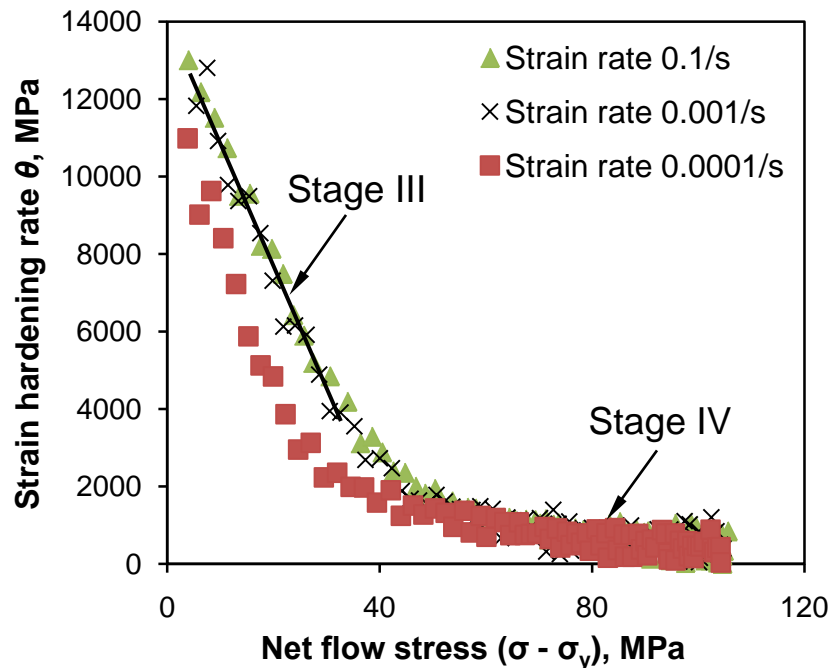


Figure 4.20: Strain hardening rate ( $\theta$ ) versus net flow stress ( $\sigma - \sigma_y$ ) of the BM tested at different strain rates.

It is seen that there was no stage I hardening (or ‘easy glide’) which depends strongly on the orientation of the crystal and stage II linear hardening where the strain hardening rate should be constant. Srinivasan and Stoebe [98] reported that the presence of stage II strain hardening could be due to the interactions of the dislocations in the primary slip system with those in an intersecting slip system. Stage III hardening is characterized by a hardening rate that decreases monotonically with increasing flow stress leading to the much repeated term “parabolic hardening” on the stress strain curve [99]. This stage is very sensitive to the temperature and rate of deformation [96]. In this present study test temperature remained constant but strain rates were changed. As seen from Figure 4.20 stage III was somewhat strain rate sensitive, i.e., the strain hardening rate increased with increasing strain rate. Similar result was observed by Lin and Chen [78] in AZ31B extruded Mg alloy as well. This could be explained on the basis of the following equation [78,96],

$$\theta = \theta_0 - \frac{R_d \sigma}{\dot{\epsilon}^{1/q}}, \quad (4.11)$$

where  $\theta$  is the strain-hardening rate in stage III,  $\theta_0$  is a constant,  $q$  is an experimental stress exponent varying with temperatures and is rather large namely about  $q=8$  at higher and  $q=35$  at lower temperatures and  $R_d$  is also a temperature dependent parameter. In the present experiments  $R_d$  and  $q$  were constant as temperature remained constant. It is evident from Equation 4.11 that the strain hardening rate increased with increasing strain rate at a given stress.

As stage III approached a saturation level, hardening stage IV appeared. Due to the low hardening level of stage IV, it is difficult to track the hardening mechanisms because they

must compete with geometrical and structural instabilities including damage [96]. However, Pantleon [100] reported that stage III hardening was extended to stage IV by incorporation of excess dislocations related to the disorientations. He further stated that in stage IV the work hardening rate often remains constant. It is seen from Figure 4.20 that stage IV in the BM remained almost constant with a low strain hardening rate.

Figure 4.21 shows a typical Kocks-Mecking plot of strain hardening rate vs. net flow stress in the base metal, FSWed and DSAWed samples tested at a strain rate of  $1 \times 10^{-2} \text{ s}^{-1}$ .

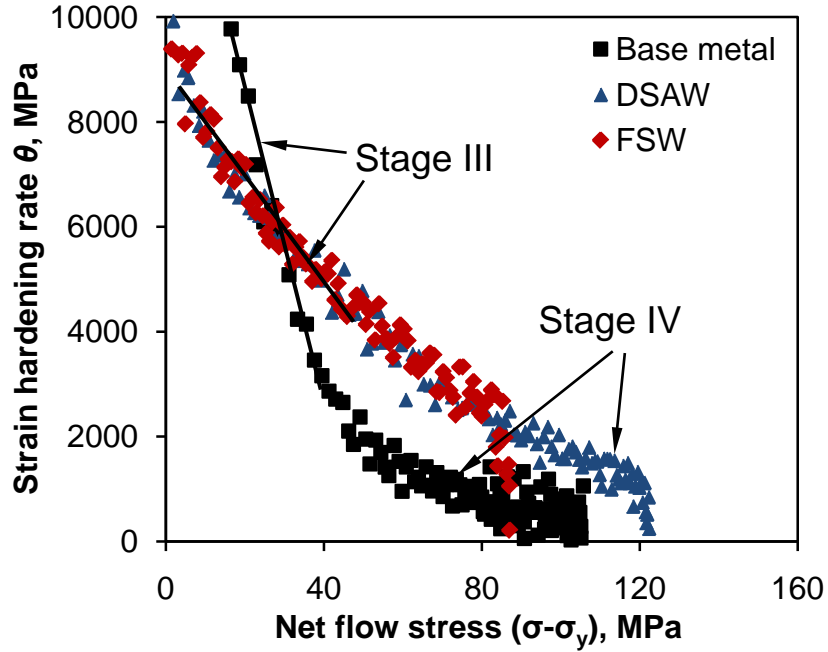


Figure 4.21: Strain hardening rate ( $\theta$ ) versus net flow stress ( $\sigma - \sigma_y$ ) of the BM, FSWed and DSAWed samples tested at a strain rate of  $1 \times 10^{-2} \text{ s}^{-1}$ .

At lower strains or net flow stress levels after yielding the strain hardening rate of the BM was higher than that of the welded joints. At higher strains or net flow stress levels it was

reversed. The strain hardening could be understood on the basis of the grain size strengthening and dislocation strain hardening [97,101],

$$\sigma = \sigma_0 + \sigma_{HP} + \sigma_d, \quad (4.12)$$

where  $\sigma_0$  is the frictional contribution,  $\sigma_{HP} = kd^{1/2}$  is the Hall-Petch contribution and  $\sigma_d = M\alpha Gb\rho^{1/2}$  is the Taylor dislocation contribution (where G is the shear modulus, b is the Burgers vector, M is the Taylor factor,  $\alpha$  is constant and  $\rho$  is the dislocation density).

Sinclair *et al.* [102] and Kovacs *et al.* [103] reported that at lower strains the grain size had a strong contribution to the strain hardening and the influence of the grain size on the strain hardening vanished at higher strains due to dislocation screening and dynamic recovery effects at grain boundaries. Since the base metal had a smaller grain size coupled with its deformed grain structure, the Hall-Petch contribution ( $\sigma_{HP}$ ) would be stronger at lower strains, leading to a higher strain hardening rate in comparison with the welded joints. On the other hand, at higher strains or later stage of deformation strain hardening was higher in the welded joints. This could be due to the larger grain size and the presence of  $\beta$  particles in the fusion zone of the DSAWed samples. It was stated that the presence of precipitates increased the dislocation density [104] and larger grain size provided more space to accommodate dislocations [45]. As the grain size of the DSAWed samples was larger, a strong strain hardening rate was observed after DSAW in comparison with the FSW and the BM (Figure 4.21). This is also in agreement with other observations where the hardening rate decreasing with decreasing grain sizes in AZ31 alloy was presented [97]. However, due to the presence of weld defects at the bottom

surface, the FSWed samples failed prematurely, thus the net flow stress up to failure in the FSWed sample was the lowest (Figure 4.21).

### 4.7.1 Effect of Welding Parameter and Thread

Figure 4.22 shows the effect of weld parameter on strain hardening exponent while Figure 4.23 shows the effect of pin tool thread orientation on the strain hardening exponent of the FSWed samples. The strain hardening exponent of the FSWed joints at different welding speeds and rotational rates increased slightly with increasing strain and increased as the welding speed decreased from 30 mm/s to 10 mm/s while the rotational rate was constant at 2000 rpm.

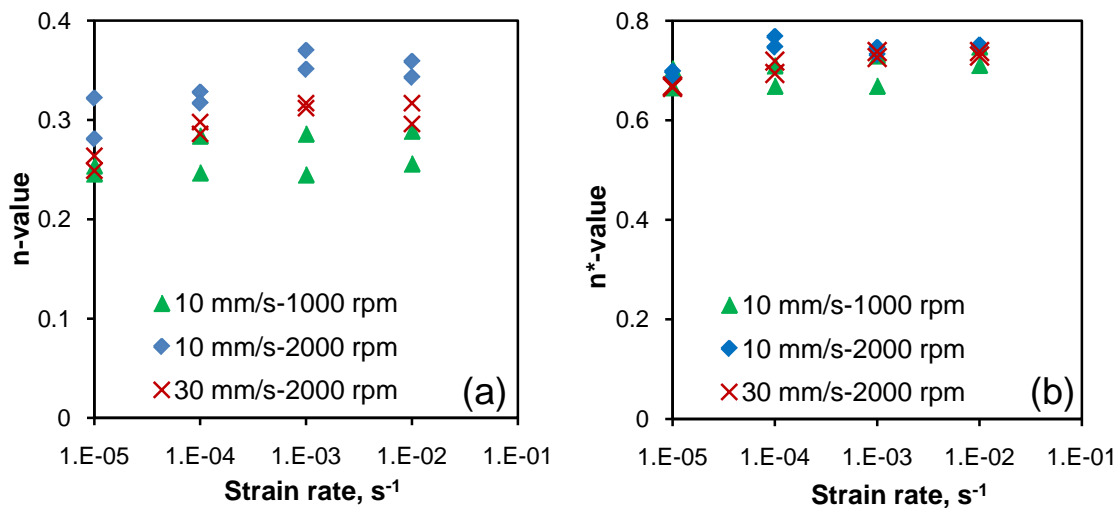


Figure 4.22: Effect of weld parameter on (a)  $n$ -value and (b)  $n^*$ -value in the AZ31B FSWed samples at different welding speeds and rotational rates.

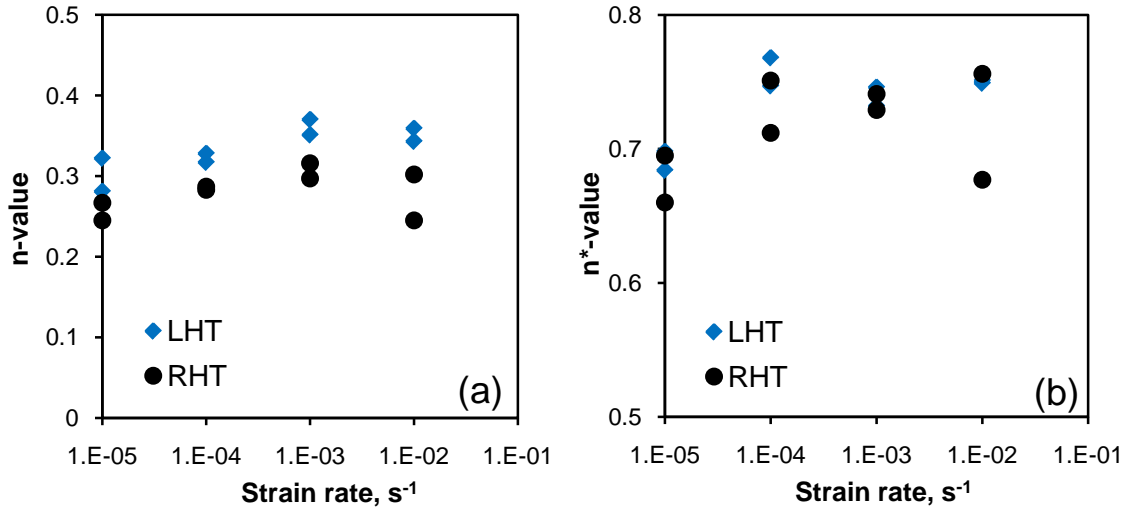


Figure 4.23: Effect of pin tool thread orientation on (a)  $n$ -value and (b)  $n^*$ -value in the AZ31B FSWed samples at a welding speed of 10 mm/s and rotational rate of 2000 rpm.

On the other hand, it increased with increasing rotational rates from 1000 rpm to 2000 rpm while the welding speed remained constant at 10 mm/s. These changes corresponded well to those of the YS, UTS, and ductility shown in Figure 4.12. The reason behind this related to the grain size that has already been discussed in detail in the previous section. However, the effect of pin tool thread orientation on the strain hardening exponent was due to the premature failure of right hand threaded FSWed samples. It is obvious from the figure that the data of strain hardening exponent of right hand threaded FSWed sample have more scattered value than the left hand threaded FSWed sample due to the presence of defect at the bottom of the welded joint.

## 4.7.2 Strain Rate Sensitivity

Another important parameter involving the deformation behavior of materials was the strain-rate sensitivity (SRS),  $m$ . The Lindholm [105] approach was used to evaluate the SRS based on the following equation,

$$\sigma = \sigma_0(\epsilon) + \sigma_1(\epsilon) \log \dot{\epsilon} \quad (4.13)$$

The Lindholm SRS is  $\sigma_1(\epsilon)$  in the above equation commonly termed as  $m_L$ . The plot of  $\sigma$  vs  $\log \dot{\epsilon}$  at 2.5% true strain is shown in Figure 4.24, where Lindholm SRS is represented by the slope,  $m_L$ .

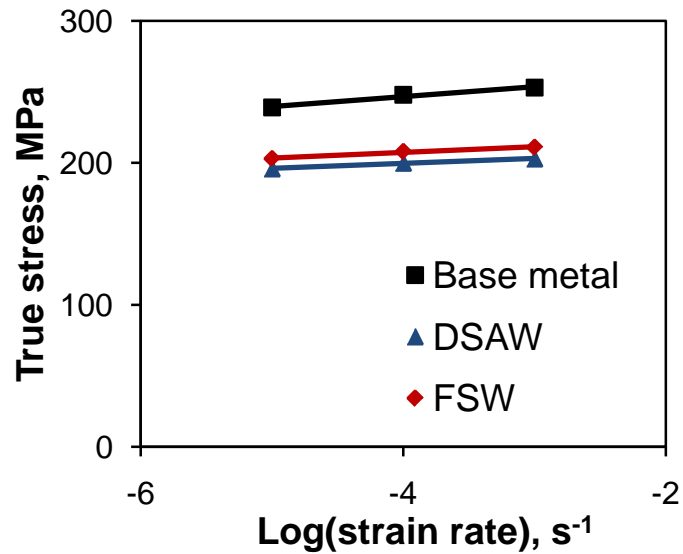


Figure 4.24: A typical plot used to evaluate the strain-rate sensitivity,  $m_L$ , at a true strain value of 2.5% via the Lindholm's approach for the BM, DSAWed and FSWed samples.

The  $m_L$  values for the base metal, DSAWed joints and FSWed joints were 7, 4 and 3.5, respectively. It follows that the SRS became lower after welding, which would be related to the difference in the microstructure and flow stress. del Valle and Ruano [101] have recently presented a relationship between stress, SRS and grain size for the AZ31 alloy as follows,

$$\frac{\partial \sigma}{\partial \ln \dot{\epsilon}} = \frac{k}{2} d^{-1/2} (M_c - 2M_{cg}) + \sigma M_{cg}, \quad (4.14)$$

where  $k$  is Boltzmann constant,  $d$  is the grain size,  $\sigma$  is the flow stress,  $M_{cg} = \partial \ln \sigma_{cg} / \partial \ln \dot{\epsilon}$  and  $M_c = \partial \ln \tau_c / \partial \ln \dot{\epsilon}$ . This equation represents a linear correlation between the SRS, flow stress  $\sigma$  and grain size in the form of  $d^{-1/2}$ . It means that the SRS increased with decreasing grain size. Since the base metal had a smaller grain size and higher flow stress, its SRS would be higher in comparison with that of the welded joints. This is in agreement with the results reported by del Valle and Ruano [101] and Prasad and Armstrong [106].

## 4.8 Tensile Fractography

Figure 4.25 shows typical images of the fracture surfaces of the BM, FSWed and DSAWed samples tested at a strain rate of  $1 \times 10^{-3} \text{ s}^{-1}$ . It is seen from Figure 4.25(a) that dimple-like elongated fracture appeared more apparent. This type of fracture surface denoted ductile fracture that was characterized by cup-like depressions [82]. Some inclusions were present on the fracture surface of AZ31B rolled magnesium alloy. Similar fracture surface characteristics were reported in [78]. As shown in Figure 4.25(b),

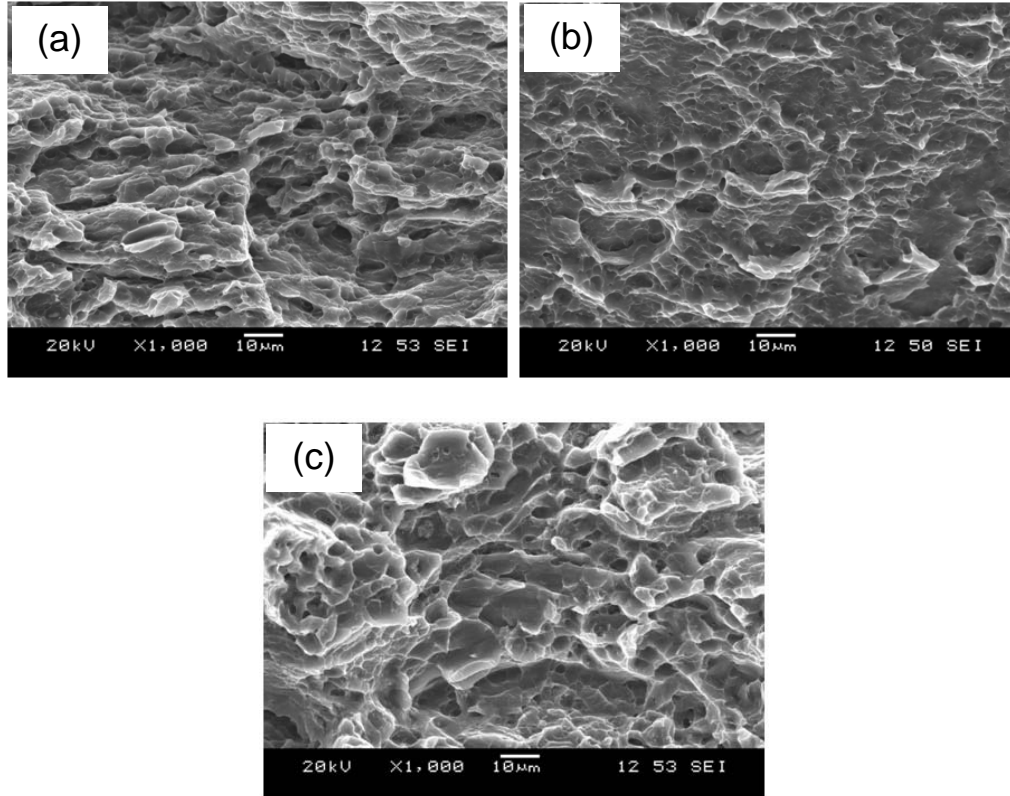


Figure 4.25: Typical SEM images showing the fracture surfaces of samples tested at a strain rate  $1 \times 10^{-3} \text{ s}^{-1}$ . (a) base metal, (b) FSWed sample, and (c) DSAWed sample.

some cleavage-like flat facets in conjunction with dimples and river marking could be seen in the FSWed sample. The river marking was caused by the crack moving through the grain along a number of crystallographic planes which formed a series of plateaus and connecting ledges [82]. The fractographic observations corresponded well to the relatively low percentage elongation of  $\sim 4\%$  in the FSWed samples. While tensile fracture initiation could have started from the area between the weld nugget and the TMAZ as reported by Lim *et al.* [7], the crack initiation occurred from the welding defect at the bottom surface in the present study (Figure 4.4). In the DSAWed sample, more dimples together with fewer cleavage-like facets were observed, as shown in Figure



which was much longer than that of FSWed joints. As the stress amplitude decreased the difference of fatigue life among the welded joints and the BM became smaller in the semi-log scale diagram. The obtained fatigue limit (defined as the fatigue strength corresponding to  $1 \times 10^7$  cycles) and calculated fatigue ratio (the ratio of the fatigue limit to the ultimate tensile strength) of the BM and welded joints are listed in Table 4-3.

Table 4-3 Ultimate tensile strength, fatigue limit and fatigue ratio of the BM, DSAWed and FSWed joints.

Specimen	Fatigue limit (MPa)	Ultimate tensile strength (MPa)	Fatigue ratio
Base metal	50	285	0.175
DSAW	40	236	0.169
FSW	30	169	0.118

The fatigue limit of the DSAWed and FSWed joints dropped down by 20% and 40%, respectively while the fatigue ratio of those two welded joints decreased by about 3.4% and 48%, respectively compared to that of the BM. Significant decrease of fatigue limit and fatigue ratio of FSWed joint was due to the presence of welding defect at the bottom of the joint.

The following Basquin-type equation [82] could be used to fit the obtained fatigue data,

$$\sigma_a = \sigma_f' (2N_f)^b, \quad (4.15)$$

where  $\sigma_a$  is the alternating stress amplitude,  $\sigma_f'$  is the fatigue strength coefficient defined by the stress intercept at  $2N_f = 1$ ,  $N_f$  is the number of cycles to failure and  $2N_f$  is the number of reversals to failure, and  $b$  is the fatigue strength exponent. The obtained  $\sigma_f'$  and

$b$  values are listed in Table 4-4. Fatigue life was indeed associated with both the fatigue strength exponent ( $b$ ) and the fatigue strength coefficient ( $\sigma_f'$ ) based upon Equation 4.15. Normally a smaller value of  $b$  corresponded to a longer fatigue life [82]. From Table 4-4 it can be seen that the value of the fatigue strength exponent i.e. the slope of the curve was in such a sequence (from low to high): BM < DSAWed joints < FSWed joints, while the fatigue strength coefficient was just in the reverse order, i.e., it was highest for the BM, and lowest for the FSWed joints, with the  $\sigma_f'$  value of DSAWed joints lying in-between those of the BM and FSWed joints. This suggested that Basquin-type equation could be used to describe the fatigue life of welded Mg joints.

Table 4-4 Fatigue strength coefficient  $\sigma_f'$  and fatigue strength exponent  $b$  of the base metal, DSAWed and FSWed joints.

Specimen	$\sigma_f'$ (MPa)	$b$
Base metal	274	-0.115
DSAW	185	-0.100
FSW	160	-0.093

#### 4.9.1 Effect of Welding Parameter

Load-controlled fatigue test was performed on different FSWed joints welded by different welding speeds and rotational rates while LHTed weld tool was used in clockwise direction of rotation as shown in Figure 4.27. It is seen that at high stress amplitudes all the FSWed joints had a lower fatigue life than the BM. As the stress

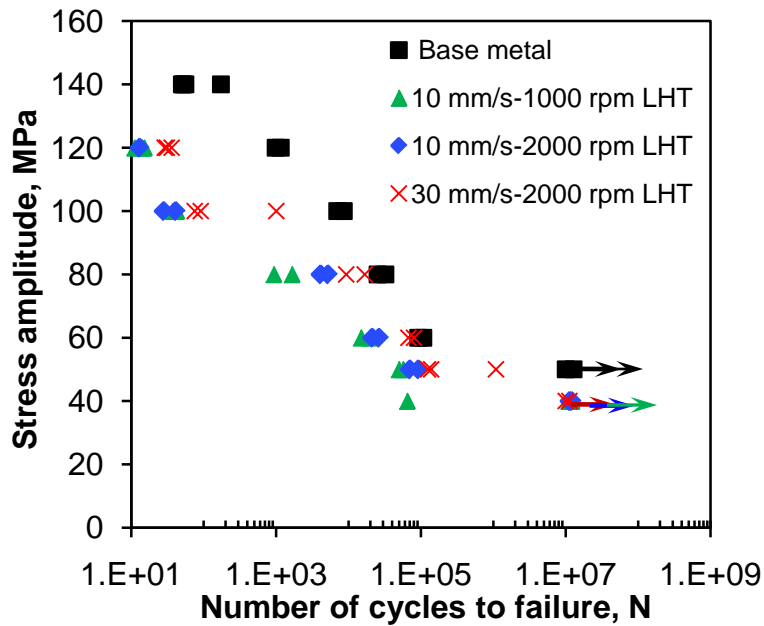


Figure 4.27: S-N curves of the AZ31B base metal and FSWed joints at different welding speeds and rotational rates tested at R=0.1, 50 Hz and room temperature.

amplitude decreased the difference of fatigue life between the FSWed joints and the BM became smaller at low stress amplitudes. From the Figure 4.27 it can be observed that, at very high stress amplitudes and at a very low stress amplitude there is almost no effect of rotational rates. But at moderate stress amplitudes fatigue life increased with increasing rotational rate from 1000 to 2000 rpm while welding speed remained the same. On the other hand, fatigue life further increased with increasing the welding speed from 10 mm/s to 30 mm/s while rotational rate remained constant at 2000 rpm. During FSW low heat was generated at a high welding speed and/or low rotational rate as can be seen from Equation 4.2, leading to a smaller grain size of the FSWed joints that was further associated with the increase of the tensile property as well as the fatigue property. The obtained fatigue limit (defined as the fatigue strength corresponding to  $1 \times 10^7$  cycles) and

fatigue ratio (the ratio of the fatigue limit to the ultimate tensile strength) of the FSWed joints at different welding speeds and rotational rates are listed in Table 4-5. Fatigue ratio of the FSWed sample at a welding speed of 30 mm/s and rotational rate of 2000 rpm was the smallest among all of the welded joints indicating that this FSWed joint had comparatively poor fatigue performance than its tensile performance. It is mentioned earlier that, during FSW, low heat input is engendered at high welding speed and rotational rate leading to the formation of kissing bond defects or other lack-of-bonding defects that might established fatigue initiation due to the inadequate plasticization of the material caused by the insufficient heat energy input. However, it is also important to be mentioned that, the effect of kissing bond on the fatigue properties of FSWed sample (specifically, the FSWed sample at 30 mm/s welding speed and 2000 rpm rotational rate) became more pronounced as stress amplitudes decreased i.e. long time fatigue testing.

Table 4-5 Ultimate tensile strength, fatigue limit and fatigue ratio of the BM and FSWed joints at different welding speeds and rotational rates.

Welding parameter	Pin thread orientation	Fatigue limit (MPa)	Tensile strength (MPa)	Fatigue ratio
Base metal	-	50	285	0.175
10 mm/s and 1000 rpm	LHT	40	212	0.190
10 mm/s and 2000 rpm	LHT	40	211	0.190
30 mm/s and 2000 rpm	LHT	40	239	0.167

## 4.9.2 Effect of Thread

Figure 4.28 depicts the effect of thread of friction stir welding tool on the fatigue properties of friction stir weld tool at a welding speed of 10 mm/s and rotational rate of 2000 rpm.

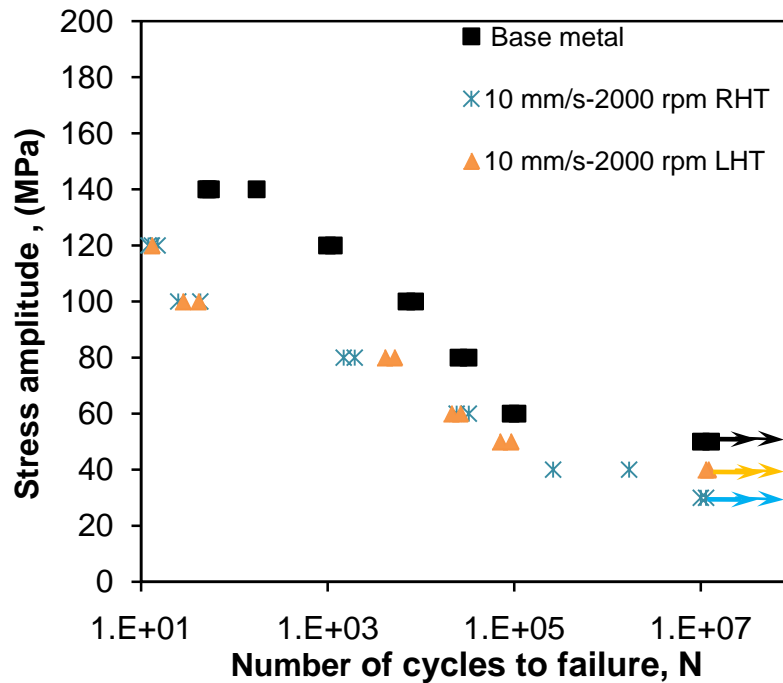


Figure 4.28: S-N curves of the AZ31B base metal and FSWed joints at 10 mm/s welding speed and 2000 rpm rotational rate using LHT and RHT weld tool tested at R=0.1, 50 Hz and room temperature.

From this figure it is observed that at high stress amplitude both welded samples experienced almost the same fatigue life while at low stress amplitude or long term fatigue testing the effect of thread is more pronounced. The obtained fatigue limit and calculated fatigue ratio of the BM and FSWed joints are listed in Table 4-6. As expected, the fatigue limit of the FSWed joints using RHT weld tool dropped down by 25% due to

the presence of weld defect at the bottom of the welded joint compared to that of the FSWed sample using LHT weld tool. Defect formation at the bottom of the FSWed sample using RHT weld tool was discussed at the beginning of this Chapter and stated that the LHT pin tool in the clockwise rotation (Figure 4.5(b)) would give rise to better joints while the RHT pin tool in the clockwise rotation (Figure 4.5(a)) would result in the occurrence of potential porosity or lack-of-bonding defects due to two possible reasons as follows.

Table 4-6 Ultimate tensile strength, fatigue limit and fatigue ratio of the BM and FSWed joints at different welding speeds and rotational rates.

Welding parameter	Pin thread orientation	Fatigue limit (MPa)	Tensile strength (MPa)	Fatigue ratio
Base metal	-	50	285	0.175
10 mm/s and 2000 rpm	LHT	40	211	0.190
10 mm/s and 2000 rpm	RHT	30	207	0.145

Firstly, the FSW was considered to be a constant volume welding process and the upward material movement would cause the plasticized material to stick to the shoulder and pin [48], which would reduce the supply of plasticized material at the bottom. Secondly, due to a certain extent due to the temperature gradient between the top surface in contact with the shoulder and bottom surface in touch with the clamping support [43], the material flow near the bottom surface would encounter more flow resistance when it moved upward. Therefore, the welds obtained using the RHT pin in the clockwise rotation had

higher probability to form porosity or lack-of-bonding defects near the bottom surface. Such defects were clearly seen from the fracture surface after fatigue testing of the FSWed joints made with the RHT pin tool in the clockwise rotation (Figure 4.29(a)), while no such defects were observed in the FSWed joints made with the LHT pin tool in the clockwise rotation (Figure 4.29(b)).

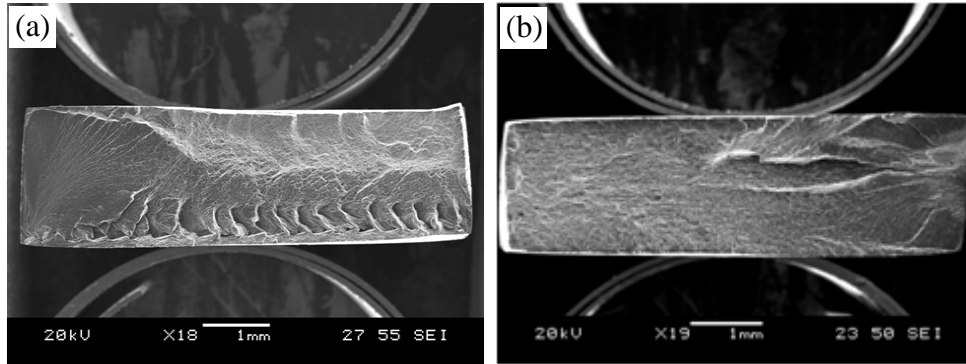


Figure 4.29: SEM images showing the fracture surfaces of the FSWed samples, after fatigue testing at a stress amplitude of 60 MPa, made with (a) RHT pin tool; (b) LHT pin tool in the clockwise rotation.

#### 4.10 Fatigue Fractography

Figure 4.30 shows typical SEM images taken from the fracture surface of a FSWed sample made with the LHT pin tool in the clockwise rotation at a stress amplitude of 60 MPa. Fatigue crack initiation occurred either from the defects or unmelted particles present at the specimen surface as shown in Figure 4.29 and Figure 4.30(a). The presence of an Al-Mn particle was responsible for the initiation during fatigue testing as shown in Figure 4.30(b), (c) and (e). For the FSWed samples made with the RHT pin tool in the clockwise rotation fatigue crack initiation was observed to initiate from the bottom surface welding defects, since the lack-of-bonding defects or pores could act as stress

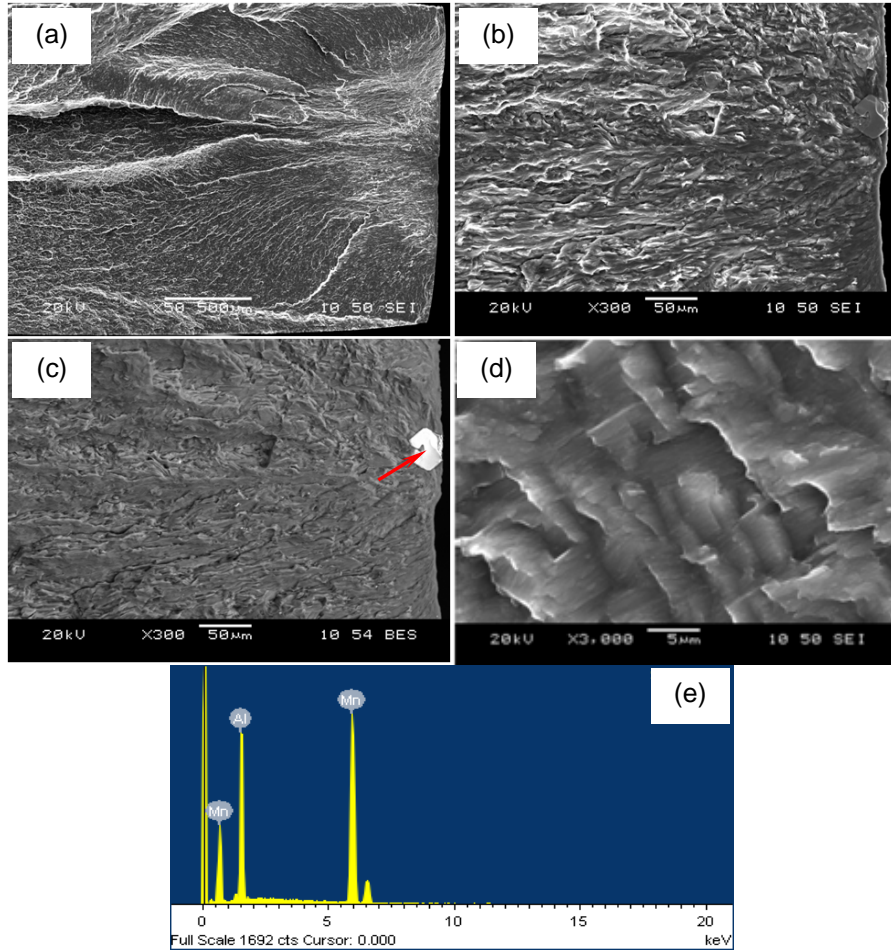


Figure 4.30: Typical SEM images of the fatigue fracture surface of a FSWed sample made with the LHT pin tested at a stress amplitude of 60 MPa. (a) fatigue crack initiation area at a low magnification; (b) fatigue crack initiation area at an intermediate magnification; (c) backscattered electron image of (b); (d) fatigue crack propagation area at a high magnification; (e) EDS spectrum of the particle near the surface on the image (c) indicated by an arrow.

raisers, facilitating crack initiation. Fatigue crack propagation was basically characterized by fatigue striations (Figure 4.30(d)), which were usually perpendicular to the propagating direction with the spacing increasing with increasing distance from the

initiation site. While the fatigue striations normally occurred by a repeated plastic blunting-sharpening process in the face-centered cubic materials due to the slip of dislocations in the plastic zone ahead of the fatigue crack tip, the formation of the fatigue striations in the magnesium alloys was expected to be related to the twinning in the compressive phase and detwinning in the tensile phase [107-109]. Further studies are needed in this aspect.

## **CHAPTER 5**

### **MECHANICAL PROPERTIES OF LASER WELDED AZ31B**

#### **Mg JOINTS**

##### **5.1 Microstructure of the Fiber and Diode Laser Welded Joints**

There are two ways or modes that energy can be transferred from the laser to the material to be welded. Depending on the power density the laser welding can be in either conduction mode or keyhole mode. Figure 5.1 shows schematically (a) the keyhole welding and (b) the conduction welding for the FLWed and DLWed joints, respectively. The keyhole welding melts a keyhole or hole in the material being welded, due to the higher energy density (such as FLW) delivered to the material, and as the beam moves forward, the molten metal fills in behind it. On the other hand, conduction welding is a low energy density weld (such as DLW) in which the laser beam basically heats the surface of the material being welded and the heat is gradually transferred to the bottom of the material through heat-conduction. The top weld bead after FLW and DLW appeared to be very good after complete cleaning of the oxides as can be seen from Figure 5.2(a,b), respectively. Because of solidification shrinkage and thermal contraction of the weld metal during welding, the workpiece has a certain tendency to distort. Due to the deep narrow keyhole in FLW, the weld bead was very narrow both at the top and the bottom and no distortion was observed. However, DLWed workpiece shrank in the upward

direction and the weld tended to be wider at the top than at the bottom, causing more solidification shrinkage and thermal contraction at the top of the weld.

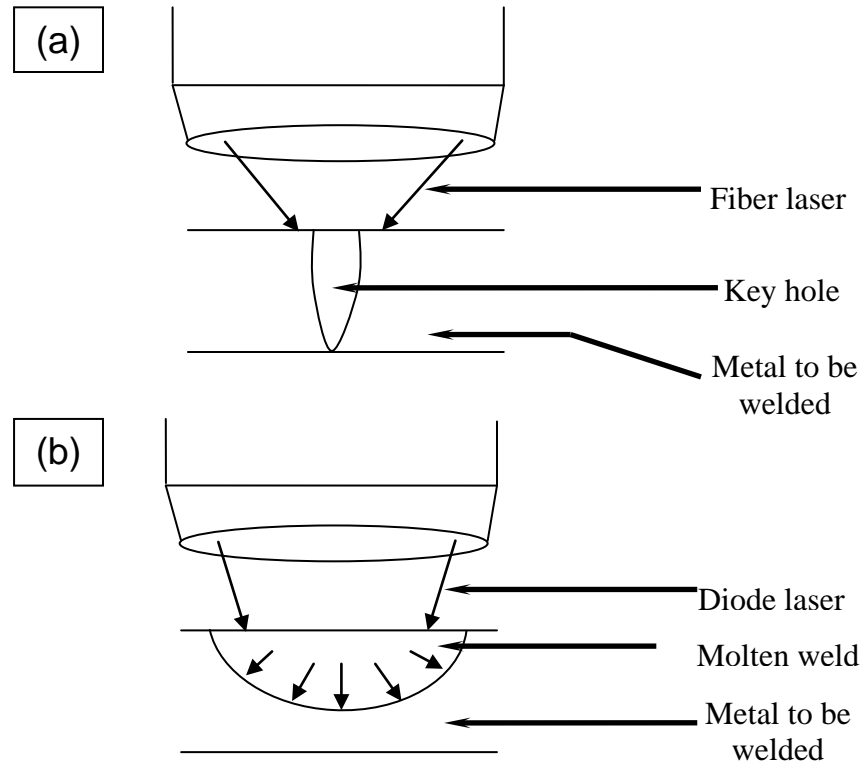


Figure 5.1: Schematic illustration of (a) keyhole and (b) conduction modes during laser welding.

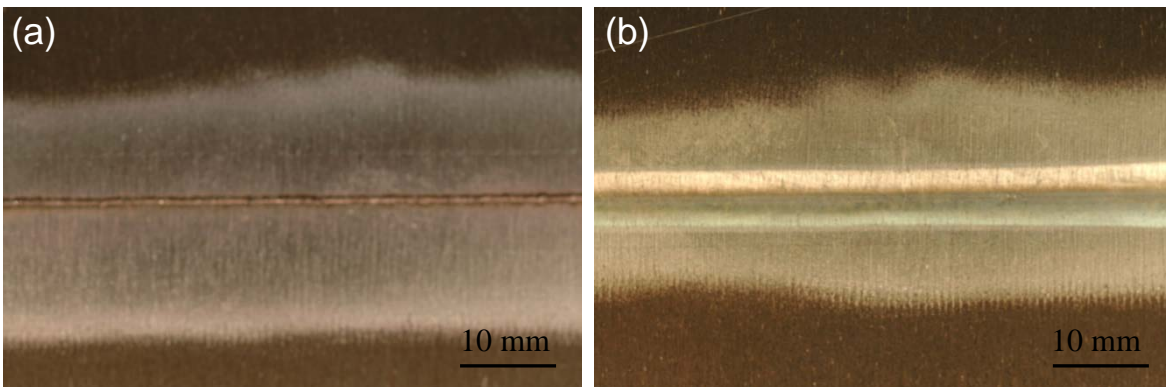


Figure 5.2: Weld bead of (a) fiber laser and (b) diode laser welded joints.

Consequently, the resultant angular distortion is upward [110]. The microstructures of the FLW and DLW along with the cross sections are shown in Figure 5.3 and 5.4, respectively. The fusion boundary of FLWed joint had a slight hourglass shape (Figure 5.3(a)) with an aspect ratio (width/height) of about 0.5, while the DLWed joint was featured by a weld droplet (Figure 5.4(a)) with an almost hemispherical shape. In Figure 5.3(b) elongated and pancake-shaped grains with varying sizes were observed in the BM. The heterogeneity in the grain structure of the BM was due to both deformation of the 2 mm thick sheet by rolling and incomplete dynamic recrystallization (partial annealing) [15]. The average grain size of the BM was observed to be  $3.6 \pm 2.2 \mu\text{m}$ . Equiaxed grains were observed in the HAZ in both types of laser welded joints as shown in Figure 5.3(c) and Figure 5.4(b), suggesting that recrystallization occurred in the HAZ. Figures 5.3(d), 5.3(e), 5.4(c) and 5.4(d) depict the columnar grains along with columnar dendrites adjacent to the solid/liquid boundary or fusion line. It is seen that the growth direction of the columnar grain was almost perpendicular to the boundary of fusion line due to the large thermal gradient, termed as epitaxial grain growth. Savage et al. [111] first observed epitaxial grain growth in fusion welding using the Laue X-ray back reflection technique. In fusion welding the existing BM grains at the fusion line acted as the substrate for nucleation. Since the liquid metal of the weld pool was in intimate contact with these substrate grains and wetted them completely, crystals nucleated from the liquid metal upon the substrate grains without alternating their existing crystallographic orientations.

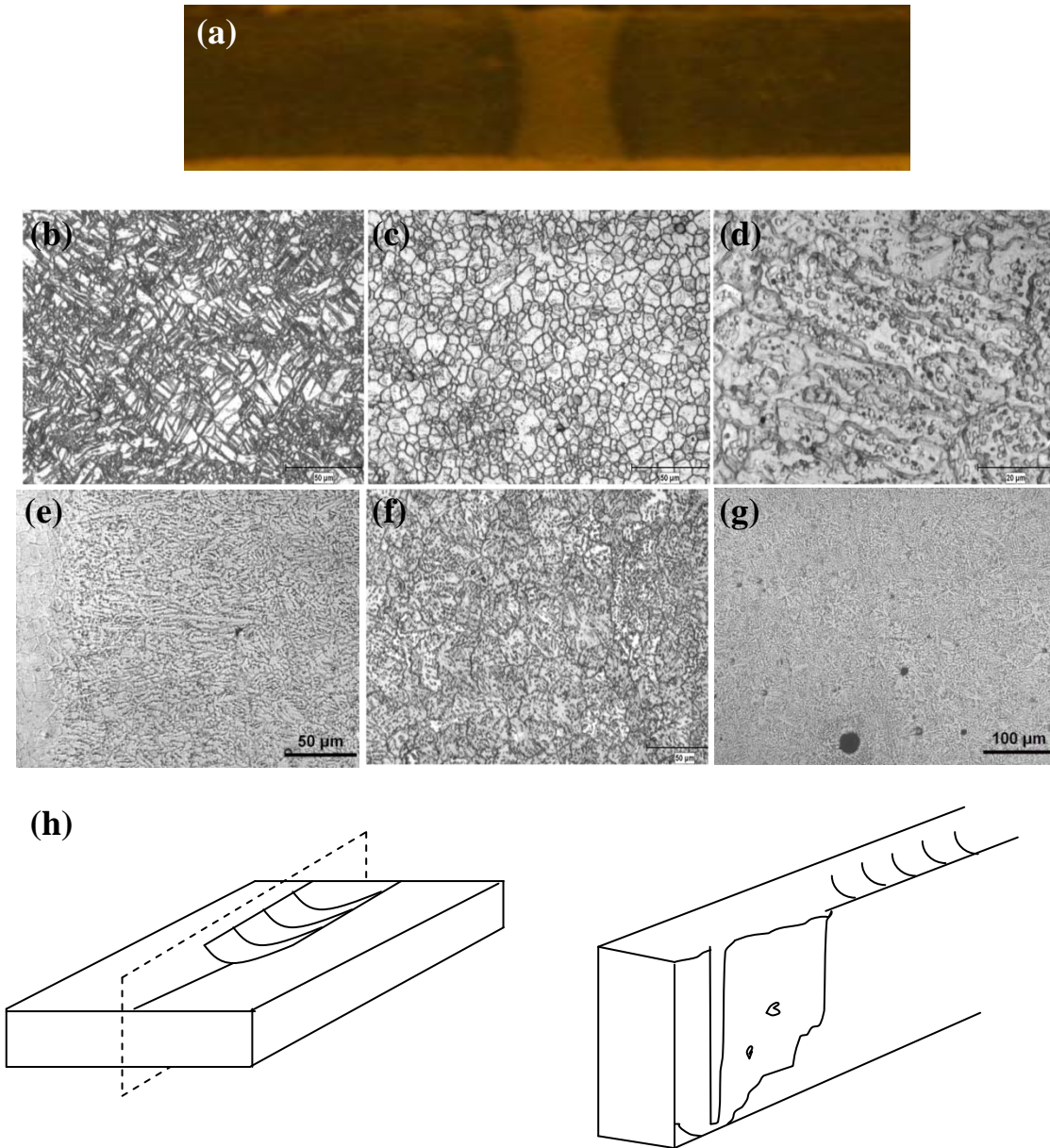


Figure 5.3: Typical macroscopic and microscopic structures of a fiber laser welded joint at a welding speed of 100 mm/s. (a) cross section of the welded joint, (b) base metal (BM) (etchant 1), (c) heat-affected zone (HAZ) at 400X (etchant 1), (d) columnar dendrites in the boundary of fusion zone (FZ) at 1000X (etchant 1), (e) columnar dendrites at 400X (etchant 2), (f) FZ at 400X (etchant 1) and (g) FZ at 200X (etchant 2) and (h) schematic diagrams of the bubble formation in the FZ.

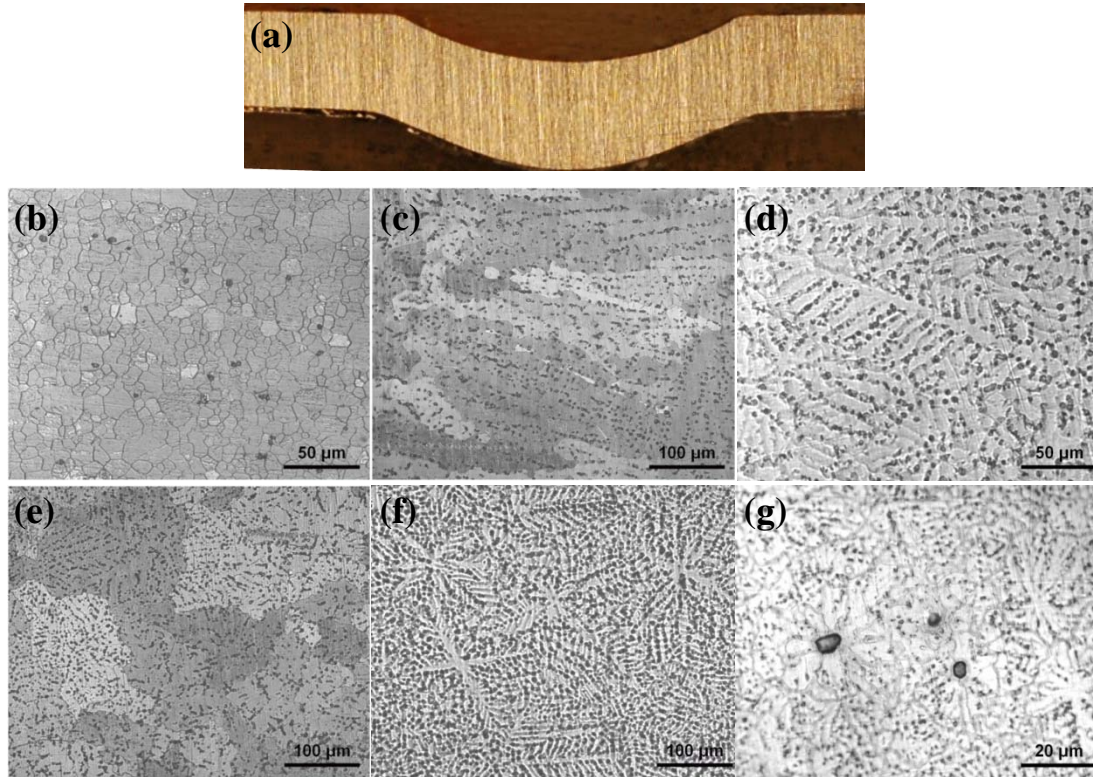


Figure 5.4: Typical macroscopic and microscopic structures of a diode laser welded joint at a welding speed of 8.33 mm/s. (a) cross section of the welded joint, (b) heat-affected zone (HAZ) at 400X (etchant 1), (c) columnar dendrites at 200X (etchant 1), (d) columnar dendrites at 400X (etchant 2), (e) fusion zone (FZ) at 200X (etchant 1), (f) FZ at the same magnification (etchant 2) and (g) heterogeneous nuclei in the FZ (etchant 2).

To identify better the grain structure and dendrites in the FZ of the laser welded joints, two different kinds of etchants were employed individually in the present study as discussed in Chapter 3. Etchant 1 (with water) was used to reveal the grain structure as shown in Figures 5.3(d), 5.3(f), 5.4(c), 5.4(e), while etchant 2 (without water) was used to reveal the dendrites only (Figures 5.3(e), 5.3(g), 5.4(d), 5.4(f) and 5.4(g)). Water was a key ingredient that made the difference between those two etchants. When etching took

place the etchant with water (etchant 1) preferentially attacked the high energy grain boundaries that reflected the light away from the eyepiece and appeared as dark grain boundary lines. During the solidification of an alloy, the temperature gradient of the solid-liquid interface,  $G$  and the growth rate,  $R$  played a crucial role producing the planar, cellular or dendritic microstructure in the FZ. The ratio  $G/R$  determines the mode of solidification (planar, columnar or equiaxed dendrites) while the product  $GR$  indicates the cooling rate that governs the size of the solidification structure. A number of papers have been published to identify the effect of  $G$  and  $R$  on the microstructure in the FZ [112-115]. To facilitate the understanding of the effect of  $G/R$  and  $GR$  on the morphology and size of solidification microstructures, a schematic plot is shown in Figure 5.5 [116].

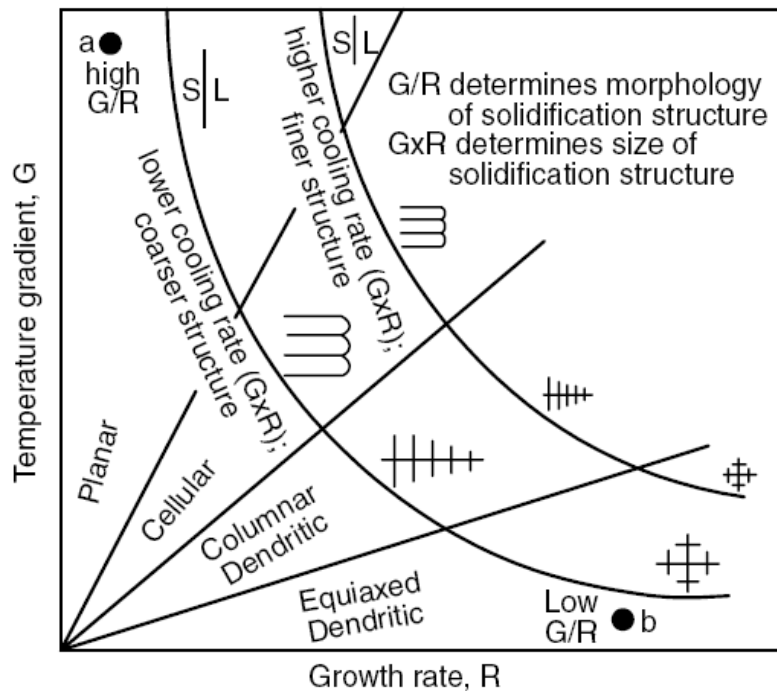


Figure 5.5: Effect of temperature gradient  $G$  and growth rate  $R$  on the formation of various solidification microstructures [116].

It is seen that at the boundary of the fusion line the temperature gradient was moderate which resulted in columnar dendrites in both welded joints, while in the center of the FZ the dendrites became equiaxed due to a lower temperature gradient. As FLW had a higher cooling rate, both the columnar and equiaxed dendrites were observed to be small in comparison with above of the DLWed joint. Bubble formation was observed during FLW as shown in Figure 5.3(h). Bubbles were generated from the tip of the keyhole and then rotated at the bottom portion of the molten pool just behind the keyhole as schematically shown in Figure 5.3(h). Some bubbles were trapped at the solidifying front of the FZ which resulted in porosity [117]. Figure 5.4(g) shows a typical image with three (dark) heterogeneous nuclei at the center of three equiaxed grains in the FZ of the DLWed joints. Similar type of heterogeneous nuclei were also observed in the FLWed joints at a higher magnification of SEM image (Figure 5.6), where EDS analysis revealed that these particles were the unmelted BM Mn-Al containing inclusions still existing in the weld pool they act as heterogeneous nuclei upon which atoms in the liquid metal can be arranged in a crystalline form. EDS analysis further indicated that in both types of laser welded joints a large number of precipitates were present along with Mn-Al containing particles/inclusions. As an example, Figure 5.7 revealed clearly the presence of divorced eutectic structure in the FZ of the DLWed joint on the left hand-side along with the unmelted Mn-Al particle on the right hand side, although both particles had the similar white color in the image. The presence of the divorced eutectic-like structure was due to the fast non-equilibrium cooling of the weld pool after welding. A normal eutectic structure in the form of alternating layers of  $\alpha$  and  $\beta$  would not be possible in the AZ31

Mg alloy containing 3 wt% Al based on the equilibrium phase diagram for an infinitely slow cooling rate.

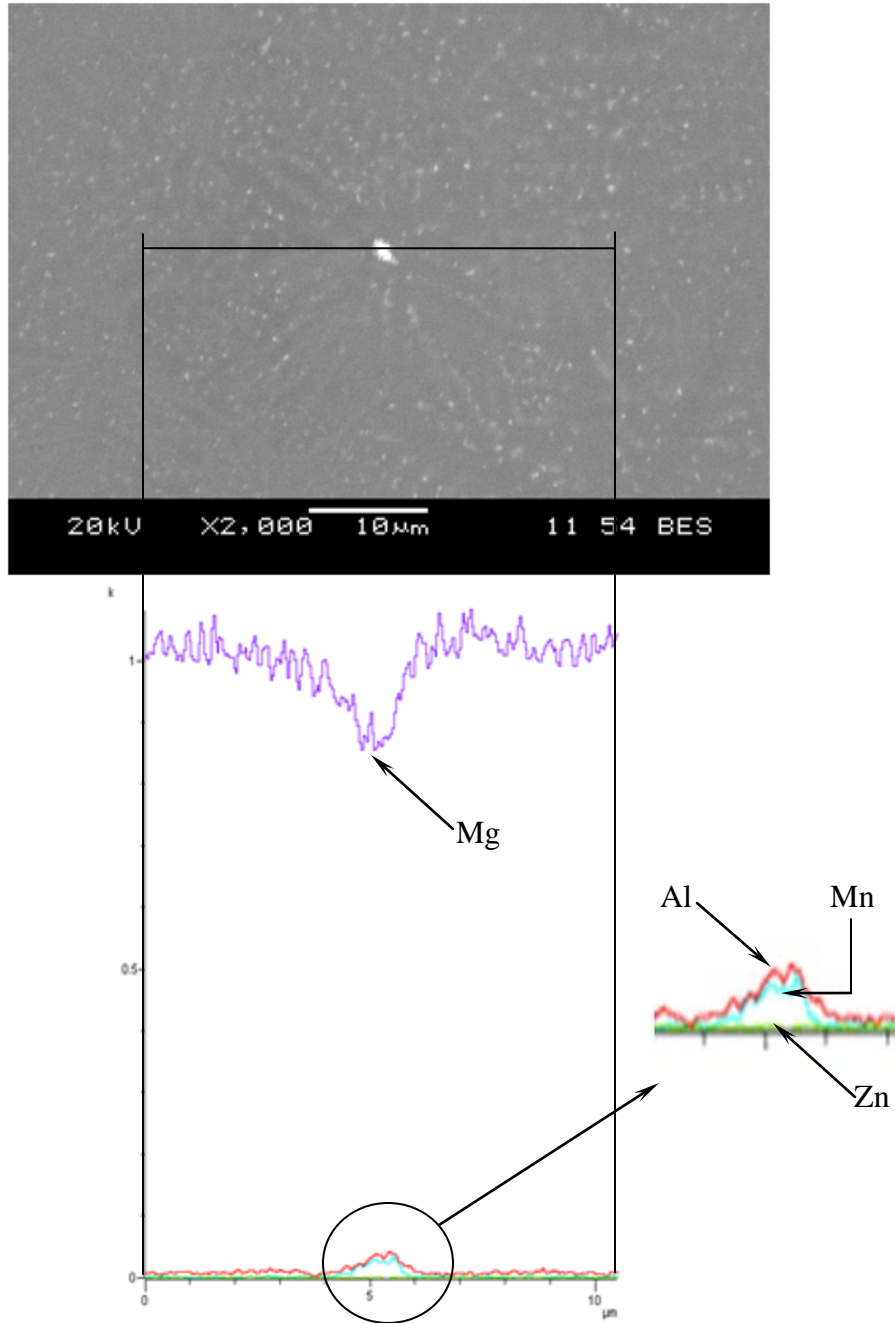


Figure 5.6: EDS line scan showing the typical compositional variation across a particle in the FZ of FLWed joint.

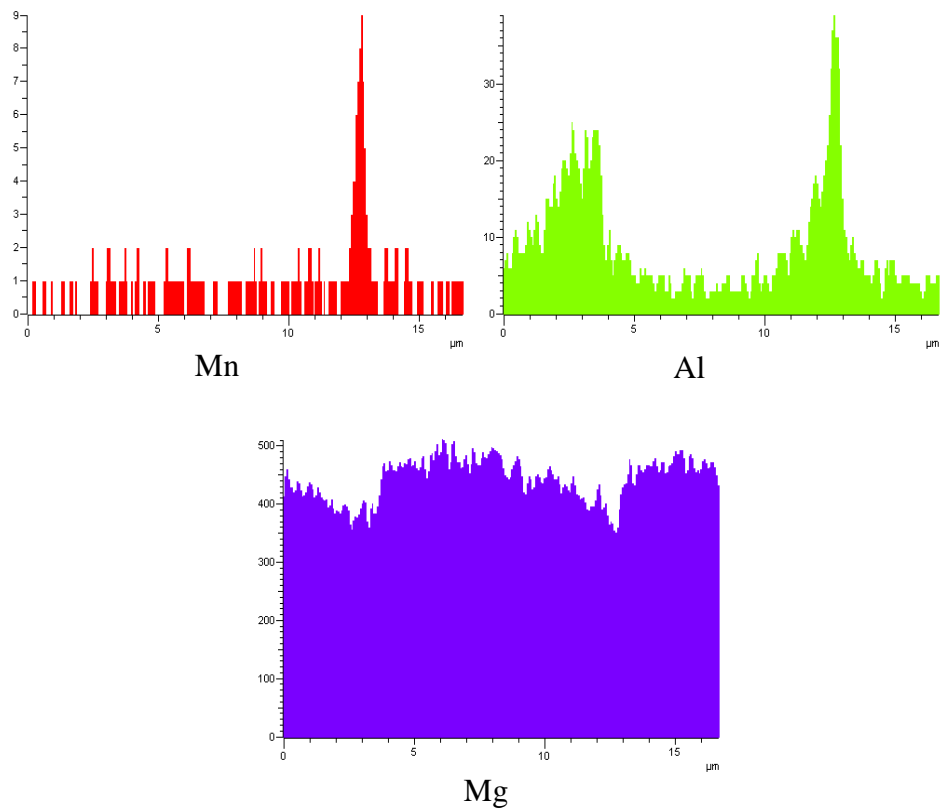
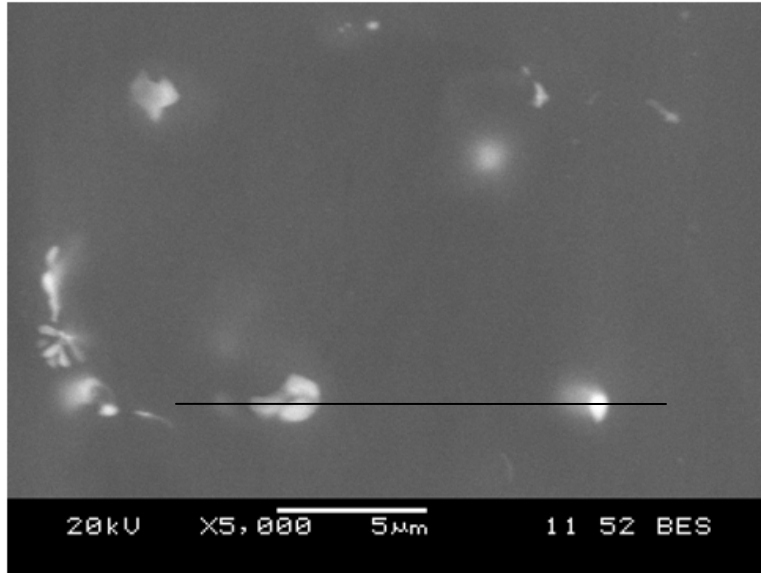


Figure 5.7: EDS line scan showing the typical compositional variation across two particles in the FZ of DLWed joint.

## 5.2 Micro-hardness

Typical hardness profiles across the FLWed and DLWed AZ31B Mg alloy are shown in Figure 5.8.

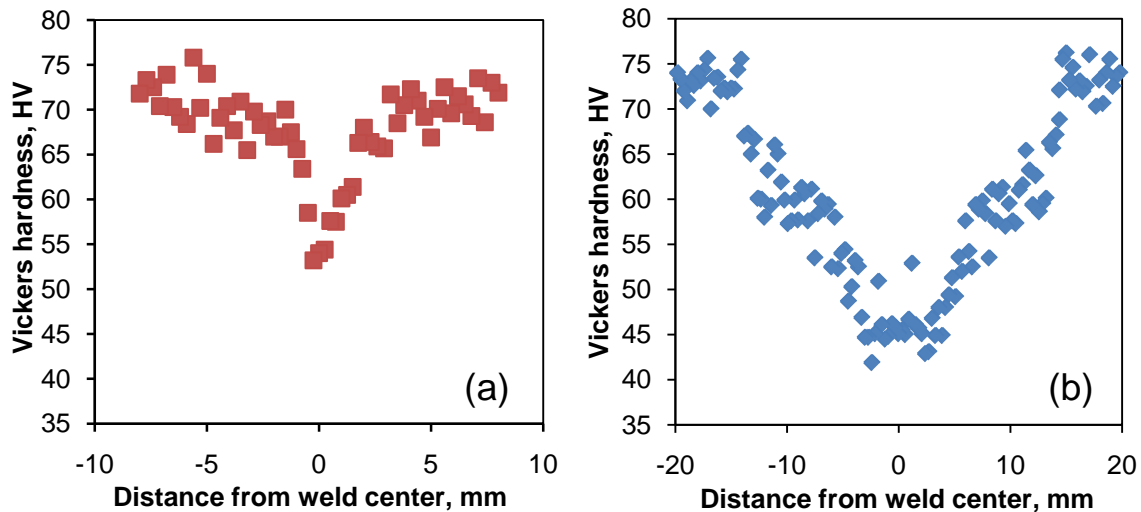


Figure 5.8: Typical microhardness profile of (a) fiber laser welded joint at a welding speed of 100 mm/s and (b) diode laser welded joint at a welding speed of 8.33 mm/s.

It is seen that the hardness value decreased from about HV 73~74 in the half-hardened H24 temper BM to approximately HV 53 at the center of the FZ, indicating narrow FZ and HAZ in the FLWed joint (Figure 5.8(a)), while in the DLWed joint much wider FZ and HAZ were obvious (Figure 5.8(b)). Besides, the lowest hardness at the center of the DLWed joint became about HV 45, which was lower than that of the FLWed joint with a hardness of about HV 55. This was associated with the faster cooling rate during the FLW due to the smaller amount of weld pool in comparison with the DLW, leading to a smaller grain size in the FZ (Figure 5.3(f), 5.3(g), 5.4(e) and 5.4(f)). The reduction in the hardness was attributed to the significant microstructural changes after laser welding. In

the FZ (Figure 5.3(f), 5.3(g) and 5.4(f)), the non-equilibrium cast structures formed, in conjunction with larger grain size in the FZ in comparison with the BM (Figure 5.3(b)). Furthermore, the grain shape changed significantly from the deformed and elongated (or pancake-shaped) grains in the half-hardened H24 condition (Figure 5.3(b)) to the fully annealed or recrystallized equiaxed grains in the HAZ (Figure 5.3(c) and 5.4(b)). All of these factors led to the hardness changes shown in Figure 5.8(a-b).

### 5.3 Tensile Strength and Ductility

Figure 5.9 shows typical engineering stress versus engineering strain curves of the BM, FLWed and DLWed AZ31Mg alloy sheets tested at a strain rate of  $1 \times 10^{-4} \text{ s}^{-1}$ .

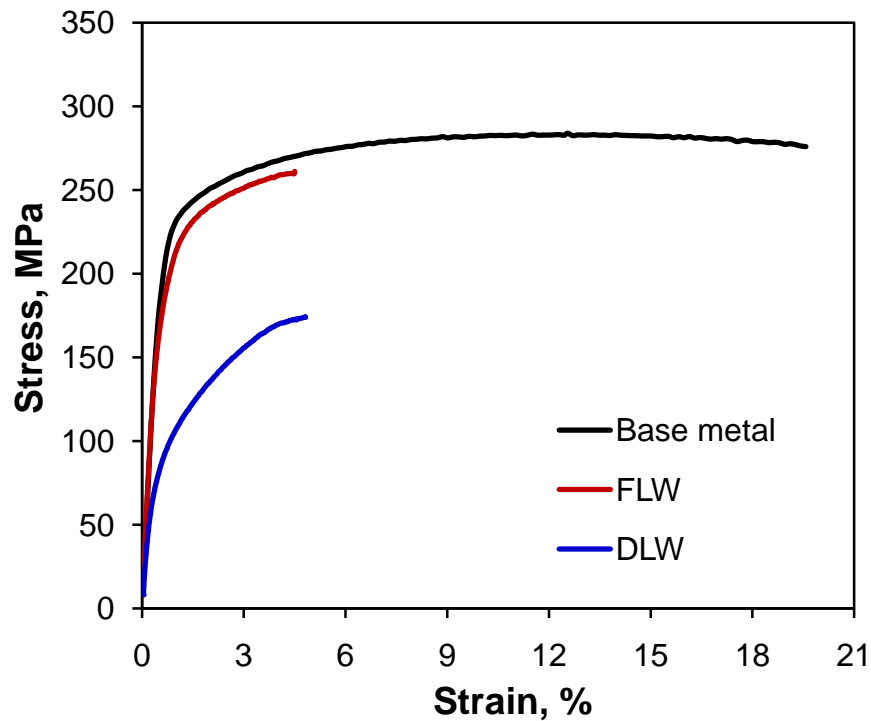


Figure 5.9: Typical engineering stress-strain curves of the AZ31B Mg alloy, fiber laser and diode laser welded samples tested at a strain rate of  $1 \times 10^{-4} \text{ s}^{-1}$ .

It is seen that after welding, both the strength and the elongation (%El) reduced. The joint efficiency was observed to be about 91% for the FLWed joint and 59% for the DLWed joint in comparison with the base metal (BM). The significant reduction of the tensile strength for the DLWed joint would be related to the larger grain size in the FZ (Figure 5.4(e,f)) and irregular shape (weld droplet, Figure 5.4(a)) of the weld bead that reduced the load capability during testing. The weld had a typical cast structure containing the divorced eutectic brittle precipitates, which was very different from that of the rolled and partially annealed BM. As a consequence, the ductility of both types of welded joints reduced notably. All FLWed joints fractured at the boundary of HAZ and columnar dendrites (Figure 5.3(e)), while DLWed joints fractured almost exclusively at the centre of the FZ due to weld droplet. From Figure 5.10 it was observed that the YS and UTS of the FLWed joints, which were fairly close to those of the BM, were much higher than those of the DLWed joints although the ductility of both types of laser welded joints was essentially the same at different strain rates. The YS and UTS of the BM increased slightly with increasing strain rate while ductility decreased drastically. This means that BM was strain rate sensitive while both the welded joints were not. This is due to the presence of smaller elongated grain structure in the BM as shown in Figure 5.3(b). The details of the strain rate sensitivity have been discussed in Chapter 4.

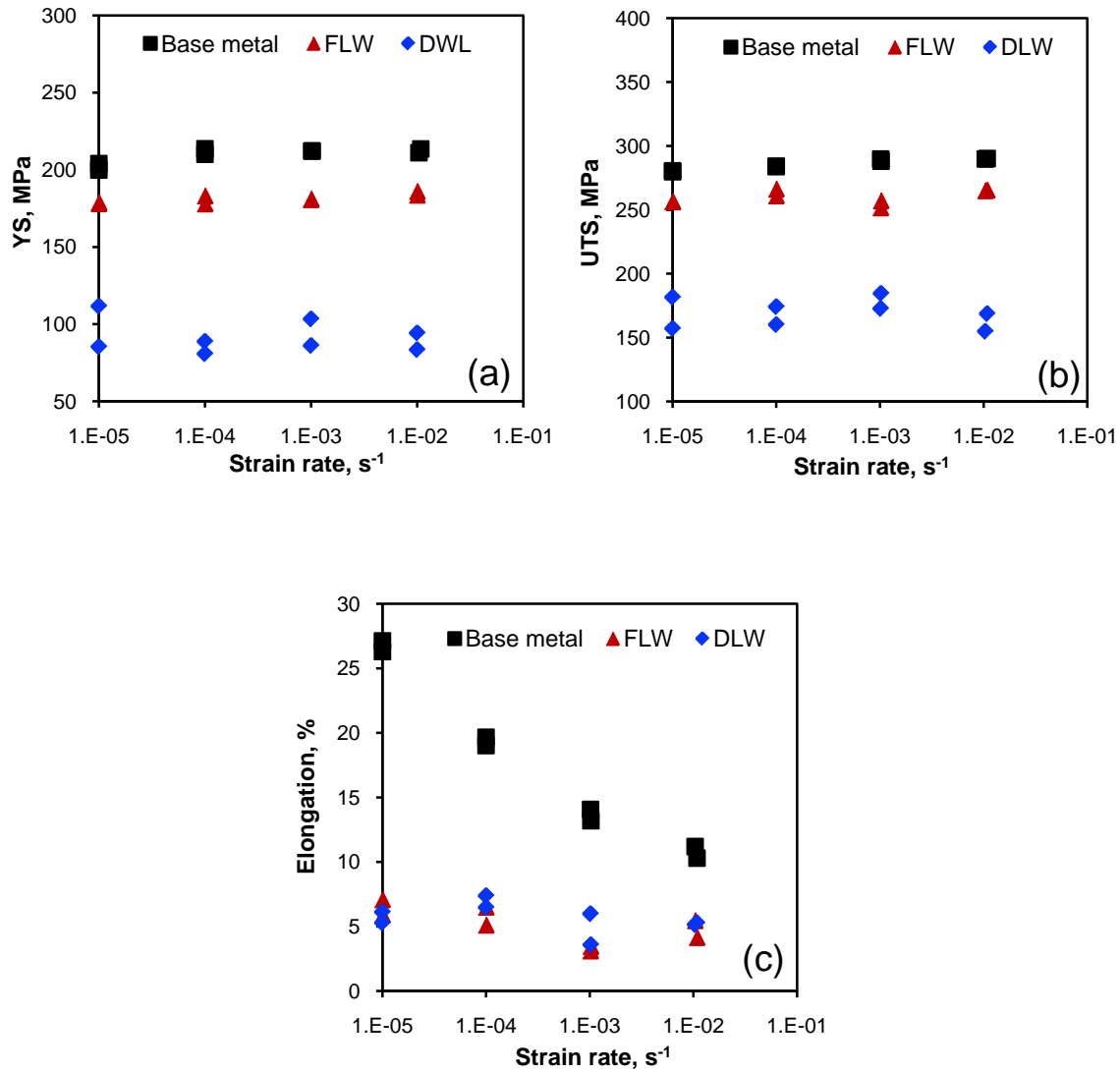


Figure 5.10: Effect of strain rate on (a) yield strength (YS) (b) ultimate tensile strength (UTS) and (c) ductility of the FLWed and DLWed samples.

## 5.4 Strain Hardening Behavior

The hardening capacity (as discussed in Chapter 4) of the BM and the welded samples are evaluated by using Equation 4.6 listed in Table 5-1. It is seen that the hardening

capacity of the DLWed joint increased more than twice that of the BM while the FLWed joint only showed a slight increase in the hardening capacity.

Table 5-1: Hardening capacity of the base alloy, FLWed and DLWed samples tested at different strain rates.

Specimen	Strain rate ( $s^{-1}$ )	Hardening capacity ( $H_c$ )
Base metal	$1 \times 10^{-2}$	0.37
	$1 \times 10^{-3}$	0.36
	$1 \times 10^{-4}$	0.36
	$1 \times 10^{-5}$	0.41
FLW	$1 \times 10^{-2}$	0.43
	$1 \times 10^{-3}$	0.41
	$1 \times 10^{-4}$	0.46
	$1 \times 10^{-5}$	0.44
DLW	$1 \times 10^{-2}$	0.83
	$1 \times 10^{-3}$	0.90
	$1 \times 10^{-4}$	0.98
	$1 \times 10^{-5}$	0.73

To facilitate the understanding of the hardening capacity, the evaluation of the strain hardening exponents ( $n$  and  $n^*$ ) as a function of strain rate for the BM, FLWed and DLWed joints are shown in Figure 5.11. Only the data lying in-between the YS and UTS were used to evaluate the value of  $n$  and  $n^*$ . While almost no effect of strain rate on the strain hardening exponents was seen within the experimental scatter, it was clear that the strain hardening exponents after DLW became much higher due to the significant microstructural change (Figure 5.4), in agreement with the results shown in Table 5.1. The values of  $n^*$  were more than twice those of  $n$  due to the exclusion of elastic deformation amount in the evaluation of  $n^*$  value expressed by Equation 4.9.

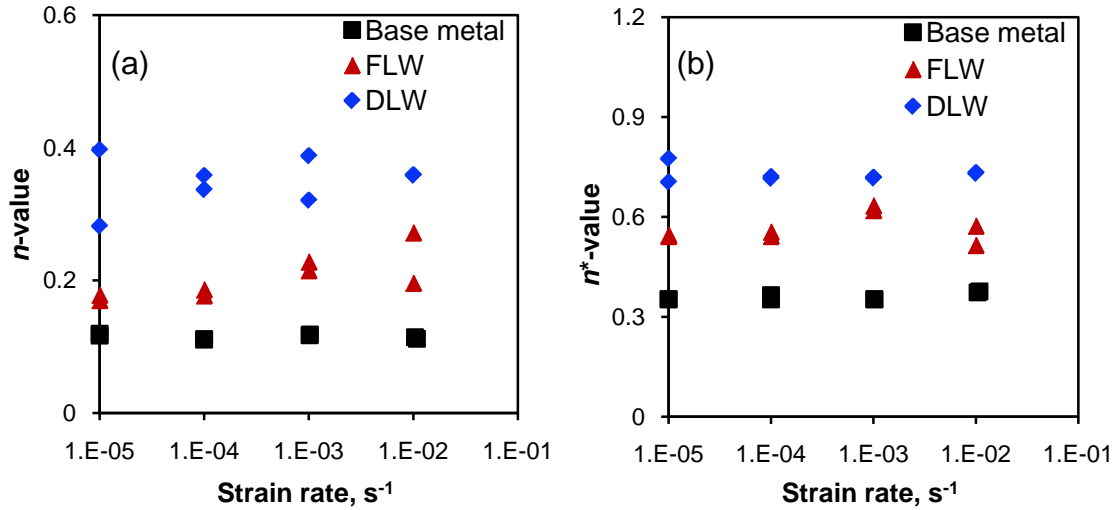


Figure 5.11: Effect of strain rate on (a) n-value, and (b) n\*-value of the FLWed and DLWed samples.

Figure 5.12 represents a typical Kocks-Mecking plot along with stage III and stage IV that has already been discussed in the previous chapter, section 4.6.5. From the figure, it can be observed that at lower strain, the strain hardening capacity of the BM characterized by smaller grain size was higher while at larger strain DLWed joint with larger grain size dominated. The strain hardening could be understood on the basis of the grain size strengthening and dislocation strain hardening as discussed in the previous chapter section 4.6.5. According to the Equation 4.12 strain hardening behavior depends on the summation of both Taylor dislocation and Hall-Petch contribution. For the readers convenience it is important to note that, Hall-Petch contribution is inversely proportional to the grain size. On the other hand, Taylor contribution is directly proportional to the dislocation density that is further associated proportionally with the grain size. Sinclair *et al.* [102] and Kovacs *et al.* [103] reported that, at lower strains due to the presence of small grain size in the BM, Hall-Petch contribution is more pronounced than Taylor

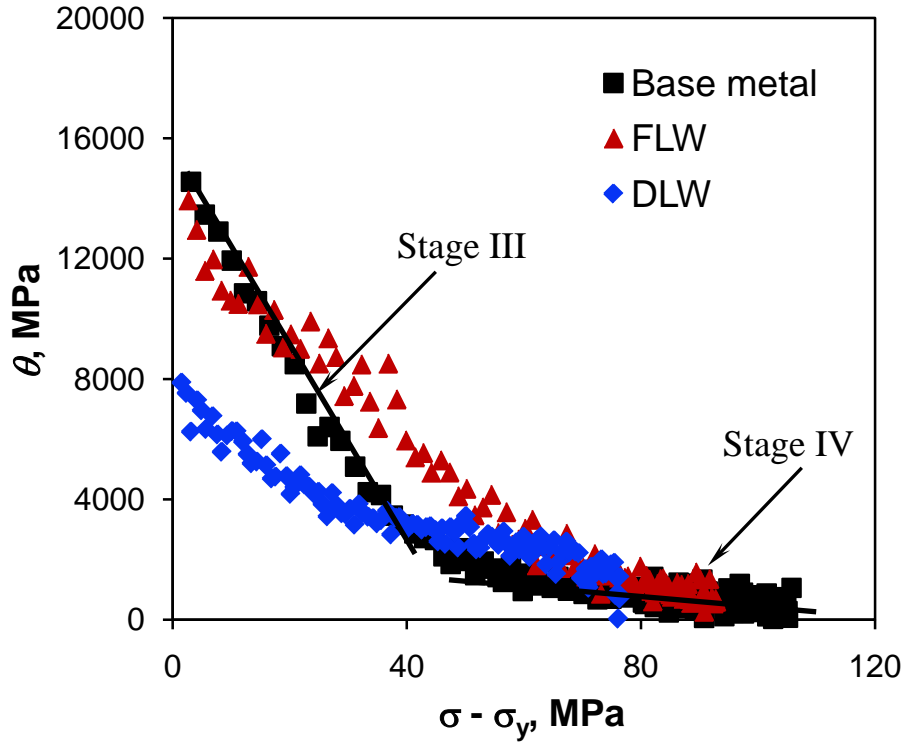


Figure 5.12: Strain hardening rate ( $\theta$ ) versus net flow stress ( $\sigma - \sigma_y$ ) of the FLWed and DLWed samples tested a strain rate of  $1 \times 10^{-3} \text{ s}^{-1}$ .

dislocation and strong strain hardening capacity observed in the BM but at higher strains the influence of the grain size (i.e. Hall-Petch contribution) on the strain hardening vanished due to dislocation screening and dynamic recovery effects at grain boundaries. As a result, at large strain, larger grain size provided more space to accommodate dislocations and enhanced Taylor contribution to the strain hardening capacity. As the grain size of the DLWed samples was larger, a strong strain hardening rate was observed at large strain in comparison with the BM and FLWed joint (Figure 5.12).

## 5.5 Tensile Fractography

Figure 5.13 shows some typical SEM images of fracture surfaces of FLWed and DLWed samples after tensile tests at a strain rate of  $1 \times 10^{-5} \text{ s}^{-1}$ .

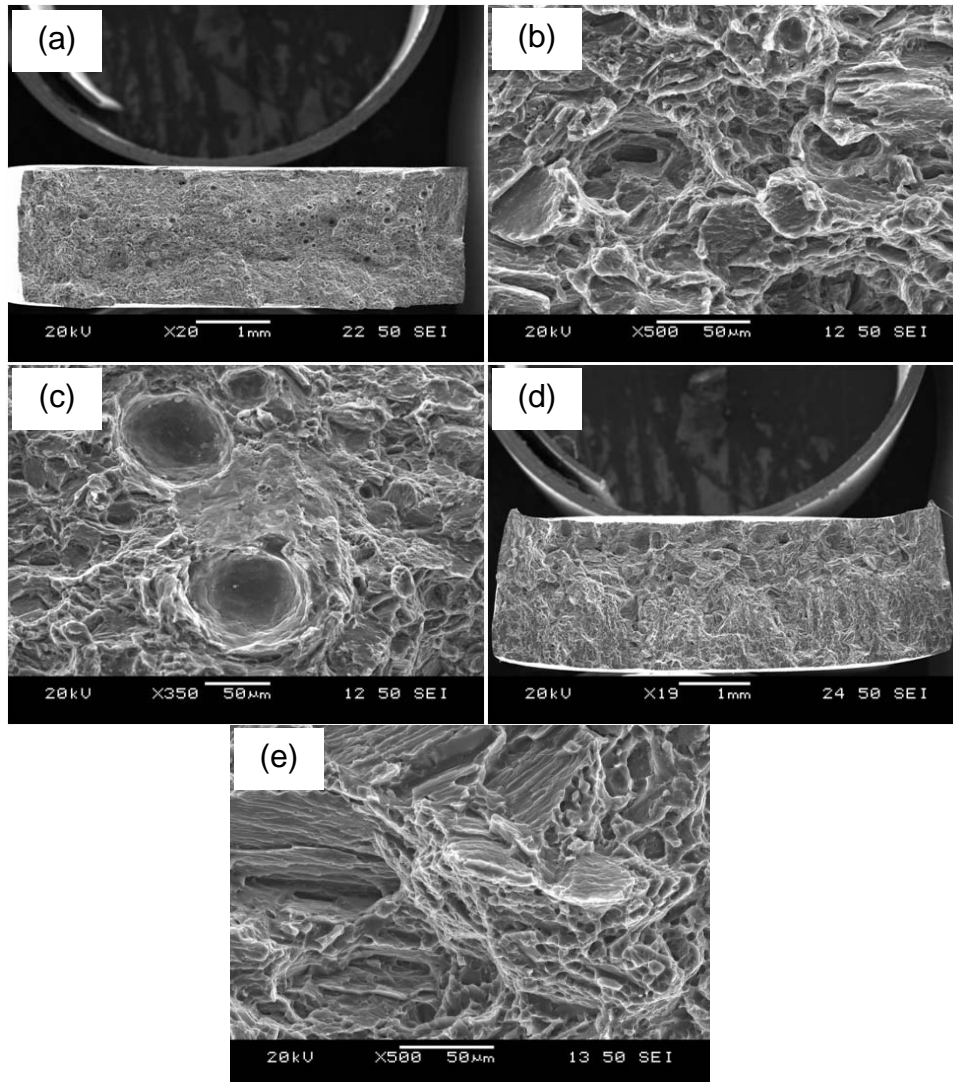


Figure 5.13: Typical SEM images showing the fracture surfaces after tensile testing at a strain rate of  $1 \times 10^{-5} \text{ s}^{-1}$ , (a) overall view of the entire fracture surface and (b) and (c) magnified view at higher magnifications of a FLWed sample, (d) overall view of the entire fracture surface, and (e) magnified view at a higher magnification of a DLWed sample.

SEM examinations revealed that dimple-like ductile fracture characteristics appeared in the BM, while some cleavage-like flat facets together with dimples and river marking were observed in the welded samples. Gas pores were more obvious in the FLWed samples than in the DLWed samples as seen from Figure 5.13(a)-(c), leading to a decrease of ductility (%El). Cleavage-like brittle fracture characteristics, i.e., some flat facets in conjunction with river marking, appeared in both the welded samples as shown in Figure 5.13(b), (c) and (e). The river marking was caused by the crack moving through the grains along a number of crystallographic planes which formed a series of plateaus and connecting ledges [82]. The fractographic observations corresponded well to the relatively low percent elongation of 5~6% in the welded samples (Figure 5.9 and 5.10(c)).

## **5.6 Fatigue Properties**

Load-controlled fatigue tests were conducted on the BM, FLWed and DLWed specimens and the obtained results are shown in Figure 5.14. The fatigue data gives an indication of the influence of the welding on the fatigue life and integrity which have to be taken into account in designing welded structural components made from Mg alloys. It is seen from Figure 5.14 that the fatigue life decreased after welding. However, similar to the tensile strength (Figure 5.10(a) and (b)), the fatigue life of the FLWed joints was close to that of the BM, which was much longer than that of DLWed joints. As the stress amplitude decreased the difference of fatigue life among the welded joints and the BM became smaller in the semi-log scale diagram. The obtained fatigue limit and calculated fatigue ratio of the BM and laser welded joints are listed in Table 5-2.

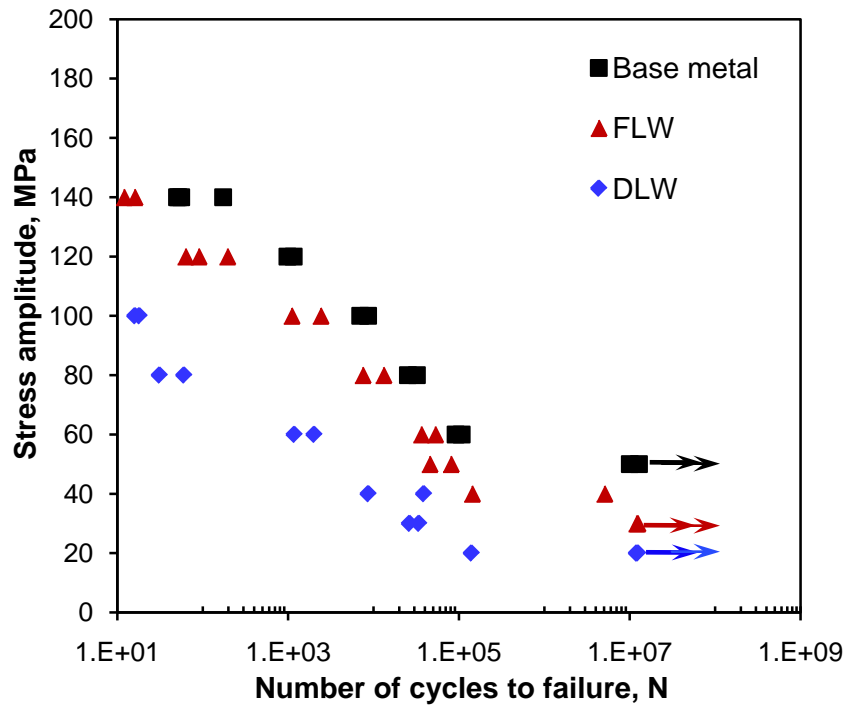


Figure 5.14: S-N curves of the AZ31B base metal, FLWed and DLWed joints tested at R=0.1, 50 Hz and room temperature.

Table 5-2 Ultimate tensile strength, fatigue limit and fatigue ratio of the BM, FLWed and DLWed joints.

Specimen	Fatigue limit (MPa)	Ultimate tensile strength (MPa)	Fatigue ratio
Base metal	50	285	0.175
FLW	30	260	0.115
DLW	20	169	0.118

The fatigue limit of the FLWed and DLWed joints dropped down by 40% and 60%, respectively, and the fatigue ratio for both types of laser welded joints decreased by about

34%, compared to that of the BM. This was mainly attributed to the microstructural change after welding, as illustrated in Figures 5.3 and 5.4. In addition, the geometry and shape of the DLWed joints were other factors responsible for the considerable decrease in the fatigue life (Figure 5.14). The presence of the weld droplet in the FZ of the DLWed joints (Figure 5.4(a)) would result in an extra bending moment. This would facilitate the early fatigue crack initiation and subsequent propagation at the center of the weld droplet in the DLWed joints, as indicated by A in Figure 5.4(a), thus giving rise to a significantly reduced fatigue strength or fatigue life of the DLWed joints (Figure 5.14). Basquin-type equation discussed in Chapter 4 was used to fit the obtained fatigue data. The obtained  $\sigma_f'$  and  $b$  values are listed in Table 5-3.

Table 5-3: Fatigue strength coefficient  $\sigma_f'$  and fatigue strength exponent  $b$  of the base metal, FLWed and DLWed joints.

Specimen	$\sigma_f'$ (MPa)	$b$
Base metal	274	-0.115
FLW	218	-0.121
DLW	153	-0.133

Normally, a smaller value of  $b$  corresponded to a longer fatigue life [82]. However, from Table 5-3 it can be seen that the relative values of the fatigue strength exponent was ranked with DLWed < FLWed < BM joints indicating BM should have lower fatigue limit which is impossible. In contrast, the value of the fatigue strength coefficient was highest for the BM, and lowest for the DLWed joints, with the  $\sigma_f'$  value of FLWed joints

laying in-between those of the BM and DLWed joints. This suggested both fatigue strength co-efficient and fatigue strength exponent need to be considered in design consideration.

## 5.7 Fatigue Fractography

Figures 5.15 and 5.16 show typical SEM images taken from the fatigue fracture surface of FLWed and DLWed joints, respectively.

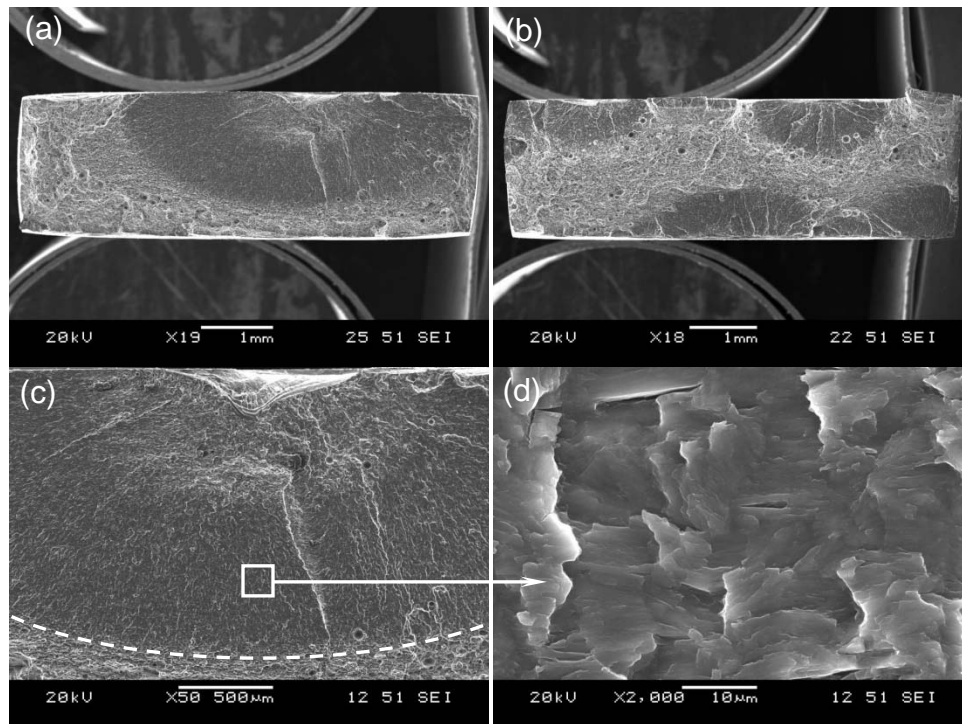


Figure 5.15: Typical SEM images of fatigue fracture surface of FLWed joints. (a) overall view of the entire fracture surface at a lower stress amplitude of 40 MPa, (b) multiple crack initiation at a higher stress amplitude of 80 MPa, (c) crack initiation from a welding defect, and (d) crack propagation zone.

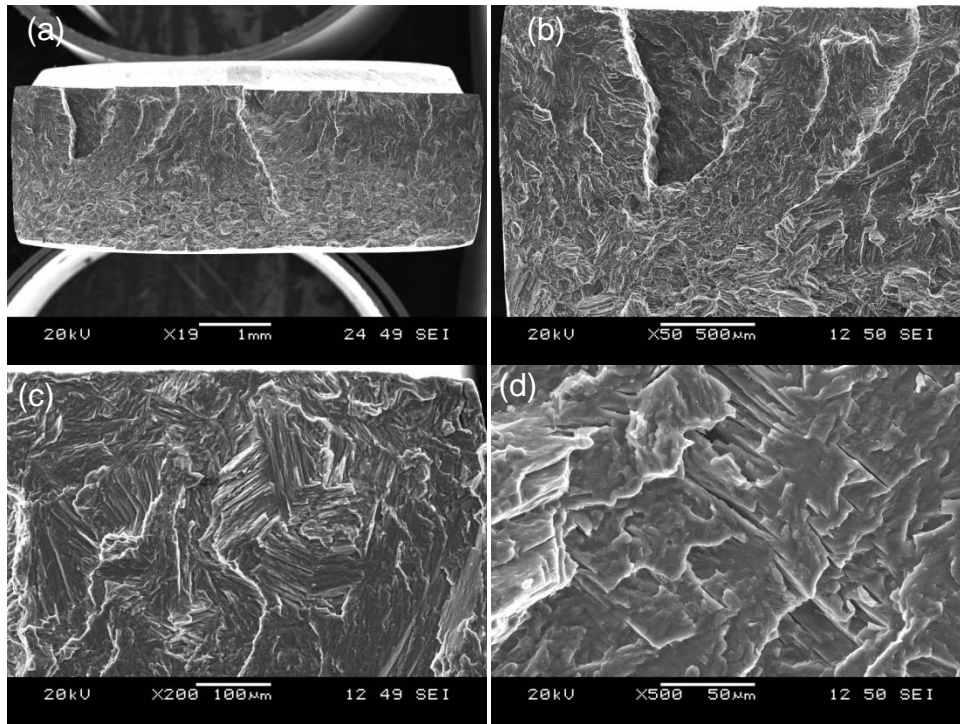


Figure 5.16: Typical SEM images of fatigue fracture surface of a DLWed joint tested at a stress amplitude of 40 MPa. (a) overall view of the entire fracture surface at a low magnification (b) welding defect at a higher magnification, (c) crack initiation site at a higher magnification, and (d) crack propagation zone at a higher magnification.

The fatigue crack initiated from the near-surface welding defect (Figure 5.15(a,c) and Figure 5.16(a,b)) or from the surface (Figure 5.15(a,b)). Welding defects or shrinkage pores were observed in both types of laser welded joints (Figure 5.15(b,c) and 5.16(b)). Multiple crack initiation sites were more apparent at higher stress amplitudes as seen from Figure 5.15(b). In the absence of surface welding defects (e.g., Figure 5.15(b)), surface grains were usually less constrained than the interior grains, so that the occurrence of slip in a few grains near the specimen surface could be relatively easier during fatigue [118]. Surface roughness and protrusions could also act as the site for

stress concentration that caused the crack initiation during fatigue. Fatigue crack propagation was mainly characterized by fatigue striations (Figure 5.15(d) and 5.16(d)) along with secondary cracks, which were usually perpendicular to the propagating direction. The fatigue striations normally occurred by a repeated plastic blunting-sharpening process in the face-centered cubic materials due to the slip of dislocations in the plastic zone ahead of the fatigue crack tip, the formation of the fatigue striations in the magnesium alloys with a hexagonal close-packed crystal structure was expected to be related to the twinning in the compressive phase and detwinning in the tensile phase [3,107-109,119]. Further studies are needed in this area.

## CHAPTER 6

### CONCLUSIONS AND FUTURE WORK

#### 6.1 Summary and Conclusions

Based on the results and discussion of the mechanical properties of the welded AZ31B-H24 Mg alloy, following conclusions can be drawn.

1. The microstructure of the as-received AZ31B-H24 consisted of small elongated grains with some Mn-Al containing inclusions which were still present in different zones after welding. The friction stir welding (FSW) resulted in recrystallized and relatively small grains in the stir zone (SZ) and thermomechanically-affected zone (TMAZ), and partially recrystallized grains in the heat-affected zone (HAZ). After double sided arc welding (DSAW), fully recrystallized grains with a relatively large grain size were observed in the HAZ, and the divorced eutectic structure containing  $\beta\text{-Mg}_{17}\text{Al}_{12}$  particles in the interdendritic and intergranular regions appeared in the fusion zone.
2. Both diode laser welding (DLW) and fiber laser welding (FLW) resulted in a typical solidification structure in the fusion zone (FZ) coupled with  $\beta\text{-Mg}_{17}\text{Al}_{12}$  particles in the interdendritic and intergranular regions while recrystallized grains appeared in the heat-affected zone (HAZ). In both types of laser welded joints, columnar dendrites were observed near the fusion boundary while equiaxed dendrites occurred at the center of the FZ. However, in the FLWed joints with a narrower FZ, the grain size

was smaller due to the higher cooling rate in comparison with the DLWed joints with a wider FZ.

3. While the YS was higher, the UTS and ductility were lower in the FSWed samples than in the DSAWed samples. This was due to the premature fracture caused by the presence of welding defects in the FSWed samples at the bottom surface. However, the strength of the FSWed samples was still similar to or higher than those reported in the literature due to the smaller grain sizes arising from the high speed low temperature FSW.
4. A significantly higher YS of about 170 MPa was achieved at a high weld pitch of 1.2 mm/rev, in comparison with the YS of approximately 110 MPa reported for AZ31-H24 Mg alloy using a weld pitch range from 0.039 to 0.24 mm/rev. After FSW, while both the YS and UTS were lower, the strain hardening exponent was observed to be much higher, and the effect of strain rate on the YS and UTS became weaker as well, although the ductility decreased slightly with increasing strain rate.
5. Despite the presence of cavity defects near the bottom surface of the FSWed joints made with a RHT pin tool rotating clockwise, which caused a bigger experimental scatter, the UTS became slightly lower, the YS slightly higher and the ductility was similar, in comparison with the FSWed joints made with a LHT pin tool turning in the same direction.
6. While the YS, UTS of the DLWed joints became much lower due to the larger dendrite cell size and the presence of weld droplet in the FZ, the decrease of the YS, UTS in the FLWed joints was moderate. The FLW resulted in a joint efficiency of

about 91% due to the narrower FZ, smaller grain size and absence of weld droplet in the FZ. However, the ductility after both types of laser welding decreased drastically.

7. The YS, UTS, strain hardening exponent and strain hardening rate increased slightly, and ductility decreased with increasing strain rate. Stronger strain-rate sensitivity was observed in the base metal due to the smaller grain size and higher flow stress in comparison with the welded joints.
8. Among all the welded joints, the strain hardening capacity of the DSAWed and DLW samples was almost the same (the DLWed joint was observed to be a little bit higher than the DSAWed joint) and observed to be twice that of the base metal, and the FLWed joints had the lowest hardening capacity. The hardening capacity of the friction stir welded joints lied in-between them.
9. After welding fatigue life was reduced. However, the DSAWed joint exhibited good fatigue properties in comparison with the FSWed joints while the FLWed joints exhibited better fatigue performance than the DLWed joints. Fatigue strength or life was observed to be higher in the FSWed joints made with the LHT pin tool in the clockwise rotation than that of the FSWed joints made with the RHT pin tool in the same rotational direction. This was due to the elimination of the welding porosity located near the bottom surface of the FSWed joints in the former case via a downward material flow close to the pin tool surface. Fatigue life increased either by increasing the tool rotation while welding speed was kept constant or increasing the welding speed while the tool rotation remained same.
10. In the tensile and fatigue tests, failure of all the FSWed joints occurred in the area between the SZ and TMAZ either at the AS or RS side, depending on the welding

parameters, while all the DSAWed joints failed at the FZ. It seemed that, at a low welding speed of 10 mm/s, the FSWed joints made with the LHT pin tool turning clockwise failed at the AS side, while a higher welding speed of 30 mm/s and RHT pin tool rotating clockwise tended to promote failure at the RS side. The FLWed joints fractured at the boundary of HAZ and columnar dendrites, while the DLWed joints fractured exclusively at the centre of the FZ due to the large dendrite cell size and the presence of a weld droplet. Dimple-like ductile fracture characteristics appeared in the BM, while some cleavage-like flat facets together with dimples and river markings were observed in the welded samples. The gas pores on the fracture surface of the FLWed joints were observed due to keyhole welding process.

11. Fatigue crack initiation occurred from the specimen surface or near-surface welding defects in all of the welded joints. Multiple crack initiation was observed at higher stress amplitudes. Fatigue crack propagation was characterized by the formation of fatigue striations with the spacing increased with increasing distance from the initiation site, along with the presence of secondary cracks.

## **6.2 Scope of Future Work**

The research in the field of magnesium has greatly improved. In the present study, a number of joining methods in terms of mechanical properties were studied. A solid state joining method, such as, FSW was compared to a fusion welding method such as DSAW. Different groups of FSWed joints were compared and tested to find out the maximum weld pitch at which optimum YS and UTS could be found. Different weld tools were considered to observe the effect of thread on mechanical properties. FLW was observed

to be more effective in terms of mechanical properties than the DLW process. However, more studies are needed in the aspect of joining technology on Mg AZ31 alloy.

1. In the DSAW method only one welding condition was utilized to evaluate the microstructure and mechanical properties. More study needs to be done by increasing or decreasing the welding speed.
2. In FSW, both RHT and LHT weld tools were considered and unsatisfactory joining was observed at the bottom surface of the joint when the RHT weld tool was used. However, mechanical properties between those two joints (welded by RHT and LHT) were not significantly distinguishable. This is due to the base material having only 2 mm thickness. Thicker material should be considered to observe significant differences of mechanical properties between FSWed joints welded by RHT and LHT weld tools.
3. Both tensile and fatigue failure depend upon the FSW tool and welding parameters. It is assumed that after FSW, texture of the welding zone was changed completely or partly from the BM. Texture identification on the fracture surface by XRD would be interesting research work.
4. In the present study, YS and UTS were observed to increase with increasing weld pitch during FSW. However, the optimum weld pitch to reach maximum YS and UTS is yet to be found.
5. Both FLWed and DLWed joints were conducted by using only one welding speed. More study is needed by using different welding speeds.

## REFERENCES

- [1] E. Essadiqi, Magnesium sheet technology perspectives, JOM, 2009, 61, 13–23.
- [2] E.A. Nyberg, A.A. Luo K. Sadayappan and W.F. Shi, Magnesium for future autos, Adv. Mater. Processes, 2008, 166, 35–37.
- [3] S. Begum, D.L. Chen, S. Xu and A.A. Luo, Effect of strain ratio and strain rate on low cycle fatigue behavior of AZ31 wrought magnesium alloy, Mater. Sci. Eng. A, 2009, 517, 334–343.
- [4] M. Tsujikawa, H. Somekawa, k. Higashi, H. Iasaki, T. Hasegawa and A. Mizuta, Fatigue of welded magnesium alloy joints, Mater. Trans., 2004, 45, 419–422.
- [5] N. Afrin, D.L. Chen, X. Cao and M. Jahazi, Microstructure and tensile properties of friction stir welded AZ31B magnesium alloy, Mater. Sci. Eng. A, 2008, 472, 179-186.
- [6] M. Pareek, A. Polar, F. Rumiche and J.E. Indacochea, Metallurgical evaluation of AZ31B-H24 magnesium alloy friction stir welds, Journals of Materials Engineering and Performance, 2007, 16, 655-662.
- [7] S. Lim, S. Kim, C.G. Lee, C.D. Yim and S.J. Kim, Tensile behavior of friction-stir-welded AZ31-H24 Mg alloy, Metall. Mater. Trans. A, 2005, 36, 1609–1612.
- [8] M. Abbasi Gharacheh, A.H. Kokabi, G.H. Daneshi, B. Shalchi and R. Sarrafi, The influence of the ratio of "rotational speed/traverse speed" ( $\omega/v$ ) on mechanical properties of AZ31 friction stir weld, Inter. J. Machine Tools & Manufac., 2006, 46(15), 1983–1987.

- [9] J. Liu, J.H. Dong and K. Shinozaki, Microstructures and properties of fiber laser welded ACM522 magnesium alloy joint, *Materials Science Forum*, 2009, 610-613, 911-914.
- [10] L. Yu, K. Nakata and J. Liao, Weld porosity in fibre laser weld of thixomolded heat resistant Mg alloys, *Science and Technology of Welding and Joining*, 2009, 14(6), 554-558.
- [11] H.E. Friedrich and B.L. Mordike, *Magnesium Technology- Metallurgy, Design Data, Applications*, Springer-Verlag Berlin Heidelberg, Germany, 2006.
- [12] K.U. Kainer, *Magnesium Alloys and Technology*, Wiley-VCH, Cambridge, 2003.
- [13] A. Staroselsky and L. Anand, A constitutive model for HCP materials deforming by slip and twinning: application to magnesium alloy AZ31B, *International Journal of Plasticity*, 2003, 19, 1843–1864.
- [14] W.F. Smith, *Structure and properties of Engineering alloys*, McGraw-Hill, Inc, New York, 1993.
- [15] X. Cao and M. Jahazi, Effect of welding speed on the quality of friction stir welded butt joints of a magnesium alloy, *Materials and Design*, 2009, 30, 2033-2042.
- [16] C.S. Wu and J.S. Sun, Numerical analysis of temperature field during double-sided arc welding of thick materials, *Computational Materials Science*, 2002, 25, 457–468.
- [17] W.M. Thomas, E.D. Nicholas, J.C. Needham, M.G. Church, P. Templesmith and C.J. Dawes, GB Patent Application No. 9125978.9, 1991.
- [18] S.A. Emam and A.E. Domiaty, A refined energy-based model for friction-stir

- welding, *Eng. Technol.*, 2009, 53, 1016-1022.
- [19] S. Katayama, H. Nagayama, M. Mizutani and Y. Kawahito, Fibre laser welding of aluminium alloy, *Welding International*, 2009, 23(10), 744–752.
- [20] S.K. Panda, V.H.B. Hernandez, M.L. Kuntz and Y. Zhou, Formability analysis of diode laser welded tailored blanks of advanced high strength steel sheets, *Metallurgical and Materials Transaction A*, 2009, 40, 1955-197.
- [21] P.S. Mohanty and J. Mazumder, Solidification behavior and microstructural evolution during laser beam-material interaction, *Metall. Trans.*, 1998, 45, 1269-1279.
- [22] S. Kou and Y. Le, Alternating grain orientation and weld solidification cracking, *Metall. Trans. A*, 1985, 16(10), 1887-96.
- [23] M. Rappaz, J.M. Vitek, S.A. David and L.A. Boatner, Microstructural Formation in Longitudinal Bicrystal Welds, *Metall. Trans., A*, 1993, 24, 1433-46.
- [24] K. Somboonsuk, J.T. Mason, and R. Trivedi, interdendritic spacing: part I. experimental studies, *Metall. Trans. A*, 1984, 15(6), 967-975.
- [25] S.H. Wu, J.C. Huang and Y.N. Wang, Evolution of microstructure and texture in Mg-Al-Zn alloys during electron-beam and gas tungsten arc welding, *Metall. Trans. A*, 2004, 35(8), 2455-2469.
- [26] Y. Liu, J. Koch, J. Mazumder and K. Shibata, Processing, microstructure, and properties of laser-clad Ni alloy FP-5 on Al alloy AA333, *Metals Trans. B*, 1994, 25(3), 425-34.

- [27] Q. Yajie, Z. Chen, Z. Yu, X. Gong and M. Li, Effects of heat input on microstructure and tensile properties of laser welded magnesium alloy AZ31, *Mater. Character.*, 2008, 59(10), 1799-1804.
- [28] L. Yu, K. Nakata, N Yamamoto and J. Liao, Texture and its effect on mechanical properties in fiber laser weld of a fine-grained Mg alloy, *Materials Letters*, 2009, 63(11), 870-72.
- [29] Z.H. Yu, H.G. Yan, X.S. Gong: Y.J. Quan, J.H. Chen and Q. Chen, Microstructure and mechanical properties of laser welded wrought ZK21 magnesium alloy *Materials Science and Engineering A*, 2009, 523(1-2), 220-25.
- [30] A. Weisheit, R. Galun and B.L. Mordike, CO<sub>2</sub> laser beam welding of magnesium-based alloys, *Weld. J.*, 1998, 77(4), 148-154.
- [31] H. Zhao and T. Debroy, Pore formation during laser beam welding of die-cast magnesium alloy AM60B - Mechanism and remedy, *Weld. J.*, 2001, 80(8), 204-210.
- [32] Z. Sun, D. Pan and J. Wei, Comparative evaluation of tungsten inert gas and laser welding of AZ31 magnesium alloy, *Sci. Technol. Weld. Joining*, 2002, 7(6), 343-351.
- [33] G. Padmanaban and V. Balasubramanian, Fatigue performance of pulsed current gas tungsten arc, friction stir and laser beam welded AZ31B magnesium alloy joints *Materials and Design*, 2010, 31(8), 3724-3732.
- [34] H. Sun, G. Song and L.F. Zhang, Effects of oxide activating flux on laser welding of magnesium alloy, *Science and Technology of Welding and Joining*, 2008, 13(4), 305-11.

- [35] Y.J. Quan, Z.H. Chen, X.S. Gong, Z.H. Yu, Effect of heat input on microstructure and tensile properties of laser welded magnesium alloy AZ31, *Materials Characterization* 2008, 59, 1491-1497.
- [36] L. Liu and C. Dong, Gas tungsten-arc filler welding of AZ31 magnesium alloy, *Materials Letters*, 2006, 60, 2194-2197.
- [37] J. Zhu, L. Li and Z. Liu, CO<sub>2</sub> and diode laser welding of AZ31 magnesium alloy, *Applied Surface Science*, 2005, 247, 300-306.
- [38] S.H. Kim, B.S. You, B.S You and C.D. Yim, The effect of rolling conditions on the microstructure and texture evolution of AZ31 Mg alloy sheets, *Mater.Forum*, 2005, 29, 530-535.
- [39] R. Johnson, Friction stir welding of magnesium alloys, *Mater. Sci. Forum* 2003, 419-422, 365-370.
- [40] X.H. Wang and K. Wang, Microstructure and properties of friction stir butt-welded AZ31 magnesium alloy, *Mater. Sci. Eng. A*, 2006, 431, 114-117.
- [41] S.H.C. Park, Y.S Sato and H. Kokawa, Effect of micro-texture on fracture location in friction stir weld of Mg alloy AZ61 during tensile test, *Scripta Mater.*, 2003, 49, 161-166.
- [42] M. Fairman, N. Afrin, D.L. Chen, X.J. Cao and M. Jahazi, Microstructural evaluation of friction stir processed AZ31B-H24 magnesium alloy, *Can. Metall. Quart.*, 2007, 46, 425-432.
- [43] W. Woo, H. Choo, M.B. Prime, Z. Feng and B. Clausen, Microstructure, texture and residual stress in a friction-stir-processed AZ31B magnesium alloy, *Acta Mater.*, 2008, 56, 1701-1711.

- [44] L. Commin, M. Dumont, J.E. Masse, L. Barrallier, *Acta Mater.* 57 (2009) 326-334.
- [45] N. Afrin, D.L. Chen, X. Cao and M. Jahazi, Strain hardening behaviour of a friction stir welded magnesium alloy, *Scripta Mater.*, 2007, 57, 1004-1007.
- [46] T.U. Seidel and A.P. Reynolds, Visualization of the material flow in AA2195 friction-stir welds using a marker strain technique, *Metall. Mater. Trans. A*, 2001, 32, 2879-2884.
- [47] Y. Li, L.E. Murr and J.C. McClure, Flow patterns during friction stir welding, *Materials Characterization, Scripta Mater.*, 1999, 40, 1041-1046.
- [48] K. Colligan, Material Flow Behavior during Friction Stir Welding of Aluminum *Welding J.*, 1999, 78, 229-237.
- [49] A.P. Reynolds, Visualization of Material Flow in an Autogenous Friction Stir Weld, *Sci. Technol. Weld. Join.*, 2000, 5, 120-124.
- [50] H. Zhang, S.B. Lin, L. Wu, J.C. Feng and S.L. Ma, Defects formation procedure and mathematic model for defect free friction stir welding of magnesium alloy, *Maters. Des.*, 2006, 27, 805-809.
- [51] L. Fratini, G. Buffa, D. Palmeri, J. Hua and R. Shivpuri, Material flow in FSW of AA7075-T6 butt joints: continuous dynamic recrystallization phenomena, *J. Eng. Mater. Technol.*, 2006, 128, 228-235.
- [52] M. Guerra, C. Schmidt, J.C. McClure, L.E. Murr and A.C. Nunes, Flow patterns during friction stir welding, *Mater. Characterization*, 2003, 49, 95-101.
- [53] J.A. Schneider and A.C. Nunes. Jr., Characterization of plastic flow and resulting microtextures in a friction stir weld, *Metall. Mater. Trans. B*, 2004, 35, 777-783.

- [54] P.A. Colegrove and H.R. Shercliff, 3-Dimensional CFD modeling of flow round a threaded friction stir welding tool profile, *J. Mater. Processing Tech.*, 2005, 169, 320-327.
- [55] P. Ulysse, Three-dimensional modeling of the friction stir-welding process, *Int. J. Mach. Tools. Manuf.*, 2002, 42, 1549-1557.
- [56] R. Nandan, G.G. Roy and T. Debroy, Numerical simulation of three-dimensional heat transfer and plastic flow during friction stir welding, *Metall. Mater. Trans. A*, 2006, 37, 1247-1259.
- [57] R. Nandan, G.G. Roy, T. Lienert and T. Debroy, *Sci. Technol*, Numerical Modeling of 3D Plastic Flow and heat Transfer during Friction Stir Welding of Stainless Steel, *Weld. Join.*, 2006, 11, 526-537.
- [58] H.N.B. Schmidt, T.L. Dickerson and J.H. Hattel, Material flow in butt friction stir welds in AA2024-T3, *Acta Mater.* 2006, 54, 1199-1209.
- [59] H.W. Zhang, Z. Zhang and J.T. Chen, 3D modeling of material flow in friction stir welding under different process parameters, *J. Mater. Proc. Tech.*, 2007, 183, 62-70.
- [60] C. Hamilton, S. Dymek and M. Blicharski, A model of material flow during friction stir welding *Mater. Character.* 2008, 59, 1206-1214.
- [61] A. Gerlich, P. Su, M. Yamamoto and T.H. North, Material flow and intermixing during dissimilar friction stir welding, *Sci. Tech. Weld. Join.*, 2008, 13, 254-264.
- [62] K. Kumar and S.V. Kailas, The role of friction stir welding tool on material flow and weld formation *Mater. Sci. Eng. A*, 2008, 485(1-2), 367-374.

- [63] Y.H. Zhao, S.B. Lin, L. Wu and F.X. Qu, The influence of pin geometry on bonding and mechanical properties in friction stir weld 2014 Al alloy, *Mater. Lett.*, 2005, 59, 2948-2952.
- [64] ASTM Standard E8/E8M, 2008, Standard Test Methods for Tension Testing of Metallic Materials, ASTM International, West Conshohocken, PA, 2008, doi: 10.1520/E0008/E0008M-08, [www.astm.org](http://www.astm.org).
- [65] W.B. Lee, Y.M. Yeon, S.K. Kim, Y.J. Kim and S.B. Jung In: H.I. Kaplan, Editor, *Magnesium Technology*, TMS, 309-312, 2002.
- [66] J.A. Esparza, W.C. Davis, E.A. Trillo and L.E. Murr, Friction-stir welding of magnesium alloy AZ31B, *J. Mater. Sci. Lett.*, 2002, 21, 917-920.
- [67] A.C. Nunes Jr., E.L. Bernstein and J.C. McClure, A rotating plug model for friction stir welding, the 81st American Welding Society Annual Convention, Chicago, IL, USA, 2000.
- [68] L. Xing, L.M. Ke, S.L. Wang and F. Wang, Joining of Advanced and Specialty Materials X, *Material Science and Technology (MS&T)*, Pittsburgh, 2008, 2349-2361.
- [69] X.Z. Lin and D.L. Chen, Strain controlled cyclic deformation behavior of an extruded magnesium alloy, *Mater. Sci. Eng. A*, 2008, 496, 106-113.
- [70] L.M. Liu, G. Song and M.L. Zhu, Low-power laser/arc hybrid welding behavior in AZ-based Mg alloys, *Metallurgical and Materials Transactions A*, 2008, 39, 1702-1711.

- [71] Peng Liu, Yajiang Li, Haoran Geng and Juan Wang, Microstructure characteristics in TIG welded joint of Mg/Al dissimilar materials, *Materials letters*, 2007, 61, 1288-1291.
- [72] G. Ben-Hamu, D. Eliezer, C.E. Cross and Th. Böllinghaus, The relation between microstructure and corrosion behavior of GTA welded AZ31B magnesium sheet, *Mater. Sci. Eng. A*, 2007, 452-453, 210-218.
- [73] S.F. Su, J.C. Huang, H.K. Lin and N.J. Ho, Electron-beam welding behavior in Mg-Al-based alloys, *Metall. and Mater. Trans. A*, 2002, 33, 1461-1473.
- [74] G. Padmanaban and V. Balasubramanian, J.K. Sarin Sundar, Influences of welding processes on microstructure, hardness, and tensile properties of AZ31B, *JMPEG*, 2009, doi: 10.1007/s11665-009-9389-7.
- [75] H. Takuda, S. Kikuchi, N. Yoshida and H. Okahara, Tensile properties and press formability of Mg-9Li-1Y alloy sheet, *Mater. Trans.*, 2003, 44, 2266-2270.
- [76] L. Jiang, J.J. Jonas, A.A. Luo, A.K. Sachdev, S. Godet In: A.A.Luo, N.R.Neelameggham, R.S.Beals, Editors, *Magnesium Technology*, TMS, 2006, 233-238.
- [77] Y.M. Wang and E. Ma, Strain hardening, strain rate sensitivity and ductility of nanostructured metals, *Mater. Sci. Eng. A*, 2004, 375-377, 46-52.
- [78] X.Z. Lin and D.L. Chen, Strain hardening and strain-rate sensitivity of an extruded magnesium alloy, *Journal of Materials Engineering and Performance*, 2008, 17, 894-901.

- [79] V. Livescu, C.M. Cady, E.K. Cerreta, B.L. Henrie and G.T. Gray III In: A.A. Luo, N.R. Neelameggham, R.S. Beals, Editors, Magnesium Technology, TMS, 2006, 153-158.
- [80] C. Hamilton, A. Sommers and S. Dymek, A thermal model of friction stir welding applied to Sc-modified Al–Zn–Mg–Cu alloy extrusions, *Inter. J. Machine Tools & Manufacture*, 2009, 49, 230-238.
- [81] Y.N. Wang, C.I. Chang, C.J. Lee, H.K. Lin and J.C. Huang, Texture and weak grain size dependence in friction stir processed Mg–Al–Zn alloy, *Script Mater.*, 2006, 55, 637-40.
- [82] G.E. Dieter, *Mechanical Metallurgy*, 3rd ed., McGraw-Hill, MA, USA, 1986.
- [83] H.B. Chen, K. Yan, T. Lin, S.B. Chen, C.Y. Jiang and Y. Zhao, The investigation of typical welding defects for 5456 aluminum alloy friction stir welds, *Mater. Sci. Eng. A*, 2006, 433, 64-69.
- [84] K. Elangovan and V. Balasubramanian, Influences of tool pin profile and axial force on the formation of friction stir processing zone in AA6061 aluminium alloy, *Mater. Sci. Eng. A*, 2007, 459, 7-18.
- [85] D.R. Ni, P. Xue, D. Wang, B.L. Xiao and Z.Y. Ma, Inhomogeneous microstructure and mechanical properties of friction stir processed NiAl bronze, *Mater. Sci. Eng. A*, 2009, 524, 119-128.
- [86] J. Yang, B.L. Xiao, D. Wang and Z.Y. Ma, Effects of heat input on tensile properties and fracture behavior of friction stir welded Mg-3Al-1Zn alloy, *Mater. Sci. Eng. A*, 2010, 527(3), 708-714.
- [87] T. Shinoda, Proc. 3<sup>rd</sup> Int. Symp. on Friction Stir Welding, Kobe, Japan, 2001.

- [88] J. Luo, Z. Mei, W. Tian, Z. Wang, Diminishing of work hardening electroformed polycrystalline copper with nano-sized and uf-sized twins, *Mater. Sci. Eng. A*, 2006, 441(1-2), 282-290.
- [89] W.D. Callister Jr., *Materials Science and Engineering - An Introduction*, 7<sup>th</sup> Edition, John Wiley & Sons, Inc., New York, USA, 2007.
- [90] W.F. Hosford, *Mechanical Behavior of Materials*, Cambridge University Press, New York, USA, 2005.
- [91] J.H. Hollomon, Tensile deformation, *Trans. AIME*, 1945, 162, 268-289.
- [92] R.W. Hertzberg, *Deformation and Fracture Mechanics of Engineering Materials*, 4<sup>th</sup> Edition, John Wiley & Sons, New York, USA, 1996.
- [93] L. Ratke and P.I. Welch, The differential work hardening coefficient and classical work hardening laws, in: *13th Biennial Congress - International Deep Drawing Research Group: Efficiency in Sheet Metal Forming*, Melbourne, Australia, 1984, 427-435.
- [94] X.H. Chen and L. Lu, Work hardening of ultrafine-grained copper with nanoscale twins, *Scripta Mater.*, 2007, 57, 133-136.
- [95] P. Ludwik, *Elemente der Technologischen Mechanik*, Springer-Verlag OHG, Berlin 1909, 32.
- [96] U.F. Kocks and H. Mecking, Physics and phenomenology of strain hardening: the FCC case, *Prog. Mater. Sci.*, 2003, 48, 171-273.
- [97] J.A. del Valle, F. Carreno and O.A. Ruano, Influence of texture and grain size on work hardening and ductility in magnesium-based alloys processed by ECAP and rolling, *Acta Materialia*, 2006, 54, 4247-4259.

- [98] M. Srinivasan and T.G. Stoebe, Temperature dependence of yielding and work-hardening rates in magnesium oxide single crystals, *Journal of Material Science*, 1974, 9, 121-128.
- [99] A.D. Rollett and U.F. Kocks, A review of the stages of work hardening, *Solid State Phenom.*, 1994, 35-36, 1-18.
- [100] W. Pantleon, Stage IV work-hardening related to disorientations in dislocation structures, *Mater. Sci. Eng. A*, 2004, 387-389, 257-261.
- [101] J.A. del Valle and O.A. Ruano, Influence of the grain size on the strain rate sensitivity in an Mg-Al-Zn alloy at moderate temperatures, *Scripta Materialia*, 2006, 55, 775-778.
- [102] C.W. Sinclair, W.J. Poole and Y. Brechet, A model for the grain size dependent work hardening of Copper, *Scripta Mater.*, 55, 2006, 739-742.
- [103] I. Kovacs, N.Q. Chinh and E. Kovacs-Csetenyi, Grain size dependence of the work hardening process in Al 99.99, *Phys. Status Solidi A*, 2002, 194, 3-18.
- [104] J.A. del Valle, A.C. Picasso and R. Romero, The superposition of flow stress contributions in a precipitate hardened Ni-based alloy studied by strain rate sensitivity measurements, *Acta Materialia*, 2003, 51, 6443-6452.
- [105] U.S. Lindholm, Some experiments with split Hopkinson pressure bar, *J. Mech. Phys. Solids*, 1964, 12, 317-335.
- [106] Y.V.R.K. Prasad and R.W. Armstrong, Polycrystal versus single-crystal strain rate sensitivity of cadmium, *Philos. Mag.*, 1974, 29, 1421-1425.

- [107] S. Begum, D.L. Chen, S. Xu and A.A. Luo, Strain-controlled low-cycle fatigue properties of a newly developed extruded magnesium alloy, *Metall Mater Trans A*, 2008, 39, 3014–26.
- [108] L. Wu, A. Jain, D.W. Brown, G.M. Stoica, S.R. Agnew, B. Clausen, D.E. Fielden and P.K. Liaw, Twinning-detwinning behavior during the strain-controlled low-cycle fatigue testing of a wrought magnesium alloy ZK60A, *Acta Mater*, 2008, 56, 688–95.
- [109] X.Y. Lou, M. Li, R.K. Boger, S.R. Agnew and R.H. Wagoner, Hardening evolution of AZ31B Mg sheet, *Inter J Plast*, 2007, 23, 44–86.
- [110] *Welding Handbook*, 7th ed., Vol. 1, American Welding Society, Miami, FL, 1976.
- [111] W.F. Savage, C.D. Lundin and A.H. Aronson, Weld metal solidification mechanics, *Weld. J.*, 1965, 44(4), 175-181.
- [112] A. Munitz, Microstructure of rapidly solidified laser molten Al-4.5 wt pct Cu surfaces, *Metall. Trans. B*, 1985, 16, 149-161.
- [113] A.J. Paul and T. Debroy, Physical process in fusion welding, *Rev. Modern Phys.*, 1995, 67, 85-112.
- [114] S. Kou and Y. Le, Effect of quenching on the solidification structure and transformation behavior of stainless steel welds, *Metall. Trans. A*, 1982, 13, 1141-1152.
- [115] T.S. Plaskett, and W.C. Winegard, Cell to dendrite transition in tin base alloys, *Can. J. Physiol*, 1960, 38, 1077-1088.
- [116] S. Kou, *Welding Metallurgy*, 2<sup>nd</sup> Ed., John Wiley & Sons, USA, 2003.
- [117] Y. Kawahito, M. Mizutani and S. Katayama, *Trans. JWRI.*, 2007, 36, 11-16.

- [118] K.S. Chan, P. Yi-Ming, D. Davidson and R.C. McClung, Fatigue crack growth mechanisms in HSLA-80 steels, *Mater. Sci. Eng. A*, 1997, 222, 1-8.
- [119] S. Begum, D.L. Chen, S. Xu and A.A. Luo, Low cycle fatigue properties of an extruded AZ31 magnesium alloy, *International Journal of Fatigue*, 2009, 31(4), 726-735.

## MD. SAKI MURSALIN CHOWDHURY

**EDUCATION** Master of Applied Science (August 2010)  
Ryerson University, Toronto, ON  
Major: Mechanical Engineering  
Bachelor of Applied Science (August 2006)  
Bangladesh University of Engineering & Technology, Bangladesh  
Major: Mechanical Engineering

**EXPERIENCE** Teaching Assistant, Sep. 2008- Dec 2009  
Ryerson University, Toronto, ON, Canada

R & D Engineer, Dec 2006- Jul 2008  
New-G-Boiler Co., Dhaka, Bangladesh

**AWARDS** Ryerson Graduate Scholarship for academic excellence, 2008-2010  
Ryerson Graduate Stipend, 2008-2010  
BUET Scholarship, 2001-2006

### LIST OF PUBLICATIONS (over the past two years during my MSc. study)

#### A. Refereed journal papers (accepted or under review):

1. S.M. Chowdhury, D.L. Chen, S.D. Bhole, X. Cao, E. Powidajko, D.C. Weckman and Y. Zhou, Tensile properties and strain hardening behavior of double sided arc welded and friction stir welded AZ31B magnesium alloy, *Materials Science and Engineering A* 527 (2010) 2951-2961.
2. S.M. Chowdhury, D.L. Chen, S.D. Bhole and X. Cao, Effect of pin tool thread orientation on fatigue strength of friction stir welded AZ31B-H24 Mg butt joints, *Procedia Engineering* 2 (2010) 825-833.
3. S.M. Chowdhury, D.L. Chen, S.D. Bhole and X. Cao, Tensile properties of a friction stir welded magnesium alloy: effect of pin tool thread orientation and weld pitch, *Materials Science and Engineering A* 527 (2010) 6064-6075.
4. S.M. Chowdhury, D.L. Chen, S.D. Bhole, X. Cao, D.C. Weckman and Y. Zhou, Fiber and diode laser welded AZ31 Mg alloy: microstructure and mechanical properties, *Materials and Metallurgical transactions A* E-TP-10-694-A.

#### B. Conference presentations:

1. S.M. Chowdhury, D.L. Chen, S.D. Bhole, X. Cao, E. Powidajko, D.C. Weckman and Y. Zhou, Mechanical properties of fiber and diode laser welded AZ31B-H24 Mg alloy, the 22nd Canadian Materials Science Conference, Waterloo University, Waterloo, June 9-11, 2010.
2. H.A. Patel, S.M. Choudhary, D.L. Chen and C.Y. Zhang, Cyclic deformation behavior of magnesium alloys, APMA-AUTO21 Annual Conference, Windsor, Ontario, June 7-10, 2010.
3. C.L. Fan, H.A. Patel, S.M. Choudhary, D.L. Chen, Cyclic deformation of magnesium alloys, APMA-AUTO21 Annual Conference, Hamilton, Ontario, May 26-28, 2009.